ABSTRACT

COHERENT CONTROL OF DISPERSIVE WAVES

by
Jimmie Adriazola

This dissertation addresses some of the various issues which can arise when posing and solving optimization problems constrained by dispersive physics. Considered here are four technologically relevant experiments, each having their own unique challenges and physical settings including ultra-cold quantum fluids trapped by an external field, paraxial light propagation through a gradient index of refraction, light propagation in periodic photonic crystals, and surface gravity water waves over shallow and variable seabeds. In each of these settings, the physics can be modeled by dispersive wave equations, and the technological objective is to design the external trapping fields or propagation media such that a high fidelity or degree of coherence of the wave phenomena is achieved.

Optimal control theory is used as the analytical and computational framework in addressing these design problems. Optimal control problems are, generally speaking, challenging searches over infinite-dimensional spaces. Methods from Hamiltonian dynamical systems, asymptotic analysis, the integrability structure of the uncontrolled constraints, and simple physical intuition are employed to better guide these searches. By introducing the dimensional reductions afforded by these methods, our computational searches are significantly more efficient, over naively attempting to search the entire space of admissible controls, both in terms of the desired outcomes and in terms of expended computational resources.

The optimal control problems posed throughout this dissertation also have the additional challenge of being nonconvex optimization problems. In order to efficiently address the nonconvex nature of these problems, the program used is a global, nonconvex search which is then accelerated by fast local methods. This methodology is specifically tailored toward maintaining feasibility

of implementing the computationally constructed control policies in technologically relevant settings.

COHERENT CONTROL OF DISPERSIVE WAVES

by
Jimmie Adriazola

A Dissertation
Submitted to the Faculty of
New Jersey Institute of Technology and
Rutgers, The State University of New Jersey – Newark
in Partial Fulfillment of the Requirements for the Degree of
Doctor of Philosophy in Mathematical Sciences

Department of Mathematical Sciences
Department of Mathematics and Computer Science, Rutgers-Newark

December 2021

APPROVAL PAGE

COHERENT CONTROL OF DISPERSIVE WAVES

Jimmie Adriazola

Dr. Roy H. Goodman, Dissertation Advisor — Date
Associate Professor of Mathematics, NJIT

Dr. David G. Shirokoff, Committee Member — Date
Associate Professor of Mathematics, NJIT

Dr. Christina A. Frederick, Committee Member — Date
Assistant Professor of Mathematics, NJIT

Dr. Richard O. Moore, Committee Member — Date
Director of Programs and Services, Society for Industrial and Applied Math, Philadelphia, Pennsylvania

---

Dr. Alejandro Aceves, Committee Member — Date
Professor of Mathematics, Southern Methodist Univeristy, Dallas, Texas

BIOGRAPHICAL SKETCH

Author: Jimmie Adriazola

Degree: Doctor of Philosophy

Date: December 2021

Undergraduate and Graduate Education:

- Doctor of Philosophy in Mathematical Sciences,
  New Jersey Institute of Technology, Newark, NJ, 2021
- Bachelor of Science in Applied Mathematics and Applied Physics,
  New Jersey Institute of Technology, Newark, NJ, 2016
- Associate of Science in Mathematics,
  County College of Morris, Randolph, NJ, 2014

Major: Mathematical Sciences

Presentations and Publications:

J. Adriazola, R. Goodman, "A Reduction-Based Strategy for Optimally Controlling Bose-Einstein Condensates", (submitted to Phys. Rev. E)

J. Adriazola, R. Goodman, "Optimal Reshaping of Stationary States in Linearly Dispersive Media", (submitted to JOSA-A)

J. Adriazola, R. Goodman, "Apodizer Design to Efficiently Couple Light into a Fiber Bragg Grating", (in preparation)

J. Adriazola, Optimal Control of Nearly Integrable Nonlinear Waves, *Applied Math Days*, Rensselaer Polytechnic Institute, 2019.

J. Adriazola, Apodizer Design to Efficiently Couple Light into a Fiber Bragg Grating *Nonlinear Waves and Coherent Structures Conference*, University of Bremen, (2020: Won SIAM travel award but conference cancelled due to the corona virus outbreak).

J. Adriazola, A Reduction-Based Strategy for Optimally Controlling Bose-Einstein Condensates, *Blackwell-Tapia Conference*, Institute for Advanced Study, 2021.

"If you look for perfection, you'll never be content."

— Leo Tolstoy

ACKNOWLEDGMENT

First, and foremost, I would like to thank my dissertation advisor, Roy Goodman. It's difficult to acknowledge, in written words, the level of patience he showed me throughout my time at NJIT. I'm deeply indebted to him for helping me through the difficult task of writing a dissertation, and for never giving up on me when, I think, most people would have. He never once expressed doubt in my technical abilities, even if he might have felt it. He must have; the amount of weekly meetings I had to tell him my code wasn't working is probably $\mathcal{O}(\varepsilon^{-1}),\ \varepsilon \ll 1$.

His commitment to the role of advisor is admirable. When I approached him with some of my research interests about optimization, he took the great effort of creating a project that would meet somewhere in between our interests. I've learned over time that this level of open-mindedness isn't something to expect from every advisor, and really demonstrates Goodman's selflessness. Throughout the last five years of this difficult journey, Goodman has always been there when I needed him most.

I deeply appreciate the encouragement and support of the dissertation committee. While Richard Moore was still a professor at NJIT, he helped Goodman and I form the skeleton of my thesis project. He was helpful in sharing the right resources, in helping me figure out what standard control theory is all about, and in helping me learn the basics of soliton physics. I appreciate how David Shirokoff shared some of his big picture ideas on what makes research useful, or even sometimes, great. He's also helped shape the format of our problem structures, influenced our methodology, and helped with a few important calculations. Alejandro Aceves is someone we could always rely on for help with his valuable physical insight. Christina Frederick has been helpful by suggesting relevant fellowships and conferences, and helpful through her very thorough review of my proposal and this dissertation.

I would also like to take this space to thank Samuel Gatley and Louis Rizzo who both worked in the Flexible Electronic Devices and Sensors Laboratory (FEDSLab) and the Additive Manufacturing Laboratory (ADDLab) at NJIT during my time as a PhD student. They suggested over tea at Fakebucks, if you know you know, that I reach out to John F. Federici and Ian Gatley in order to work at their lab as a research assistant. Over the course of a year and a half, I had the pleasure of contributing to their research group by applying things I learned at the DMS. In return, I had the chance to appreciate many of the practical aspects of numerical optimization and learn how to constructively and productively work with experimentalists and engineers. Many of this dissertation's results are indebted to the maturity in my methodology I experienced while working at FEDSLab.

Of course, without early inspirations for delving into the mathematical sciences, I would not have made it this far. My interest in math really started to take shape in third grade, thanks to Mr. Robert Silvera, and at Boonton High School during geometry class. I would like to thank the late Mr. William Reichler for exposing me to M.C. Escher's fractal and hyperbolic geometry, and for his insistence on stapling exams in the right corner. If you ever asked him why he would staple his exams on the "wrong side", he would stare at you with a smile and say "What do you mean? It's on the right side." I would also like to thank Coach Dave Hughen, Al Bellini, Bob Davis, Linda Snow, and Angelo Questa for their continued excellent guidance throughout and after high school.

I then continued my studies at the County College of Morris. I loved this school and have many fond memories of making friends and learning there. I first learned calculus from the late Robert Gebhardt. He had a reputation of really challenging his students, and I'm extremely grateful that I had the opportunity to learn from him while it was still possible. I learned physics from John Klages who, I still think, delivers the most compelling physics lectures I've ever attended. These men have inspired me to continue learning science well into today.

I would also like to thank the professors who guided me through an education at NJIT. Specifically, the instruction and guidance of Andres Jerez, Bruce Bukiet, Yassine Boubendir, Amit Bose, Catalin Turc, Lou Kondic, Cyrill Muratov, Tao Zhou, Brittany Froese-Hamfeldt, Denis Blackmore, Michael Booty, and Linda Cummings were all impactful. The obvious care and attention they put into their curricula greatly softened the difficulty of pursuing research in mathematical science for me. In addition, without the continued support of the DMS, this dissertation would not have been possible. Michelle, Alison, Pauline, Rey, Amy, and Wil were always ready to help.

I was fortunate enough to make several friends while studying at NJIT. I would really like to first thank Brandon Behring for his kindness. Being that we shared the same advisor, and he was one year ahead of me in the program, Brandon helped me to get through various stages of the program while avoiding many of the pains he had to endure. Senior students, and now graduates, Valeria Barra, Michael Lam, Ivana Seric, and Aminur Rahman were also extremely helpful in answering a lot of my questions while I was still early on in the program. I would also like to acknowledge my friends Vladimir, Erli, Binan, Axel, Tensae, Jake, Yixuan, David, Elly, Tadanaga, Prianka, Malik, and Tore for our fruitful interactions as peers.

I should also acknowledge the Graduate Student Mathematical Modeling Camp that was held at the Rensselaer Polytechnic Institute. I learned a lot about thinking like an applied mathematician from working in Donald Schwendeman's group. This greatly encouraged me to participate in the Mathematical Problems in Industry Workship in 2017 and 2019 held at NJIT. I would like to specifically acknowledge the encouragement of Tom Witelski and Dean Duffy in working on the problem provided by Corning, Inc. and Zhenyu He's guidance with working on Gore's problem. This experience has been invaluable.

Lastly, the support and love of my immediate family has been the most fundamentally important aspect of my life. My father Jaime, my mother Sonjie,

my three brothers Jayson, Jessie, and Justin have always been there for me even through the really rough times. I can only hope that the work I've done here makes them proud.

TABLE OF CONTENTS

Chapter **Page**

TABLE OF CONTENTS
(Continued)

Chapter **Page**

TABLE OF CONTENTS
(Continued)

Chapter **Page**

LIST OF FIGURES

Figure **Page**

LIST OF FIGURES
(Continued)

Figure **Page**

LIST OF FIGURES
(Continued)

Figure **Page**

LIST OF FIGURES
(Continued)

Figure **Page**

LIST OF FIGURES
(Continued)

Figure **Page**

LIST OF FIGURES
(Continued)

Figure **Page**

LIST OF FIGURES
(Continued)

Figure **Page**

LIST OF FIGURES
(Continued)

Figure **Page**

CHAPTER 1

INTRODUCTION

1.1 The Relevance of Optimal Control Theory in Today's Technology

Optimal control theory is a branch of applied mathematics where the main goal is to determine a control policy, in some suitable class of functions, such that a clearly defined objective or measure of performance involving the state of some dynamical system is considered optimal. The theory, which is an extension of the classical calculus of variations, provides a framework for determining optimality as well as methods for computing optimal control policies.

The necessary and sufficient conditions for optimality in a general class of problems constrained to finite-dimensional dynamical systems goes back to the 1950's through the independent works of the Jewish-American applied mathematician Richard Bellman and Russian-Soviet mathematician Lev Pontryagin. Given the historical context of the Cold War, it is interesting to note one of the first applications of Pontryagin's optimal control theory was the maximization of a rocket's terminal speed [25] while Bellman used his theory of dynamic programming to study "games of survival" [6]. Because of its general framework, optimal control theory continues to impact most scientific fields such as biology, economics, ecology, engineering, finance, management, and medicine. Therefore, the utility of optimal control theory for designing technology and policies in a wide and diverse number of fields cannot be understated.

The aim of this dissertation is to apply methods of deterministic optimal control theory to problems arising from the technological desire of controlling coherent dispersive wave phenomena. We investigate the applications of such control problems to transforming quantum fluids trapped by external magnetic fields, reshaping laser beams in refractive wave-guides, and manipulating optical solitons in periodic photonic crystals.

Of course, optimization problems constrained by infinite-dimensional systems, such as the ones we consider, are both theoretically and computationally much more challenging than problems constrained by finite-dimensional systems. Proving well-posedness of important control problems and constructing computationally tractable strategies for finding optimal controls in high-dimensional settings remains an active area of research within applied mathematics. This dissertation, and its initial focus of research, is motivated by our humble desire to understand the recent work by others on the optimal control of Bose-Einstein condensates.

1.2 Interpreting Quantum Control Problems From the Past Decade

Quantum optimal control, as it has come to be known in the literature, concerns itself with the control of N-body quantum systems. An important example of such a control problem is the reshaping of a dilute atomic Bose-Einstein condensate (BEC). Since they were observed in laboratory experiments in the 1990's, BECs, an ultra-cold quantum fluid whose mean dynamics resemble that of a single atom, have proven to be an experimentally reliable and versatile platform for high-precision storage, manipulation, and probing of interacting quantum fields. It is likely that future technologies involving quantum computation, simulation, and metrology will be dependent on the fast manipulation of BECs [46].

Experimentalists over the last two decades have achieved remarkably high, yet sub optimal degrees of control of BECs by using empirical rules of thumb and intuition gained from significantly reduced models admitting closed-formed solutions [72]. Meanwhile, optimal control theory provides a computational framework for systematically finding highly efficient control policies. This is demonstrated numerically in three spatial dimensions in the work by Mennemann et al. [46] which depends on the seminal work due to Hohenester [34] which we will outline shortly.

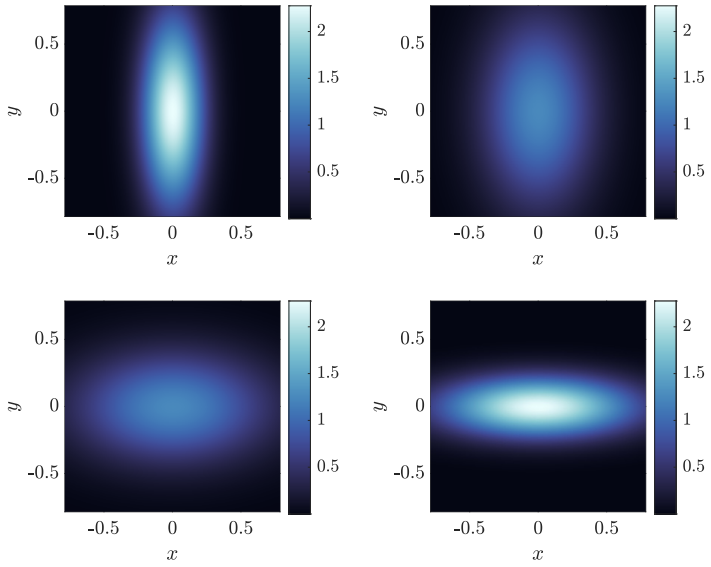

Figure 1.1 An example of rotating a BEC. Shown here are density distributions $|\psi_{\text{Gaussian}}|^2$ as they are rotated from the initial vertical state with $a = 10$ and $b = 1$ to the desired horizontal state with $a = 1$ and $b = 10$.

An example of a BEC manipulation studied by Mennemann, et al., is a rotation of a BEC facilitated by squeezing and elongation. The goal of this experiment is to reorient the magnetic field confinement concentrated along one axial direction to another axial direction which in turn reorients the density distribution of the condensate. A two dimensional example of this is shown in Figure 1.1 with normalized Gaussian wavefunctions of the form

$$\psi_{\text{Gauss}} = \sqrt[4]{\frac{ab}{\pi^2}} e^{-ax^2-by^2}, \tag{1.1}$$

where $a, b > 0$ and $(x, y) \in \mathbb{R}^2$. Another manipulation Mennemann et al. consider is one which topolgically changes the support of the wavefunction. An example of this is shown in Figure 1.2 where a Gaussian wavefunction (1.1), with $a = b = 1$, is mapped to the normalized toroidal wavefunction

$$\psi_{\text{Toroid}} = \frac{2}{\sqrt{3\pi}} r e^{-r}, \tag{1.2}$$

where $r = x^2 + y^2$.

Manipulating the condensate will, in general, excite oscillations in the mean field of the condensate and distort any intended coherence of the transformed distribution after the control process has terminated. This dissertation considers these types of manipulations when we attempt to control BEC optimally.

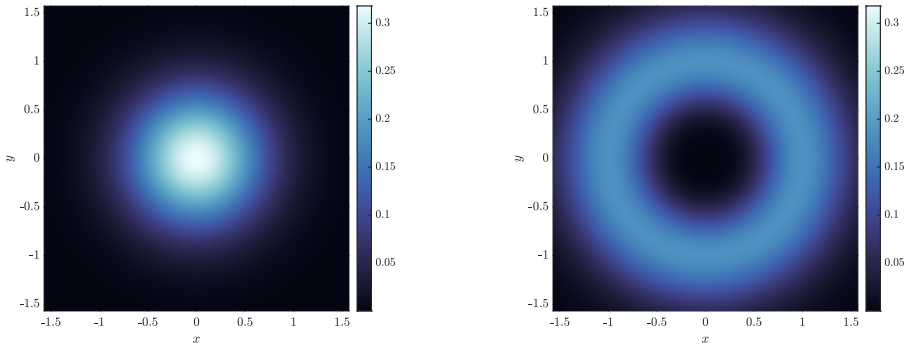

(a) (b)

Figure 1.2 An example of topologically changing the condensate's support. Panel (a) shows the initial distribution $|\psi_{\text{Gaussian}}|^2$ with $a = b = 1$ while panel (b) shows the desired distribution $|\psi_{\text{Toroid}}|^2$.

The, now standard, optimal control problem which addresses these distortions, first proposed by Hohenester [34], is one which maximizes the fidelity between an evolving field ψ at a final time T and an experimentally-desired state ψ_d, subject to a control function u. This problem, expressed in dimensionless form, is

$$\inf_{u\in\mathcal{U}} J = \frac{1}{2}\inf_{u\in\mathcal{U}}\left\{1 - |\langle\psi_d(x), \psi(x,T)\rangle|^2_{L^2(\mathbb{R}^3)} + \gamma\int_0^T |\dot{u}|^2 dt\right\}, \tag{1.3}$$

subject to the mean field dynamical system

$$i\psi_t = -\frac{1}{2}\Delta\psi + V(x,u(t))\psi + |\psi|^2\psi, \tag{1.4a}$$

$$\psi(x,0) = \psi_0(x) \in H^1\left(\mathbb{R}^3\right), \tag{1.4b}$$

where the wavefunction $\psi(x,t)$ belongs to $L^2\left([0,T]; H^1\left(\mathbb{R}^3\right)\right)$, ψ_0 is some initial quantum state, Δ is the Laplacian operator, $V(x,u)$ models the geometry of confinement as a potential energy parameterized by the control $u(t)$, $\mathcal{U}$ is an

admissible class of control parameters $u \in H^1([0,T])$ with fixed initial and terminal conditions, $L^2(\Omega)$ is the space of square Lebesgue-integrable functions over the measurable set Ω, and $H^1(\Omega)$ is the Sobolev space of once weakly differentiable $L^2(\Omega)$ functions whose first weak derivatives are also in $L^2(\Omega)$. Recall that wave functions are typically normalized to have a unit $L^2(\Omega)$ norm. Therefore, we also require that $||\psi||_{L^2(\mathbb{R}^3)} = 1$.

The dynamical constraint (1.4a) is known as the Gross-Pitaevskii equation (GPE), and the confining potential $V(x, u(t))$ arises due to an applied optical or magnetic field. How the constraint arises as a model of the mean-field dynamics of BEC is discussed in detail in [53]. The objective J in Equation (1.3) has two contributions which, after ignoring the factor of a half, are the *infidelity*, defined as $1 - |\langle \psi_d(x), \psi(x,T)\rangle|^2_{L^2(\mathbb{R}^3)} \in [0,1]$ and the *regularization*, defined as $\gamma \int_0^T |\dot{u}|^2 dt$. The infidelity is a type of terminal cost which penalizes control policies that miss the desired wave function ψ_d. The regularization is a type of running cost which penalizes the usage of physically undesirable controls with fast variations. We provide more details in Section 2.2 about how optimal control problems are generally posed with objectives involving terminal and running costs.

A more general control problem defined through the Hohenester objective (1.3) and mean field constraint (1.4a), along with a running cost which also penalizes the amount of work done by the control, was shown to be well-posed by Hintermuller, et al., for approriately chosen values of γ [33]. The bulk of the rigorous mathematical justification for the optimal control of mean-field BEC, as well as the work carried out in this proposal, relies on well-posedness results such as these. For this reason, we will simply state in which function space our computations are carried out and provide limited mathematical detail otherwise. This frees us to focus on the physical and technological applications, modeling, and development of numerical techniques.

Mennemann, et al., numerically study experimentally motivated transformations of $\psi(x,t)$, such as the ones in Figure 1.1 and Figure 1.2, by solving

the associated optimal control problem, after setting $\gamma = 10^{-6}$, with a projected gradient method called **Gr**adient **A**scent **P**ulse **E**ngineering, or GRAPE for short; Subsection 2.4.4 discusses the idea of GRAPE as it was implemented in this dissertation. Their work is the source of inspiration for the first problem of study.

Problem 1: Optimal Control of Bose-Einstein Condensates The first problem this dissertation considers is the coherent control of BEC. Our primary goal has been two-fold when attempting to understand this problem: can we gain further physical intuition of the condensate dynamics as it is controlled, and can we use this physical insight to implement optimization strategies in some easier, i.e., finite-dimensional, computational setting?

To address these goals, we introduce a Galerkin ansatz which incorporates the time-dependent nature of the confining potential, and use this as a means to study two model problems: the optimal squeezing of a BEC in a quadratic potential and the optimal splitting of a BEC by a time-dependent barrier. These model problems are posed in one spatial dimension and are representative of the salient features of the rotation problem 1.1 and splitting problem 1.2.

This work is the subject of Chapter 3 which begins by describing our approach on modeling the squeezing and splitting problems. We show how the associated finite-dimensional dynamics are constructed, justified, and further simplified. We carefully show how the dynamics of the controlled condensate can be reduced to just a single non-autonomous degree of freedom Hamiltonian system. In the subsequent section of Chapter 3, we precisely define an objective for the optimal control of finite-dimensional Hamiltonian systems. We suggest the general minimization of any reasonable enough function of the canonical coordinates, time, and controls after the dynamics have evolved for some time $T > 0$, and specialize to the physically relevant case of when the function of interest is the Hamiltonian that generates the dynamics. We then derive the necessary optimality conditions for this class of Hamiltonian control problems.

The resulting optimal control problem is non-convex. A technique called multi-starting, i.e., sampling the space of initial controls in an ad hoc way for the purposes of a local optimization method, is often used to overcome the nonconvex nature of optimal control problems. Instead, we pursue a more systematic approach which makes use of a hybrid optimization method that couples the use of genetic algorithms, inspired by the work of Storn and Price [64], and GRAPE in order to find controls which are more likely to be globally optimal. These methods are used to solve the finite dimensional BEC optimal control problems of this chapter and are explained in greater detail in Section 2.4. Once we apply the techniques of Section 2.4 to solve these control problems, we solve the Gross-Pitaevskii equation (1.4a) using the resulting computed controls to see if they effectively control the full dynamics. We interpret the results and make quantitative conclusions about the effectiveness of our overall strategy.

Moving forward, we turn our attention from control of quantum many-body systems to the design of photonic technology using optimal control theory. We aspire to contribute to the photonics community by adopting and modifying the tools we acquired from studying BEC control problems. The first photonics problem we consider is the reshaping of light propagating in a waveguide, and we specifically thank Professors Braxton Osting and Alejandro Aceves for providing this problem for us.

1.3 Designing Photonic Technology

Problem 2: Reshaping Light in Diffractive Wave Guides Reshaping light remains an active area of research despite having been extensively studied over thousands of years from the introduction of primitive lenses by the Ancient Assyrians circa 750 B.C.E [1] to designs based on the sophisticated techniques of optimal transport [24]. Requiring a laser beam to have a specified irradiance distribution has diverse and broad applications which include laser/material processing, laser/material interaction studies, fiber injection systems, optical data

image processing, and lithography [22]. Geometric optics is the simplest physical setting in which to study beam reshaping, and one that is often chosen. However, the wave nature of light cannot be neglected when diffractive effects are present as is often the case in nano-scale optical technologies.

Diffraction is taken into consideration in a recent paper by Kunkel and Leger [36]. They demonstrate that the so-called phase retrieval method is a viable means for numerically constructing a gradient-index (GRIN) optical fiber which reshapes light to an intended intensity distribution. An example of light reshaping Kunkel and Leger consider, and we show in Figure 1.3, is one which transforms sharply peaked intensity profiles to nearly uniform ones.

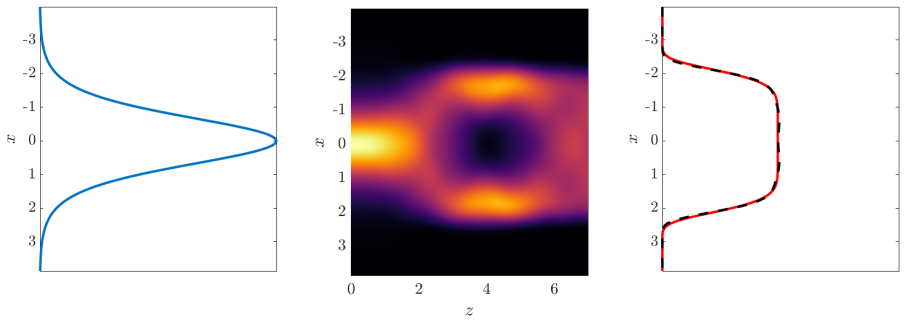

Figure 1.3 An example of reshaping light with a peaked intensity profile into one with a more uniform profile. Chapter 4 details the methods used to find such a mapping.

For purposes of modeling, consider an electromagnetic field propagating transversely through a linear waveguide, i.e., a waveguide through which the electrical field responds linearly to the polarization of the propagation media. Assuming time-harmonic fields with negligible magnetic fields components satisfying the assumptions of the paraxial approximation, namely, that the direction of propagation does not deviate much from the axial direction defined by the waveguide, one can show [30] Schrödinger's equation (in dimensionless form)

$$i\psi_z = -\frac{1}{2}\Delta_\perp \psi + V(x, u(z))\psi, \tag{1.5}$$

arises from the inhomogeneous, variable-coefficient Helmholtz equation. Here, z is the axis of propagation, x is the transverse direction, $\Delta_\perp$ is the Laplacian in the transverse directions, $V(x, u(z))$ is proportional to a spatially varying refractive index, and ψ is a spatially varying complex electric amplitude. The numerical solution of Schrödinger's equation is significantly cheaper computationally than either the full numerical solution of Helmholtz's or Maxwell's equations. It is for these reasons, one often commits to studying optical problems in the paraxial limit. Also, it is clear that reshaping light in the Schrödinger optics regime naturally calls for the use of quantum optimal control.

The light reshaping problem we consider seeks to find potentials $V(x, u(z))$ that transform the amplitude ψ as it evolves axially into a transverse stationary state, i.e., a function φ_d such that

$$-\frac{1}{2}\Delta_\perp \varphi_d + V(x, u(l))\varphi_d = \lambda \varphi_d, \quad \varphi_d \in L^2(\Omega_\perp), \quad \lambda \in \mathbb{R}, \tag{1.6}$$

at the end of some propagation length l. This feature is highly desirable if the mode is to then continue propagating through a wave guide since in this case its absolute value will remain invariant as it evolves axially in z.

Our attempts to solve the light reshaping problem is the subject of Chapter 4 and is organized as follows. The first section precisely states the optimization problem, which is nearly identical to the quantum optimal control problems considered by Hohenester [34], with the distinguishing feature being that the constraints are drawn from a slightly more general class of linear dispersive wave equations. The intention of the stated problem is to map the n^{th} eigenfunction of an appropriately defined linear operator to the n^{th} eigenfunction of another linear operator.

In the subsequent section, we specialize to the case where the linearly dispersive constraints are given by Schrödinger's equation (1.5) and provide a proof of concept in the form of a contrived, yet representative, numerical experiment. Again we use the optimization methods described in Section 2.4 in order to

numerically solve the optimal control problem. We then focus on solving the light reshaping problem shown in Figure 1.3 and pulse combining problem shown in Figure 1.4.

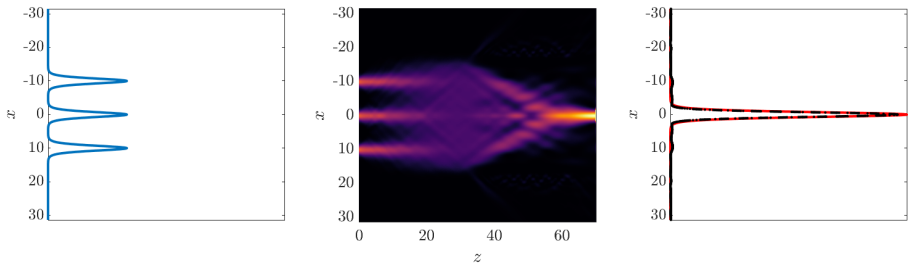

Figure 1.4 Another example of light reshaping. Here, we combine three pulses into one using optimal control theory. More detail is provided in Chapter 4.

Problem 3: Optimal apodization of Bragg gratings Another photonics problem we consider in this dissertation is the excitation and control of optical solitons; coherent pulses of localized light balanced by dispersive and nonlinear focusing effects, in fiber Bragg gratings (FBGs). FBGs are typically short optical elements in optical fibers with a periodic variation of the refractive index, called a grating, along an optical fiber. The fiber grating strongly couples forward and backward propagating waves from successive Fresnel reflection and transmission, or simply a Bragg resonance, leading to an exponential attenuation of a specific band of frequencies. Therefore, FBGs can act as a wavelength-specific bandstop filter.

Meanwhile, the optical dynamics are richer when nonlinearities arising from the optical Kerr effect are significant. This typically manifests itself as self-phase modulation, a self-induced phase- and frequency-shift of light, but also manifests in the cross-phase due to the grating's coupling of forward and backward propagating waves. This can lead to strongly focused light, yet when balanced with dispersion,

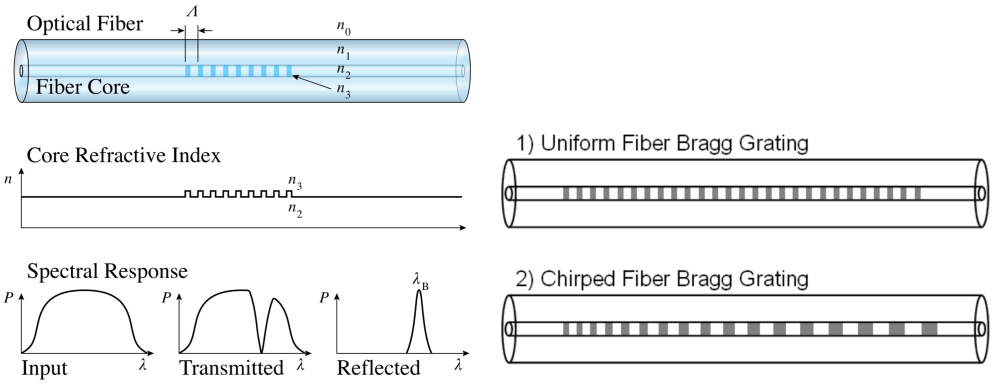

Figure 1.5 A visualization of Fiber Bragg Gratings (FBG's). Because of Bragg's law, the transmission and reflection in the spectrum is dependent on the spacing Λ in the way as it is shown in this figure. Part of this proposal involves constructing chirped gratings, and so we provide a basic picture of what is meant by that here. This figure was provided to Wikipedia by users Sakurambo and Grahamwild and is licensed under the Creative Commons Attribution-ShareAlike 3.0 License.

allows for the possibility of solitary waves; a self-reinforcing wave packet that maintains its shape while it propagates at a constant velocity.

The manipulation of solitary waves using FBGs is generally quite difficult because of the strong reflection of frequencies in the photonic stopband. Fortunately, an apodization of the grating, i.e., introducing a spatially varying index of refraction, can be used successfully to mitigate the strong Bragg reflection of solitary waves. This technique allows for the possibility of dramatically slowing light while compressing the width of its support by several orders of magnitude.

Dispersion compensation and pulse compression is essential in applications that involve high-resolution multi-photon microscopy [2]. In addition, modern optical communications systems use FBGs as notch filters or as components in optical add-drop multiplexers [4]. Since information is transmitted as coherent pulses of light in optical fibers, these pulses need to be manipulated or redirected as they travel. Therefore, technology that can significantly slow down, or even halt, solitary waves is highly desirable.

In a series of papers, Rosenthal and Horowitz, [56], [57], outline an apodization method for exciting highly compressed solitary waves with a central frequency near the Bragg resonance in the forbidden band gap. These waves,

called gap solitons, can be excited by propagating a very wide low intensity pulse toward an apodized grating. This leads to significant compression of the incident light, and pulse compression techniques such as these may be promising in future photonics devices where loss of coherence through dispersion is significant. An example of this excitation scheme is shown in Figure 1.6:

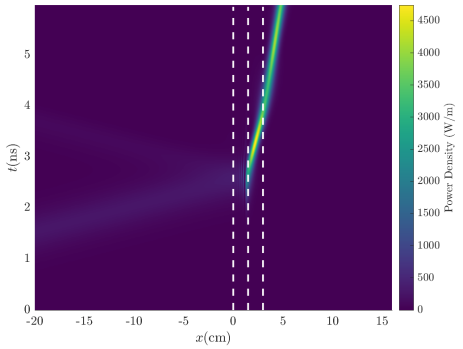

Figure 1.6 A numerical simulation of the Rosenthal and Horowitz experiment from [56] where a gap soliton has been excited by a specific FBG design. Dashed lines indicate regions where the two segment apodization varies spatially. We discuss, in greater detail, experiments of this type in Chapter 5.

Rosenthal and Horowitz [57] claim that their method is efficient. Despite achieving an increase in the pulse-transmission of an excited gap soliton from 20-30% [48] to around 70%, the work of Rosenthal and Horowitz leaves room for improvement. We investigate to what extent this method is efficient with the goal of designing our own FBG apodizers which suffer less severely from losses due to fiber Bragg back reflection such as in Figure 1.6. In Chapter 5, we outline the physical models used, precisely define an objective with the intention to maximize excited pulse energy transmission, and present our numerical results.

Problem 4: Optimal Control of Nearly-Integrable Systems We find, after studying the control of excited Bragg solitons in Chapter 5, some of the energy coupled into the grating is incoherent. By this, we mean, the energy escapes from the localized support of the Bragg soliton on long enough time scales. To address this, we construct control strategies that exploit the general mathematical structure of the types of equations that support solitons as exact

solutions. Improving upon the results of Chapter 5 is the impetus behind our research of optimal control of solitons in nearly-integrable settings.

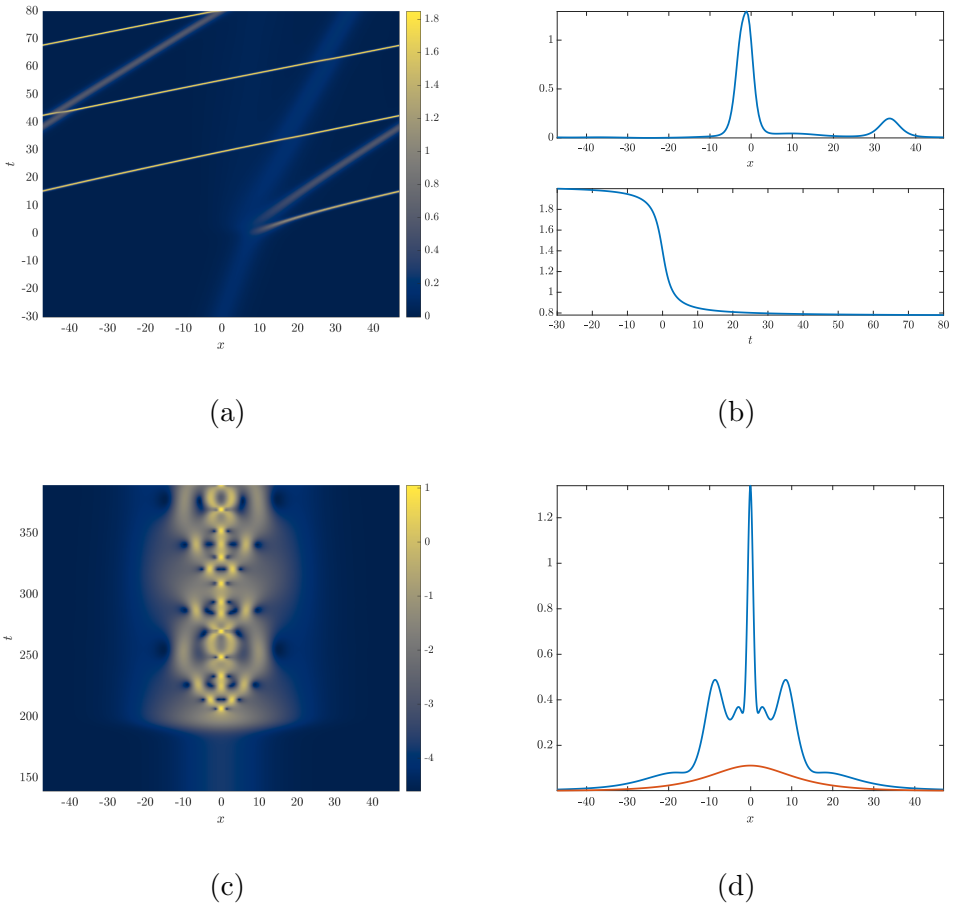

Figure 1.7 Numerical solutions of the nearly integrable KdV equation (1.7), Panel (a) and Panel (b), and NLS equation (1.8), Panel (c) and Panel (d), for some localized disturbances $\varepsilon(t)$ explained in greater detail Chapter 6. The solutions at the final computed time, panels on the right, show filtering unwanted mass from the primary soliton data generally requires careful consideration.

The existence of solitons has a long and storied history [52] and is an indicator of an infinite number of conserved quantities and so-called integrability. Equations with such properties have deep mathematical structure and several interesting properties. While gap solitons are not classical solitons, the two are related. The basic governing equations of light propagating through FBG's, the non-linear coupled mode equations (NLCME), are related, in some way, to two integrable systems: the non-linear Schrödinger (NLS) equation and the massive Thirring model (MTM).

In Chapter 6, we focus on studying the optimal control of classical solitons in inhomogeneous media. There, we propose a method based on a spectral decomposition of total mass into the mass carried by solitons and the mass of the incoherent radiation. Decompositions of this type are expressed through the so-called trace formulae [52], which we discuss in Appendix C, and can be roughly interpreted as a type of nonlinear filtering of incoherent energy from coherent soliton data.

In Section 6.2 and in Figure 1.7, we numerically demonstrate some of the generic phenomena one can expect when studying nearly-integrable equations such as the perturbed Korteweg-deVries (KdV) equation

$$\partial_t q + 6q\partial_x q + \partial_x^3 q = \varepsilon(t) q \tag{1.7}$$

and perturbed NLS equation

$$i\partial_t \psi_t + \frac{1}{2}\partial_x^2 \psi + |\psi|^2 \psi = \varepsilon(t)\psi. \tag{1.8}$$

By nearly-integrable, we mean the Cauchy problem involving these equations is exactly solvable in the absence of the time-localized disturbance $\varepsilon(t)$. In subsequent sections, we then present the soliton-specific control problem for the KdV equation (1.7) since this is the simplest and earliest model problem of a Hamiltonian system solvable by means of the Inverse Scattering Transform (IST) [26].

Equipped with a soliton-specific control framework, we revisit the problem of designing FBG in Chapter 7. We begin by showing how we can model the dynamics of light in FBG by an inhomogeneous NLS equation. In Figure 1.8, we visually demonstrate the basic approach which takes advantage of an appropriate characteristic coordinate. Once we have a model dispersive wave equation at our disposal, we treat this as the constraint in our soliton control framework. We conclude with results from our methodology and leave open the possibility for future work.

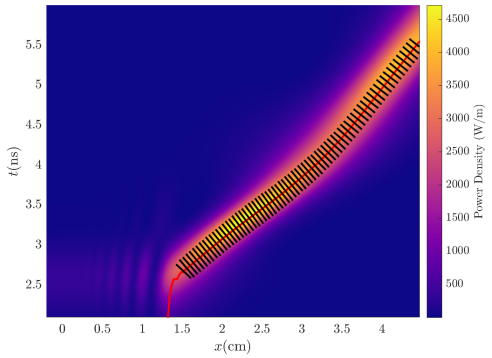

Figure 1.8 Tracking the wave front shown in Figure 5.3. We show, in Chapter 7, along the characteristic coordinates, drawn in black, the dynamics can be modeled by an NLS-type equation.

CHAPTER 2

ANALYTICAL FORMULATION OF OPTIMAL CONTROL PROBLEMS AND NUMERICAL TECHNIQUES

2.1 A Brief History of Variational Problems

Problems involving the extremization of a given functional has a long and storied history which can be traced back to antiquity when Queen Dido famously solved a type of isoperimetric problem in founding the city of Carthage circa 8^{th} century BCE [74]. However, a rigorous proof of her solution would not appear until the European scientific revolution after the methods of calculus and mathematical analysis emerged [76]. The first functional optimization problems considered during this time were Newton's minimal resistance problem in 1687 [62] and the Brachistochrone problem in 1696 [8]. Although these problems were solved by various geometric methods, Leonhard Euler provided both a general framework and necessary conditions for extrema in 1731. Euler named this branch of mathematics the calculus of variations in 1756 after Joseph Louis Lagrange provided the more systematic method of variations when Lagrange was just 19 years old [29]. Eventually, in 1879, Karl Weierstrass provided necessary and sufficient conditions which classified these variational extrema as strong relative minima building on earlier work by Adrien-Marie Legendre, Carl Gustav Jacob Jacobi, and many others [68].

In the early 1900's, Stanisław Zaremba provided existence proofs of minimizers and his methods were later extended by David Hilbert and Leonida Tonelli [71]. This led to the development of the so-called direct method of the calculus of variations which is still widely used today [39]. Although the question of existence could be dispensed with as a mere subtlety, the danger of assuming the existence of an optimization problem is clear from the following amusing paradox due to Oskar Perron: "Let N be the largest positive integer. If $N > 1$, then $N^2 > N$, contradicting the definition of N. Hence $N = 1$".

The calculus of variations, as a subject of pure and applied mathematics, continued to remain relevant. Hilbert posed three problems, of his now famous 23, which further stimulated research. The 20^{th} problem, solved in a culminating effort by several mathematicians throughout the 20^{th} century, involves further developments in techniques for proving existence of minimizers and their connections to boundary value problems [61] while the 19^{th} problem, solved in 1957 by Ennio De Giorgi [18] and John Forbes Nash [51], independently, is concerned with regularity of solutions belonging to a particular class of variational problems. The last of the three problems, problem 23 on Hilbert's list, is simply encouragement for further research in variational calculus:

"So far, I have generally mentioned problems as definite and special as possible.... Nevertheless, I should like to close with a general problem, namely with the indication of a branch of mathematics repeatedly mentioned in this lecture-which, in spite of the considerable advancement lately given it by Weierstrass, does not receive the general appreciation which, in my opinion, it is due—I mean the calculus of variations."

— David Hilbert, 1900 [32]

In order to illustrate a basic problem in the calculus of variations, consider the following class of variational problems in Lagrange form:

$$\inf_{x\in\chi} \mathcal{J}_{\mathcal{L}}[x] = \inf_{x\in\chi} \left\{ \int_0^T \mathcal{L}\left(x(t), x'(t), ..., x^n(t), t\right) dt \right\} \tag{2.1}$$

where the time parameter $t \in (0,T) \subset \mathbb{R}$, T is called the time horizon, the Lagrangian functional $\mathcal{J}_{\mathcal{L}} : \chi \to \mathbb{R}$ models some geometric or physical scenario, and the admissible function space $\chi = \{x \in C^n(0,T) : x(0) = x_0,\ x(T) = x_T\}$ specifies the regularity restrictions and boundary conditions of the curve $x(t)$. The necessary optimality condition, the Euler-Lagrange equation, for this problem is

$$\sum_{j=0}^{n} (-1)^j \frac{d^j}{dt^j}\left(\frac{\partial \mathcal{L}}{\partial x^j}\right) = 0, \tag{2.2}$$

where x^j is short-hand for the j^{th} derivative of $x(t)$ with respect to t.

A simple example to consider is the minimization of the arclength function $\mathcal{L}(x'(t)) = \sqrt{1+x'^2}$. Using Equation (2.2), it is easy to show that the linear function $x(t) = c_1 t + c_2$, where c_1 and c_2 are arbitrary constants, extremizes the arclength functional. Although it is obvious to state a straight line is the curve with minimum arclength, one could in principle show lines are truly minimizers, and not just an extremizer, by applying Weierstrass's conditions [68]. In general, computing minimum length paths or minimal area surfaces is typically much more challenging, and is an important task in fields such as differential geometry, image processing, and Einstein's theory of relativity.

Another brief application is to let $\mathcal{L}(x(t), \dot{x}(t)) = \frac{1}{2}\dot{x}^2 - V(x)$, in Newton's notation, where V is a potential energy, so that Equation (2.2) implies Newton's second law: $\ddot{x} = -\partial_x V$. This was first observed by Lagrange in 1788 and helped pave the way toward Hamilton's least action principle of classical mechanics; the least action principle has served as a fundamental tool of mathematical physics and analysis of partial differential equations (PDE) ever since. Broad areas of mathematical physics ranging from potential theory to quantum mechanics make use of variational principles [39]. For these reasons, the calculus of variations was still an active area of research throughout most of the 20^{th} century and its importance is reflected through its inclusion in Hilbert's famous problem set.

2.2 Structure of Deterministic Optimal Control Problems

Up until the middle of the 20^{th} century, variational problems remained challenging, yet had become somewhat mathematically routine [45]. However, in the 1950's, Lev Pontryagin and his students considered a reformulation of variational problems which revitalized the field. Moreover, this reformulation, the optimal control formulation, is better adapted for problems in the applied sciences and technology. Previous formulations consider the path of a moving point, and its motion controlled by the value of its momentum $\dot{x}(t)$ for each moment of time. However, in

design problems typical of engineering and economics, one cannot choose momenta arbitrarily because of underlying dynamic constraints. The critical idea of control theory is to instead search for a parameter $u(t)$ which determines $\dot{x}(t)$. In this sense, the state x of the system together with its momentum $\dot{x}$ are responses to a single set of control functions u. This framework is more general, can handle dynamic constraints, and is more computationally straightforward from a numerical standpoint.

Throughout this dissertation, our focus is on modeling design problems from scientific experiments as optimal control problems, such as the optimization problem with Objective (1.3). In this section, we describe a somewhat general structure of the optimal control problems studied in this dissertation, and provide a greater level of detail and the appropriate modifications as we come across each problem in later chapters.

To this end, let ψ be the state of a dynamical system constraint in a (generally) complex Banach space $\mathcal{B}_\psi$, let an admissible class of control functions be $\mathcal{U} = \{u \in \mathcal{B}_u : u(0) = u_0, u(T) = u_T\}$, where u_0 and u_T are specified boundary values for the control policy u, and let $J : \mathcal{B}_\psi \times \mathcal{U} \to \mathbb{R}$ be an objective functional which is to be minimized. The problem structure mainly considered throughout this dissertation is of the form

$$\inf_{\psi \in \mathcal{B}_\psi, u \in \mathcal{U}} J[\psi, u] = \inf_{\psi \in \mathcal{B}_\psi, u \in \mathcal{U}} \left\{ \mathcal{G}(\psi)\Big|_{t=T} + \int_0^T \mathcal{F}(\partial_t u) dt \right\}, \tag{2.3}$$

subject to

$$\partial_t \psi + \mathcal{P}(\psi, u) = 0, \qquad \text{(Differential Equation Constraints)} \tag{2.4a}$$

$$\mathrm{d}(\psi) = 0, \qquad \text{(Boundary and Initial Data)} \tag{2.4b}$$

where $\mathcal{P}$ is a generally nonlinear differential operator such that the constraining dynamics given by Equation (2.4a) are dispersive [77].

Note that a solution of the constraints (2.4) corresponding to a control $u \in \mathcal{U}$ induces a map

$$\psi : \mathcal{U} \to \mathcal{B}_\psi : \quad u \mapsto \psi(u).$$

Therefore, the previous optimal control problem can be equivalently stated as an unconstrained optimization problem over the control function u, i.e.,

$$\inf_{u \in \mathcal{U}} \mathcal{J}[u] = \inf_{u \in \mathcal{U}} \left\{ \mathcal{G}(\psi(u))\Big|_{t=T} + \int_0^T \mathcal{F}(\partial_t u) dt \right\}, \tag{2.5}$$

by making use of the so-called reduced functional

$$\mathcal{J} : \mathcal{U} \to \mathbb{R}, \quad u \mapsto \mathcal{J}[u] := J[\psi(u), u]. \tag{2.6}$$

Optimal control problem (2.5) is a version of the so-called fixed time, free endpoint problem studied by Pontryagin, et al., and a simpler, finite-dimensional version is discussed further in Section 2.3.1. The first term of $\mathcal{J}$ is called a terminal cost and penalizes control policies which fail to drive ψ to the state which minimizes $\mathcal{G}$ at $t = T$. Sometimes, the terminal cost is referred to as a soft constraint since it can be viewed as a relaxation of the hard constraint $\psi\big|_{t=T} = \psi_T^* := \arg\min \{\mathcal{G}\big|_{t=T}\}$ used in the so-called free time, fixed endpoint problem [38]. The second term is called a running cost which we use to regularize the control u. This relaxes the use of inequality constraints on u, which simplifies the analysis and numerical study of the control problem. The typical choice we make is $\mathcal{F}(z) = \frac{\gamma}{2} z^2$, $\gamma > 0$, and is a type of Tikhonov regularization. This penalizes controls which rapidly vary and often ensures the optimal control problem remains well-posed, i.e., that solutions exist in the admissible space $\mathcal{U}$ [33]. We will make further remarks about the role of Tikhonov regularizations and typical choices of the parameter γ in Section 2.3.4. In the context of classical problems from the calculus of variations, optimization problem (2.5) is known as a Bolza problem [27].

After posing a Bolza control problem, we are of course tasked with solving it. However, solving Bolza problems can be quite challenging since the admissible classes $\mathcal{B}_\psi$ and $\mathcal{U}$ are, in principle, infinite-dimensional. Exact solutions are often impossible to find, and numerical solutions may be extremely computationally intensive. Fortunately, many efficient solution strategies exist for solving Bolza problems. These methods can be generally classified into three families: indirect, direct, and dynamic programming methods.

2.3 Survey of Existing Optimal Control Paradigms and Available Strategies

2.3.1 Indirect Methods and Pontryagin's Principle

"The [maximum] principle was, in fact, the culmination of a long search in the calculus of variations for a comprehensive multiplier rule, which is the correct way to view it: $p(t)$ is a "Lagrange multiplier" ... It makes optimal control a design tool, whereas the calculus of variations was a way to study nature."

— Francis Clarke, 1989 [16]

The discovery of the Pontryagin Principle initiated the field of optimal control theory. New and interesting research directions emerged in studies of differential equations, functional analysis, extremal problems, and computational science as a result [37]. Moreover, the principle serves as the basis for a class of numerical techniques called indirect methods.

The general philosophy of an indirect method is to "optimize then discretize." By optimize, we mean first use calculus of variations and adjoint state methods [35] in order to formally derive the necessary optimality conditions given by Pontryagin's Principle. In optimal control theory, this generally reduces the problem to the solution of a boundary value problem which is then solved by discretizing.

Although, there are numerous generalizations and alternate versions of the Pontryagin Principle, we focus on a particular basic instance of it which captures the essence of the theory relevant to this dissertation. In order to state the

principle, consider the following fixed time, free endpoint optimization problem

$$\inf_{u\in\mathcal{U}} \mathcal{J}[u] = \inf_{u\in H^1([0,T])} \left\{ g(q(T)) + \int_0^T r(q(t),u(t))dt \right\}, \tag{2.7}$$

subject to

$$\dot{q}(t) = f(t,q(t),u(t)), \tag{2.8a}$$

$$q(0) = q_0, \tag{2.8b}$$

where $f : \mathbb{R}^d \times \mathcal{U} \to \mathbb{R}^d$ is a uniformly Lipschitz continuous vector function of each q, u, and t separately on $[0,T]$ [10]. The conditions on the function f guarantees the existence of a unique state q for each control $u \in \mathcal{U}$. Further define the *Hamiltonian* function $\mathcal{H}(q,p,u) = p^{\mathsf{T}}(t)f(q,u,t) + r(q,u),\ p \in \mathbb{R}^d$, where T denotes matrix transpose. The Pontryagin Principle asserts the existence of a function p^* which is the *conjugate momentum* of the optimal trajectory q^*.

Theorem 2.3.1 *Assume u^* is an optimal control for the problem defined by objective* (2.7) *and constraints* (2.8a)*. Then there exists a function $p^* : [0,T] \to \mathbb{R}^d$ such that*

$$\dot{q}^*(t) = \partial_p \mathcal{H}(q^*(t),p^*(t),u^*(t)), \tag{2.9a}$$

$$\dot{p}^*(t) = -\partial_q \mathcal{H}(q^*(t),p^*(t),u^*(t)), \tag{2.9b}$$

$$p^*(T) = \partial_T g(x^*(T)), \tag{2.9c}$$

$$\mathcal{H}(q^*(t),p^*(t),u^*(t)) = \inf_{u\in\mathcal{U}} \mathcal{H}(q^*(t),p^*(t),u(t)). \tag{2.9d}$$

Additionally, the following saturation condition holds: $t \mapsto \mathcal{H}(q^*(t),p^*(t),u^*(t))$ is constant.

Theorem 2.3.1 is considered a milestone in the theory of optimal control [45]. In essence, it converts an optimization problem over an entire function space to the pointwise optimization problem (2.9d) which depends only on the solution of a boundary value problem defined by Equations (2.8b), (2.9a), (2.9b), and (2.9c).

An **indirect method** is an iterative method which approximates the optimality conditions of Theorem (2.3.1). In Section 2.4.5, we demonstrate how an indirect method can be used to solve a toy optimal control problem.

2.3.2 Direct and Pseudospectral Methods

Solving more general optimal control problems using an indirect method can be extremely difficult due to the curse of complexity present in additional algebraic, inequality, or non-smooth constraints [13, 59]. In addition, it can be shown that if the admissible class of controls $\mathcal{U}$ is not locally convex then indirect methods may generate erroneous solutions even in very simple contexts [58]. An alternative is to use a **direct method** where the philosophy now is to "discretize then optimize."

In general, this leads to a large-scale nonlinear programming (NLP) problem. The advantage here is that many state of the art methods exist for solving NLP problems, and many of these methods do so through approximations of the well-known Karush-Kuhn-Tucker (KKT) conditions for optimality [12]. NLP problems are typically better suited to handle more general constraint spaces and overcome issues arising from the nonconvexity of the admissible space $\mathcal{U}$. Furthermore, NLP problems are somewhat easier to understand theoretically, and therefore more accessible to a wider group of engineers, because solving them does not require functional analysis and calculus of variations.

Although direct methods offer these computational and theoretical advantages, the solutions computed in this way may fail to converge to the optimality conditions given by the Pontryagin Principle even though they converge to the KKT conditions [58]. This failure is due to the noncommutativity of dualization, i.e., writing extremal conditions through the use of a multiplier rule, and discretization. Ross, et al. [59], show how these operations can be made commutative in the context of pseudospectral methods based on Gaussian quadrature. Consequentially, pseudospectral direct methods are among the best options for solving deterministic ODE constrained optimal control problems.

2.3.3 Dynamic Programming

Dynamic programming is a general method for handling mathematical optimization and computer programming problems. The basic idea is to recursively decompose a general problem structure into sub-problems. In the context of optimal control, Bellman's principle of optimality states that "An optimal policy has the property that whatever the initial state and initial decision are, the remaining decisions must constitute an optimal policy with regard to the state resulting from the first decision" [6].

Applying Bellman's principle of optimality to the objective functional (2.3) yields the Hamilton-Jacobi-Bellman (HJB) equation [6]

$$\partial_t \mathcal{J} + \min_u \{\partial_q \mathcal{J} \cdot f(t, q, u) + r(q, u)\} = 0, \tag{2.10a}$$

$$\mathcal{J}(q, T) = g(q(T)). \tag{2.10b}$$

Once the HJB Equation (2.10a) is solved backward from the terminal condition (2.10b), Pontryagin's Principle (2.3.1) determines the optimal control u; this typically amounts to the computation of a single gradient of $\mathcal{J}$ with respect to the states q. The main advantage of this approach is that the HJB equation provides necessary and sufficient conditions for minimality. Furthermore, extensions exist for problems constrained by stochastic differential equations.

Although Bellman's approach has several theoretical advantages over the optimal control paradigms of Pontryagin and Ross, solving the HJB equation is a significant undertaking for two reasons. The first is due to the so-called curse of dimensionality. Grid based methods, such as ones built from finite-differences, are impractical when the dimension of the constraint space is large. The second obstacle is that the HJB equation typically fails to have classical solutions even for smooth input data and problem domains [5].

The theory of viscosity solutions, discovered by Crandall and Lions in the 1980's [17], adequately addresses the need for a setting in which to study HJB-

type equations. This theory was originally motivated to handle optimal control problems and has since been applied to a wide range of applied mathematics problems [5].

In addressing the computational challenge of solving the HJB equation, recent work [60] proposes deep learning techniques which overcome the curse of dimensionality inherent in grid based methods. This offers interesting future directions for extending some of our problems to a stochastic setting. However, we will not pursue dynamic programming based methods in this dissertation since they do not offer a substantial advantage for the deterministic problems of this dissertation.

2.3.4 The Role of Tikhonov Regularization

Ill-posed and ill-conditioned problems frequently arise in mathematics. Some of the problems of this dissertation are ill-posed, and so we must pursue appropriate regularizations. In order to overcome this common challenge, one often introduces a type of regularization which either converts the problem to a well-posed one or better conditions the resulting computational problem. The Tikhonov regularization technique has been successfully applied in several contexts ranging from ill-posed optimal control problems [33] to the numerical solution of poorly-conditioned integral equations [69].

The type of Tikhonov regularization we consider throughout this dissertation imposes a penalty on control functions which oscillate rapidly. In order to show how this might help condition a problem in a much simpler context, consider the following optimization problem

$$\min_{x\in\mathbb{R}^n} J = \min_{x\in\mathbb{R}^n} \left\{ \frac{1}{2} x^\mathsf{T} A x - x^\mathsf{T} b + \frac{\varepsilon}{2} x^\mathsf{T} D^\mathsf{T} D x \right\} \tag{2.11}$$

where A is a real, symmetric, and positive definite $n \times n$ matrix, $b \in \mathbb{R}^n$, D is a differentiation matrix, and ε is some small parameter. By taking the gradient of

the objective J in Equation (2.11), we see that the optimal vector x^* satisfies

$$\left(A + \varepsilon D^2\right) x^* = b \tag{2.12}$$

where D^2 is shorthand for $D^\mathsf{T} D$.

It is well-known that the condition number of a symmetric, positive-definite matrix, such as the matrix A with condition number denoted by $c(A)$, is given by the ratio of its largest eigenvalue to its small eigenvalue [65]. For this reason, we would like to better understand the effect of the Tikhonov regularizer εD^2 on the spectrum of A for small enough ε. To this end, consider the asymptotic expansions

$$\lambda(\varepsilon) \sim \sum_{j=0}^{\infty} \lambda_j \varepsilon^j \qquad \text{as } \varepsilon \to 0, \tag{2.13a}$$

$$\nu(\varepsilon) \sim \sum_{j=0}^{\infty} \nu_j \varepsilon^j \qquad \text{as } \varepsilon \to 0, \tag{2.13b}$$

where ν_0 and λ_0 are defined as the respective eigenvector/eigenvalue pair of the matrix A. To leading order, we have

$$A\nu_0 = \lambda_0 \nu_0, \tag{2.14}$$

which is automatically satisfied by the definition of ν_0 and λ_0.

To next order, i.e., $\mathcal{O}(\varepsilon)$, we have

$$(A - \lambda_0 I)\nu_1 = (\lambda_1 - D^2)\nu_0, \tag{2.15}$$

where I is the $n \times n$ identity matrix. The Fredholm alternative tells us the solvability of Equation (2.15) requires the right-hand side to be orthogonal to the left-eigenvector of A [65]. Since A is symmetric, the left eigenvector of A is simply ν_0^T. The solvability condition of Equation (2.15) is then given by

$$\lambda_1 = \frac{\nu_0^\mathsf{T} D^2 \nu_0}{\nu_0^\mathsf{T} \nu_0}. \tag{2.16}$$

Thus, the resulting condition number is

$$c(A+\varepsilon D^2)=\frac{\lambda^{\max}}{\lambda^{\min}}\sim\frac{\lambda_0^{\max}+\varepsilon\lambda_1^{\max}}{\lambda_0^{\min}+\varepsilon\lambda_1^{\min}}+\mathcal{O}\left(\varepsilon^2\right),\qquad\text{as }\varepsilon\to 0. \tag{2.17}$$

Presumably, $\lambda_0^{\min}$ is nearly 0, so as long as $\lambda_1^{\min}$ is not, the regularization has a high likelihood of being effective. Indeed, the asymptotic formula (2.17) gives a criteria for finding effective differentiation matrices, i.e., effective, $A-$specific differentiation matrices solve the following max-min problem

$$\max_{D^2\in\mathcal{D}}\min_{\nu_0\in\mathcal{V}}\left\{\frac{\nu_0^{\mathsf{T}}D^2\nu_0}{\nu_0^{\mathsf{T}}\nu_0}\right\}, \tag{2.18}$$

where $\mathcal{D}$ is the space of all $n\times n$ second derivative matrices and $\mathcal{V}$ is the set of eigenvectors of the ill-conditioned matrix A.

To better illustrate the effect this has on a nearly singular operator, take as an example the symmetric, positive-definite matrix

$$A=\begin{pmatrix}1 & 1\\ 1 & 1+\mu\end{pmatrix},\qquad\mu>0 \tag{2.19}$$

which has eigenvalues

$$\lambda_0^{\min}=\frac{1}{2}\left(-\sqrt{\mu^2+4}+\mu+2\right),\quad\lambda_0^{\max}=\frac{1}{2}\left(\sqrt{\mu^2+4}+\mu+2\right). \tag{2.20}$$

Clearly, A is ill-conditioned since $c(A)\to\infty$ as $\mu\to 0$ from above. Indeed, for $\mu=10^{-6}$, the condition number $c(A)\approx 4\times 10^6$. However, the asymptotic result (2.17) says simply choosing D to be the forward difference operator

$$D=\begin{pmatrix}1 & 0\\ -1 & 1\\ 0 & -1\end{pmatrix}, \tag{2.21}$$

and $\varepsilon=0.1$, the regularized condition number $c(A+\varepsilon D^2)\approx 23$; a noteworthy improvement. In fact, the true value of the condition number

$$c(A+\varepsilon D^2)=\frac{2+4\varepsilon+\mu+\sqrt{4-8\varepsilon+4\varepsilon^2+\mu^2}}{2+4\varepsilon+\mu-\sqrt{4-8\varepsilon+4\varepsilon^2+\mu^2}} \tag{2.22}$$

is even smaller at a value close to 7.

Choosing the operator D is problem-specific. However, we find that using second order centered-difference matrices D^2 is sufficient throughout this dissertation. This is the choice we make implicitly throughout our work and its effectiveness is demonstrated in Subsection 2.4.5.

2.4 The Hybrid Method

2.4.1 Overall Strategy

The previous computing paradigms have been extremely successful in many applications when the constraining dynamics are ODE [6, 13, 58]. However, in this dissertation, we are often faced with solving PDE constrained optimization problems. At the time of this writing, and to the best of the author's knowledge, there is no clear analogue of Ross's direct methods from Section 2.3.2 or Bellman's approach of Section 2.3.3. Of course, one could discretize the PDE constraints and control functions and pose the optimization problem as a large-scale NLP problem; however, theoretical results such as the covector mapping principle are sparse in this context. Moreover, this approach is somewhat difficult to implement and is computationally less efficient than other available methods which we will discuss shortly.

We note that since the admissible classes of controls $\mathcal{U}$ used throughout this dissertation are all locally convex, indirect methods are still theoretically and computationally viable because we avoid the paradoxical issues that may arise when using them [58]. Indirect methods are still faced with a major technical challenge; the non-convexity of either the objective functional or dynamic constraints. When an optimal control problem is non-convex, indirect methods alone are not guaranteed to converge to the global optima.

The method we use to solve optimal control problems throughout this dissertation is a combination of a direct method at the level of the reduced cost functional (2.6), which we call a semi-direct method in contrast with the fully

direct method of Subsection 2.3.2, followed by an indirect method. This approach is called the **hybrid method**. Hybrid methods, when used appropriately, can overcome non-convexity, yet still remain computationally efficient.

Combining direct and indirect methods in order to solve optimization problems has been done for quite some time. Before the work of Ross, et al. [59], the astrodynamics community routinely used direct methods based on Eulerian and Runge-Kutta discretizations (instead of collocation as in Section 2.3.2), solved the resulting optimization problem using NLP, and then used this solution as an initial guess for an indirect method [58]. In the quantum control literature, it seems Sørensen, et al. [63], were the first to use the type of hybrid method we use in this dissertation. They use a semi-direct method of due to Calarco, et al. [14,23], which uses a global search routine based on stochastic optimization to overcome non-convexity. Although it is well-known stochastic optimization methods can suffer from slow convergence near a local minimum [12], this is ameliorated by coupling the optimization to an indirect method in order to accelerate convergence.

2.4.2 The Chopped Random Basis Method

The semi-direct method of Calarco, et al. [14, 23], is called the **C**hopped **Ra**ndom **B**asis (CRAB) method. It relies on choosing controls from the span of an appropriately chosen finite set of basis functions so that the optimization is performed over a set of unknown coefficients. The choice of the basis is problem specific, but is always chosen so that controls remain in the appropriate admissible space. The choice of representation we always make throughout this dissertation is of the form

$$u_r(t) = \mathcal{P}(t; u_0, u_T, T) + \sum_{j=0}^{N-1} \varepsilon_j \varphi_j(t; T), \quad t \in [0, T], \tag{2.23}$$

where $\mathcal{P}$ is a fixed polynomial, $\varphi_j(t)$ is some basis function, and the coefficients ε_j are parameters to be optimized over. If the polynomial $\mathcal{P}$ and the basis functions

φ_j are chosen wisely enough, then control ansatz (2.23) reliably simplifies the optimal control problem given by objective (2.6).

The CRAB method can genuinely be viewed as a Galerkin type method. Recall that the intent behind any Galerkin method is to choose the number of basis functions N simultaneously large enough to define an accurate approximation, yet small enough so that the overall procedure remains computationally inexpensive. For the work in this dissertaion, we use at most 50 basis functions. In this way, the optimization problem is now a small-scale NLP problem and can be solved using industry standard techniques.

The technique we use to solve the resulting NLP problem is Differential Evolution (DE) [64]. DE is a stochastic optimization method used to search for candidate solutions to non-convex optimization problems. DE draws inspiration from evolutionary genetics and is thus part of a class of so-called genetic algorithms. DE searches the space of candidate solutions by initializing a population of agents within some appropriately chosen region of space. These agents are then mutated (see Algorithm 1) into a new generation that is necessarily no worse than the previous generation. As each iteration, or generation, evolves into the next, inferior agents inherit optimal traits from superior agents. After a sufficient number of evolutions, the best agent in the final generation is chosen as the candidate solution most likely to be globally optimal with respect to the objective functional (2.3). We provide a pseudocode of the general method in Algorithm 2. A more detailed discussion about DE and further implementation and benchmarking details can be found in the book by Storn, et al. [55].

Since so few assumptions need to be made about the objective functional, genetic algorithms as a whole are part of a wider class of optimization methods called metaheuristics. Although metaheuristics are useful in the context of non-convex optimization problems such as the one defined in Section 2.2, metaheuristic methods make no guarantees about the optimality of candidate solutions. For this

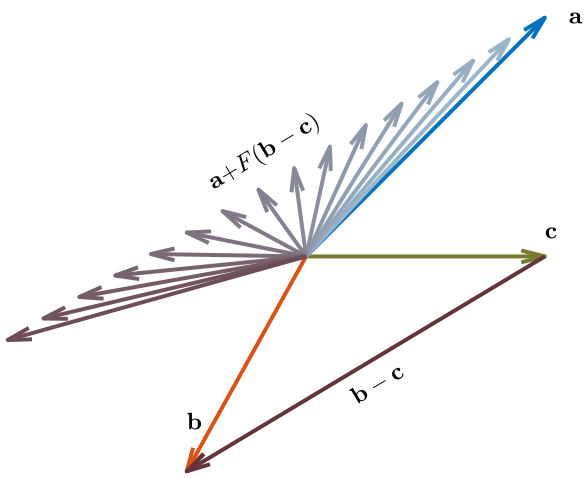

Figure 2.1 An example of vectors in $\mathbb{R}^2$ comprising the mutation function in Algorithm (1). The unlabeled vectors are the linear combinations $a + F(b - c)$, as F ranges from 0.2 to 1.6, which are used in the crossover defined in Algorithm (1) and used by Algorithm (2).

Algorithm 1: Differential Evolution Mutation

Result: A vector z mutated from agents in a given generation as required by differential evolution.

input: 4 distinct members a, b, c, d from the current generation of agents each with N components, the crossover ratio $R_C \in (0, 1)$, and weight $F \in (0, 2)$.

```
for j=1:N do
    Compute a random variable rand;
    if rand < R_C then
        y ← a[j] + F * (b[j] − c[j])
    else
        y ← d[j]
    end
    z[j] ← y;
end
```

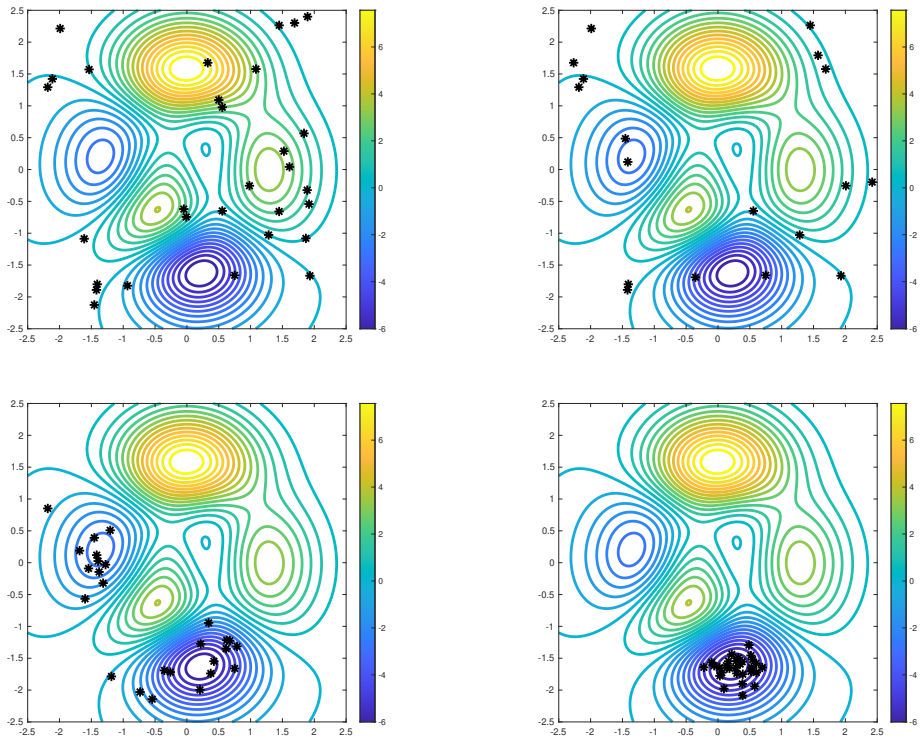

Figure 2.2 Different iterations of the DE algorithm applied to the peaks function (2.24). (a): The initial population. (b): The population of vectors after 1 iteration. (c): After 10 iterations. (d): After 20 iterations. The parameters used are $F = 0.6$ and $R_C = 0.9$, and the number of agent vectors N_{pop} is 20. Note that although all N_{pop} vectors are initialized on $\Omega = [-2.5, 2.5] \times [-2.5, 2.5]$, vectors are not explicitly constrained to be in Ω at each iteration. This accounts for the missing vectors in Panel (b).

Algorithm 2: Differential Evolution

Result: A vector likely to be globally optimal with respect to an objective J.

input: A maximum number of iterations `Nmax`, crossover ratio $R_C \in (0, 1)$ and weight $F \in (0, 2)$

while `counter` $<$ `Nmax` **do**
  Generate a population pop of N_{pop} vectors.
  for *i=1:*N_{pop} **do**
    `CurrentMember` $\leftarrow$ $\texttt{Pop}_i$*;*
    Choose three distinct vectors a_i, b_i, c_i different from the vector $\texttt{Pop}_i$;
    Mutate a_i, b_i, c_i, and the `CurrentMember` into the mutated vector z using the mutation parameters R_C, F and Algorithm 1;
    if $J(z) < J($`CurrentMember`$)$ **then**
      $\texttt{TemporaryPop}_i = z$;
    end
  end
  `Pop` $\leftarrow$ `TemporaryPop`*;*
  `counter` $\leftarrow$ `counter` $+ 1$*;*
end

reason, we use DE to search for candidate solutions and use these candidates in order to generate initial controls for in an indirect method.

In order to illustrate the generic behavior of DE, we show, in Figure 2.2, the effect of minimizing MATLAB's peaks function

$$f_{\text{peaks}}(x,y) = 3(1-x)^2 e^{-x^2-(y+1)^2} - \left(2x - 10x^3 - 10y^5\right) e^{-x^2-y^2} - \frac{1}{3} e^{-(x+1)^2-y^2} \tag{2.24}$$

using DE. We see that an initial, random population of vectors converges to the globally optimal regions of the function f_{peaks}. At an intermediate generation, the population vectors compete between two local minima, yet the population vectors eventually converge collectively on the more optimal of the two.

We further demonstrate how DE overcomes non-convexity using another test function. Consider the so-called Ackley function

$$f_{\text{Ackley}}(x,y) = -20e^{-0.2\sqrt{0.5(x^2+y^2)}} - e^{0.5(\cos 2\pi x + \cos 2\pi y)} + e + 20. \tag{2.25}$$

The Ackley function is highly non-convex. It has several local minima with a global minima at the origin. In Figure 2.3, we show the convergence of DE to the global minima in less than 40 iterations and with just $N_{\text{pop}} = 20$ agents, see Algorithm (2). We also find the parameters $R_C = 0.9$ and $F = 0.8$, required of Algorithm 2, work well enough for this test problem.

In the context of the CRAB method, the usage of DE requires uniformly drawing the coefficients ε_j from an appropriately constructed N dimensional hyperrectangle. The half-length of the j^{th} side of the hyperrectangle is chosen to be

$$l_j = \frac{u_T - u_0}{j^2}, \tag{2.26}$$

so that each ε_j is sampled from a uniform distribution on $[-l_j, l_j]$. We choose these coefficients to decay quadratically because the Fourier series of an absolutely continuous functions exhibits the same type of decay [70]. In this way, the search

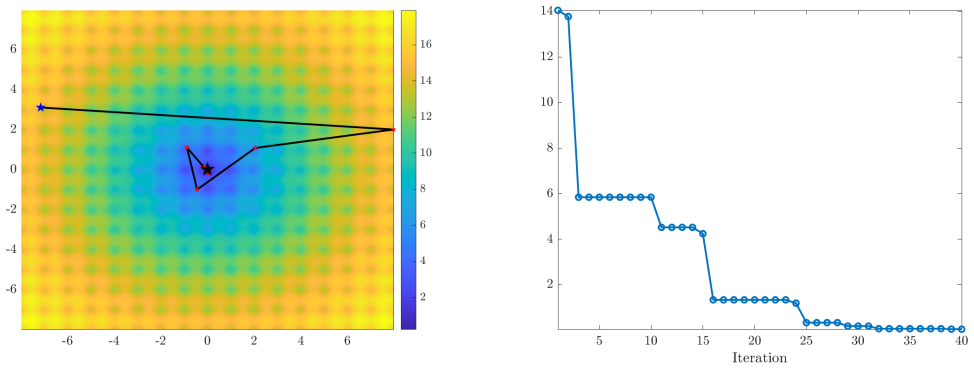

(a) (b)

Figure 2.3 Minimization of the Ackley Function (2.25) using the evolutionary Algorithms 1 and 2. Panel (a) shows the false-color plot of the Ackley function with the optimal member from each iteration of Algorithm 2 denoted by stars. Panel (b) shows the Ackley function evaluated at the optimal member of each iteration.

space of amplitudes ε_j is not severely restricted, yet the controls generated by the CRAB method remain technologically feasible throughout each generation.

2.4.3 Inexact Line Searches in $\mathbb{R}^n$

We use a line search strategy throughout this dissertation to numerically implement indirect methods. We introduce here the basic ideas of a line search in the simpler setting of unconstrained optimization problems over $\mathbb{R}^n$, i.e.,

$$\min_{x \in \mathbb{R}^n} J(x), \tag{2.27}$$

where the function J is assumed to be smooth. Line search approaches are iterative methods and when applied to minimization problems can be summarized by the following two steps: first, identify a descent direction p_k, and then compute a step size α_k which determines how far x_k should move along p_k at the k^{th} iteration. Put simply, line searches determine p_k and α_k such that

$$J(x_{k+1}) := J(x_k + \alpha_k p_k) < J(x_k). \tag{2.28}$$

After a Taylor expansion of Inequality (2.28), we see that

$$\langle p_k, \nabla J(x_k) \rangle_{\mathbb{R}^n} + \mathcal{O}(\alpha_k) < 0. \tag{2.29}$$

For this to hold uniformly in α_k, we should choose the descent direction p_k such that $\langle p_k, \nabla J(x_k) \rangle_{\mathbb{R}^n} < 0$. The most natural choice is $p_k = -\nabla J(x_k)$, in which case the line search is called a **gradient descent**. Choosing $p_k = -H(x_k)^{-1} \nabla J(x_k)$, where H is the Hessian of J and is assumed to be positive-definite, yields a damped Newton-Raphson method.

The task of determining α_k remains. An *exact* line search determines the solution of the subproblem

$$\min_{\alpha \in \mathbb{R}} J(x_k + \alpha p_k). \tag{2.30}$$

Often, computational resources are better allocated toward computing better search directions p_k and away from determining the stepsize α exactly. Therefore, it is wiser to approximate each α_k. A reasonable approach to choosing α_k is to start with some large value of α_k and to then continually reduce it until some criteria is met. Observe that

$$J(x_k + \alpha_k p_k) = J(x_k) + \langle \alpha_k, p_k \nabla J(x_k) \rangle_{\mathbb{R}^n} + \mathcal{O}\left(\alpha_k^2\right). \tag{2.31}$$

This suggests it is reasonable to decrease α_k until

$$J(x_k + \alpha_k p_k) \leq J(x_k) + \langle \alpha_k p_k \nabla J(x_k) \rangle_{\mathbb{R}^n}. \tag{2.32}$$

This *inexact* line search is called backtracking, and Inequality (2.32) is called the Armijo-Goldstein condition.

The line search strategies mentioned in this section are perhaps the most straightforward to implement. Also, since Newton's method requires a computation of $J's$ second derivatives, which is costly in a high-dimensional setting, we choose to use the method of gradient descent. Of course, there are many other options to choose from, see e.g. [12], but for the purposes of this dissertation,

the basic method of gradient descent with Armijo-Goldstein backtracking is shown to be adequate.

2.4.4 Gradient Descents in Homogeneous Sobolev Spaces

The last ingredient required of the hybrid method is an appropriate generalization of a gradient descent in $\mathbb{R}^n$. We use a method due to von Winckel and Borzi [75] because it automatically preserves the boundary conditions necessary for controls to stay within the admissible class $\mathcal{U}$ mentioned in the context of optimal control problem (2.3). This method is more recent and has been repeatedly used in the quantum control literature, see for example [34, 46]. We provide a brief outline here, but first discuss the means of arriving at the necessary conditions for optimality.

The problems considered throughout this dissertation are most easily modeled in Bolza form (2.3); however, determining the extrema of the objective functional (2.3) is more easily done for Lagrange problems where the relevant objective functional is expressed in the form

$$J = \int_0^T \mathcal{L}(\psi, u, \partial_t u) dt. \tag{2.33}$$

By assuming the terminal penalty function $\mathcal{G}$ is sufficiently smooth with respect to the parameter t, i.e., $\mathcal{G} \in C^1(0, T)$, we can convert the Bolza functional (2.3) to Lagrange form by using the fundamental theorem of calculus:

$$\mathcal{G}(\psi, u)\Big|_T = \mathcal{G}(\psi, u)\Big|_0 + \int_0^T \partial_t \mathcal{G} dt. \tag{2.34}$$

In addition, the input data (2.4) throughout this dissertation will involve initial conditions specified at the point $t = 0$. Therefore, we can ignore the first term on the right hand side of Equation (2.34) since the initial data is assumed fixed when we optimize over the control u. The resulting Lagrangian functional associated with the Bolza problem is then given by

$$\mathcal{L}(\psi, u, \partial_t u) = \partial_t \mathcal{G} + \mathcal{F}. \tag{2.35}$$

We note that this approach is not available if either $\mathcal{G} \notin C^1(0,T)$ or $\mathcal{G}$ is not known in closed-form. With the exception of the problem of Section 3.3, we will not encounter these issues and will mainly model optimization problems as Bolza problems and later convert to Lagrange problems by using this strategy.

The constraint (2.4) can be adjoined to the Lagrangian (2.35) by introducing a Lagrange multiplier p which exists in the space dual to $\mathcal{B}_\psi$; in the language of optimal control theory, p is called the costate of the system. This motivates the use of the Hamiltonian function

$$\mathcal{H} = \mathcal{L} + p^\dagger \mathcal{P} \tag{2.36}$$

where $\dagger$ denotes the adjoint operator, as is similarly used by Theorem (2.3.1).

The first-order optimality conditions for the Lagrange problem are determined by the appropriate Euler-Lagrange equations

$$\delta_\psi \mathcal{J} = 0, \tag{2.37a}$$

$$\delta_p \mathcal{J} = 0, \tag{2.37b}$$

$$\delta_u \mathcal{J} = 0, \tag{2.37c}$$

where $\delta_\bullet \mathcal{J}$ is understood as the functional derivative of J with respect to $\bullet$ [27]. The method of gradient descent, in this context, takes the form

$$u_{k+1} = u_k - \alpha_k \nabla_u \mathcal{H}\big|_{u=u_k}, \tag{2.38}$$

where the stepsize α is chosen using backtracking, and the Armijo-Goldstein condition for this problem reads

$$\mathcal{J}\left[u_k - \alpha \nabla_{u_k} \mathcal{H}\left(u_k\right)\right] < \mathcal{J}[u_k] - \frac{\alpha}{2} \|\nabla_{u_k} \mathcal{H}(u_k)\|^2_{L^2([0,T])}. \tag{2.39}$$

Until condition (2.39) is satisfied, the value of the stepsize α is decreased by some constant factor less than one. Since the gradient descent (2.38) depends on which function space $\nabla_u \mathcal{H}(u)$ is to be understood, we review some basic facts about calculus on infinite-dimensional (affine) spaces.

The Gateaux differential of a functional $\mathcal{J}$, evaluated at a point $u \in \mathcal{U}$ in the direction of a displacement vector $v \in C_c^\infty([0,T])$ is defined by

$$d_u\mathcal{J}[u;v] := \lim_{\varepsilon\to 0} \frac{\mathcal{J}[u+\varepsilon v] - \mathcal{J}[u]}{\varepsilon}, \tag{2.40}$$

and if this exists for all displacement vectors v in $\mathcal{U}$, the functional J is said to be Gateaux differentiable. Suppose we have the uniform bound $\sup_{u\in\mathcal{U}} |\mathcal{H}(u)| \leq M$ for some finite M. By a direct calculation, observe that

$$\begin{aligned} d_u\mathcal{J}[u;v] &= \lim_{\varepsilon\to 0} \frac{\mathcal{J}[u+\varepsilon v] - \mathcal{J}[u]}{\varepsilon} \\ &= \lim_{\varepsilon\to 0} \frac{1}{\varepsilon}\left(\int_0^T \mathcal{H}[u+\varepsilon v]dt - \int_0^T \mathcal{H}[u]dt\right) \\ &= \lim_{\varepsilon\to 0} \frac{1}{\varepsilon}\int_0^T\int_0^1 d_s\mathcal{H}[u+s\varepsilon v]dsdt \\ &= \lim_{\varepsilon\to 0} \int_0^T\int_0^1 \mathcal{H}'[u+s\varepsilon v]vdsdt \\ &= \int_0^T \nabla_u\mathcal{H}[u]vdt := \langle \delta_u\mathcal{J}, v\rangle_{L^2([0,T])}, \end{aligned} \tag{2.41}$$

making use of the bound on $\mathcal{H}$ in order to invoke the Lebesgue dominated convergence theorem in the last equality.

This shows the gradient of $\mathcal{H}$ with respect to the $L^2([0,T])$ inner product can be identified with the functional derivatives $\delta_u\mathcal{J}$ calculated and expressed through Equation (2.37c) , i.e., $\nabla_u\mathcal{H} = \delta_u\mathcal{J}$ in the space $L^2([0,T])$. However, if one were to perform a gradient descent on an initially admissible control u_k, the increment $\alpha_k\nabla_u\mathcal{H}\big|_{u=u_k}$ would fail to satisfy the boundary conditions and the updated function would not be in the admissible set $\mathcal{U}$. This problem is avoided by revisiting the choice of vector space from which the controls are drawn.

Note that since we expect Taylor's theorem to hold for all sufficiently regular functionals on Hilbert spaces, the Taylor series

$$J[u+\varepsilon v] = J[u] + \varepsilon d_u J[u,v] + \mathcal{O}(\varepsilon^2) = J[u] + \varepsilon\left\langle \nabla_u\mathcal{H}(u), v\right\rangle_X + \mathcal{O}(\varepsilon^2) \tag{2.42}$$

holds term-by-term for all spaces X. The method of von Winckel and Borzi relies on choosing X to be the homogeneous Sobolev space $\dot{H}_0^1([0,T])$, i.e., the vector

space of measurable functions, with zero trace on the boundary of [0,T] such that the norm $||\star||_{\dot{H}_0^1([0,T])}$ induced by the inner product

$$\langle \star, \star \rangle_{\dot{H}_0^1([0,T])} := \int_0^T (\partial_t \star)^\dagger (\partial_t \star)\, dt, \tag{2.43}$$

is finite. This implies, by equating the Gateaux differential with respect to $L^2([0,T])$ and with respect to $\dot{H}_0^1([0,T])$,

$$\begin{aligned} \langle \delta_u \mathcal{J}, v \rangle_{L^2([0,T])} = \langle \nabla_u \mathcal{H}(u), v \rangle_{\dot{H}_0^1([0,T])} &= \int_0^T \partial_t \nabla_u \mathcal{H} \partial_t v dt \\ &= -\int_0^T \partial_t^2 \nabla_u \mathcal{H} v dt = -\left\langle \partial_t^2 \nabla_u \mathcal{H}, v \right\rangle_{L^2([0,T])} \end{aligned} \tag{2.44}$$

where integration by parts is used once along with the boundary conditions of v. Since this holds for all displacements $v \in C_c^\infty([0,T])$, we conclude that in order to perform a gradient descent at the current control u, we must first solve the strong form of (2.44)

$$\partial_t^2 \nabla_u \mathcal{H} = -\delta_u \mathcal{J}, \quad \nabla_u \mathcal{H}(0) = \nabla_u \mathcal{H}(T) = 0 \tag{2.45}$$

in order to determine the admissible gradient of the objective with respect to the control. This is the projected gradient descent method of von Winckel and Borzi which is called the **Gra**dient Descent **P**ulse **E**ngineering (GRAPE) algorithm by the quantum control community [46, 63, 72] and is summarized by Algorithm (3).

Note that boundary value problem (2.45) yields a control gradient with homogeneous Dirichlet boundary conditions. This implies that the use of an iterative method which uses the control gradient in an update automatically preserves the boundary conditions of the control, as desired. In order to solve the two-point boundary values problems for the control gradients, we use spectral methods such as Chebyshev collocation [70].

We provide a slight extension of Algorithm (3) appropriate for problems where, in addition, Neumann boundary data is specified for the admissible class $\mathcal{U}$. We encounter a problem of this type in subsection 3.2. The idea is to use the inner product on $\dot{H}_0^2([0,T])$, so that we are instead tasked with solving an

Algorithm 3: Gradient Descent Method in $\dot{H}_0^p([0,T])$.

Result: Admissible control u which is locally optimal with respect to the objective functional

input: Initial admissible control u, the objective functional J, tolerance `tol`, maximum number of iterations `Nmax`, and reduction parameter $r \in (0,1)$

while `error` $>$ `tol` and `counter` $<$ `Nmax` **do**
  Solve the State equations (2.37b);
  Solve the Costate equations (2.37a);
  Compute $\nabla_u \mathcal{H}$ via Equation (2.47) with source term (2.37c);
  while Inequality (2.39) is false and $\alpha >$ `tol` **do**
    $\alpha \leftarrow r\alpha$;
  end
  if $\alpha <$ `tol` **then**
    break;
  else
    $u \leftarrow u - \alpha \nabla_u \mathcal{H}$;
    `error` $\leftarrow J[u] - J[u + \alpha \nabla_u \mathcal{H}]$;
    `counter` $\leftarrow$ `counter` $+ 1$;
  end
end

inhomogeneous biharmonic equation with homogeneous boundary data:

$$\partial_t^4 \nabla_u \mathcal{H} = \delta_u \mathcal{J}, \qquad \nabla_u \mathcal{H}(0) = \nabla_u \mathcal{H}(T) = \partial_t \nabla_u \mathcal{H}\big|_{t=0} = \partial_t \nabla_u \mathcal{H}\big|_{t=T} = 0. \quad (2.46)$$

Once again, it is easy to see the gradient $\nabla_u \mathcal{H}(u)$ preserves the appropriate boundary data when using a line search. In fact, it is also clear that the boundary value problem

$$\partial_t^{2p} \nabla_u \mathcal{H} = (-1)^p \delta_u \mathcal{J}, \qquad \partial_t^j \nabla_u \mathcal{H}\big|_{t=0} = \partial_t^j \nabla_u \mathcal{H}\big|_{t=T} = 0, \ j = 0, 1, \ldots, p-1, \quad (2.47)$$

generalizes the method of von Winckel and Borzi to the space $\dot{H}_0^p([0,T])$, for $p \in \mathbb{Z}^+$.

2.4.5 A Test of the Hybrid Method

We provide here an example of an exactly solvable optimal control problem which helps reveal some of the typical numerical difficulties we encounter and overcome using the techniques of this section. Consider the following Lagrange control problem

$$\min_{u \in \mathcal{U}} J = \min_{u \in \mathcal{U}} \int_0^\pi \left(x + \frac{1}{2}u^2 + \frac{\gamma}{2}\dot{u}^2 \right) dt, \quad (2.48)$$

subject to the forced harmonic oscillator

$$\dot{x} = p, \qquad x(0) = 0, \quad (2.49a)$$

$$\dot{p} = u - x, \qquad p(0) = 0, \quad (2.49b)$$

where $\mathcal{U} = \{u \in H^1([0,\pi]) : u(0) = u(\pi) = 0\}$.

Using the costate multipliers $\lambda(t)$ and $\mu(t)$, the equivalent unconstrained problem is given by

$$\begin{aligned} &\min_{u \in \mathcal{U}} \int_0^\pi \mathcal{L}\left(x, \dot{x}, p, \dot{p}, \lambda, \mu, u, \dot{u}\right) dt \\ =&\min_{u \in \mathcal{U}} \int_0^\pi \left(x + \frac{1}{2}u^2 + \frac{\gamma}{2}\dot{u}^2 + \lambda(\dot{x} - p) + \mu(\dot{p} + x - u) \right) dt. \end{aligned} \quad (2.50)$$

The Euler-Lagrange equations for this problem are given by Equations (2.37a)–(2.37c) (see also [78]) and reduce to

$$\frac{\delta\mathcal{L}}{\delta x} = \frac{\partial\mathcal{L}}{\partial x} - \frac{d}{dt}\frac{\partial\mathcal{L}}{\partial\dot{x}} = 1 - \dot{\lambda} + \mu = 0, \qquad \left.\frac{\partial\mathcal{L}}{\partial\dot{x}}\right|_{t=\pi} = \lambda(\pi) = 0, \tag{2.51a}$$

$$\frac{\delta\mathcal{L}}{\delta p} = \frac{\partial\mathcal{L}}{\partial p} - \frac{d}{dt}\frac{\partial\mathcal{L}}{\partial\dot{p}} = \lambda - \dot{\mu} = 0, \qquad \left.\frac{\partial\mathcal{L}}{\partial\dot{p}}\right|_{t=\pi} = \mu(\pi) = 0, \tag{2.51b}$$

$$\frac{\delta\mathcal{L}}{\delta\lambda} = \frac{\partial\mathcal{L}}{\partial\lambda} = \dot{x} - p = 0, \qquad x(0) = 0, \tag{2.51c}$$

$$\frac{\delta\mathcal{L}}{\delta\mu} = \frac{\partial\mathcal{L}}{\partial\mu} = \dot{p} + x - u = 0, \qquad p(0) = 0, \tag{2.51d}$$

$$\frac{\delta\mathcal{L}}{\delta u} = \frac{\partial\mathcal{L}}{\partial u} - \frac{d}{dt}\frac{\partial\mathcal{L}}{\partial\dot{u}} = u - \mu - \gamma\ddot{u} = 0, \qquad u(0) = u(\pi) = 0. \tag{2.51e}$$

Note that the costate terminal conditions are a result of an integration by parts again test functions $\varphi \in C_c^\infty([0,T))$, which do not necessarily vanish at $t = \pi$, in the construction of the adjoint operator present in the costate equations (2.51a) and (2.51b). More detail about the analogous derivation of these Euler-Lagrange equations in the context of PDE constraints is provided later on in this dissertation; for example in Appendix B.1.

Now, it's easy to see the following functions

$$\lambda_* = -\sin(t), \tag{2.52a}$$

$$\mu_* = -\cos(t) - 1 \tag{2.52b}$$

are the optimal costates. This implies, after using the method of variation of parameters, see e.g. [7], to solve Equation (2.51e), the optimal control is

$$u_* = \frac{\operatorname{csch}\left(\frac{\pi}{\sqrt{\gamma}}\right)\left((\gamma+2)\sinh\left(\frac{\pi-t}{\sqrt{\gamma}}\right) + \gamma\sinh\left(\frac{t}{\sqrt{\gamma}}\right)\right) - \cos(t) - \gamma - 1}{\gamma+1}. \tag{2.53}$$

Additionally, we solve for the optimal state x_* in a similar fashion which results in

$$\begin{aligned} x_* = &-\left(2(\gamma+1)^2\right)^{-1}\left(2\gamma(\gamma+2)\cosh\left(\frac{t}{\sqrt{\gamma}}\right) + (\gamma+1)(2\gamma + t\sin(t) + 2) + 2\cos(t)\right. \\ &\left. + \operatorname{csch}\left(\frac{\pi}{\sqrt{\gamma}}\right)\left((\gamma+2)\cosh\left(\frac{\pi}{\sqrt{\gamma}}\right) - \gamma\right)\left(\sqrt{\gamma}\sinh\left(\frac{t}{\sqrt{\gamma}}\right) - \sin(t)\right)\right), \end{aligned} \tag{2.54}$$

while the optimal objective J^* is found to be

$$J_* = \sqrt{\gamma}\tanh\left(\frac{\pi}{2\sqrt{\gamma}}\right)\left(\frac{\coth^2\left(\frac{\pi}{2\sqrt{\gamma}}\right)}{(\gamma+1)^2}+1\right) - \frac{\pi(2\gamma+3)}{4(\gamma+1)}. \tag{2.55}$$

We now turn towards numerically approximating the optimal control u_* using the methods detailed in Section 2.4. In order to ensure numerical validity in our program and maintain focus on the accuracy of the numerical optimization methods, we use MATLAB's built-in ordinary differential equation (ODE) solvers. We solve the state and costate equations (2.51a)–(2.51d) with MATLAB's `ODE45` solver. We also use `BVP4C` to solve Equation (2.45), required by Algorithm (3), with the inhomogeneity given by $\frac{\delta J}{\delta u}$ from Equation (2.51e).

We perform a test on the effectiveness of gradient descent using the GRAPE algorithm, Algorithm (3), without the aid of the CRAB method of Subsection 2.4.2. We use the admissible function $u_0 = t(t-\pi)$ as an initial control, set the Tikhonov parameter $\gamma = 1$, and use 1000 discretization points on the time interval $[0, \pi]$. We show the result of the computation in Figure 2.4.

We see the residual difference between the objective J evaluated at the final control computed through GRAPE and the optimal objective J_* is small. In fact, the efficiency

$$E(u_{\text{computed}}, u_*) = 1 - \left|\frac{J(u_{\text{computed}}) - J(u_*)}{J(u_*)}\right| \tag{2.56}$$

is about 0.9. However, the point-wise error between the computed functions u_{GRAPE} and $x(u_{\text{GRAPE}})$ against the exact functions u_* and x_*, which can be seen in Figure 2.4, remains relatively large. We could, of course, attempt to overcome these errors and refine the efficiency E further by guessing different admissible initial controls, but this is the reason behind using the CRAB method in the first place.

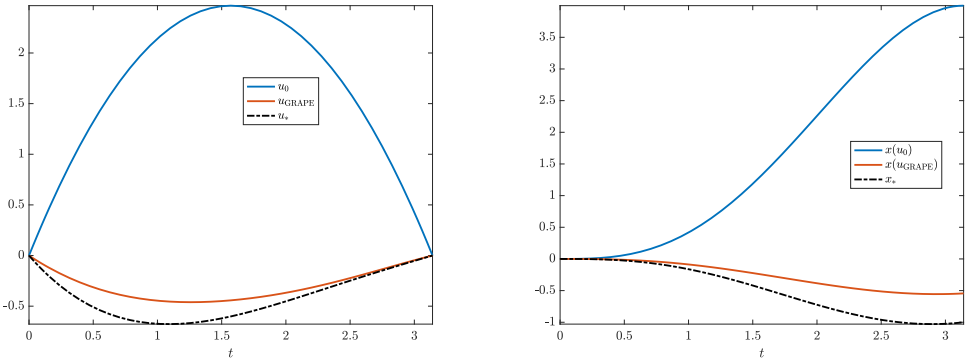

(a)

(b)

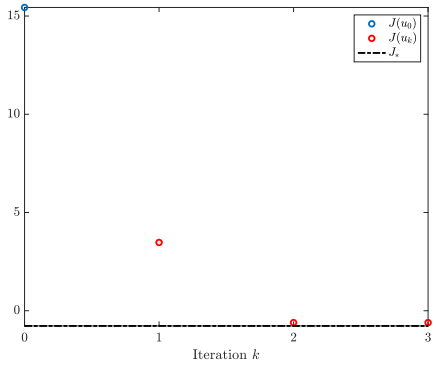

(c)

Figure 2.4 The result of using the GRAPE algorithm of Subsection 2.4.4. Panel (a) shows the initial, final computed, and exact controls u, while Panel (b) shows the initial, final computed, and exact states x. Panel (c) shows the local convergence of GRAPE.

We now show the result of using the hybrid method with initial controls found via the CRAB method. We use the 6 mode CRAB

$$u_r(t) = \sum_{j=1}^{6} \varepsilon_j \sin(jt), \tag{2.57}$$

and use differential evolution parameters $N_{\text{pop}} = 50$, $F = 0.8$, $C_R = 0.9$, and $N_{\max} = 30$. We input the resulting CRAB control, u_{CRAB}, into the GRAPE algorithm and find a final control which yields an efficiency of 0.994. In addition, the point-wise errors in the control and state have been significantly reduced. The results of the computation are shown in Figure 2.5.

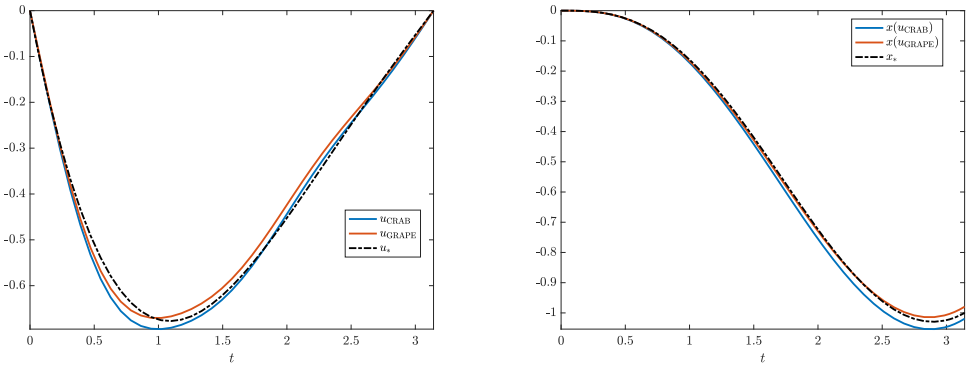

(a)

(b)

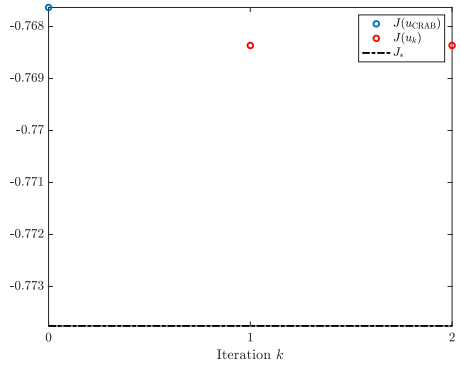

(c)

Figure 2.5 The result of first using the CRAB method of Subsection 2.4.2 and following up with GRAPE. The conventions are consistent with those in Figure 2.4.

We now investigate the role of the Tikhonov parameter γ. To this end, we use the same computational setting as that of Figure 2.5, but with $\gamma = 0.0058$. We see, in Figure 2.6, the optimal state x_* oscillates strangely in the vicinity of the boundary point $t = \pi$. This results in a significantly more computationally difficult control problem; a difficulty which is reflected through the failure of our numerics to resolve this oscillatory behavior. Increasing the number of CRAB functions, adjusting differential evolution parameters, and refining the temporal discretization do little to ameliorate this difficulty. Therefore, this suggests the optimal control problem (2.48) may be ill-posed in the absence of the Tikhonov regularization.

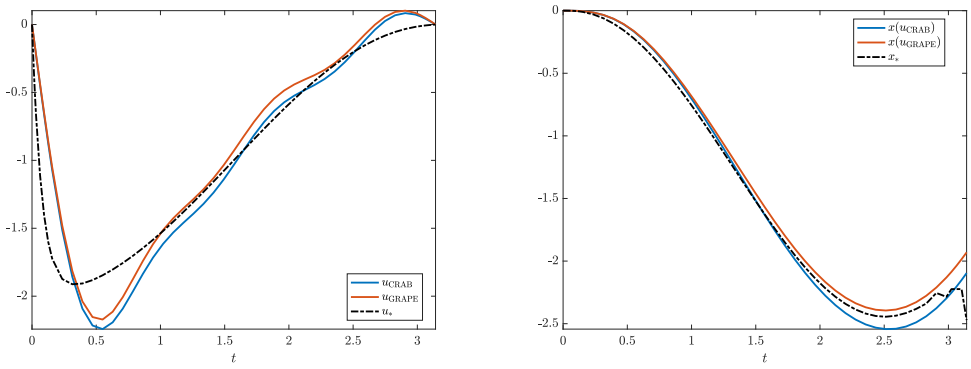

(a) (b)

Figure 2.6 An example of where the Tikhonov parameter γ is small. The conventions here are consistent with previous figures, yet we see the optimal state x_* is oscillatory near the right end of the boundary in Panel (b). This hints at the ill-posedness of optimal control problem (2.48) for small values of γ.

Upon reflection, the unregularized control problem is certainly ill-posed. The first term $\int_0^\pi x dt$, present in objective J, is unbounded from below. In addition, by fortune of the closed-form expressions (2.53) and (2.54), we can make more direct conclusions. For example, we see that u_* fails to remain a function in $H^1([0,\pi])$ as $\gamma \to 0$. We can also see the limit as $\gamma \to 0$ spells disaster for the optimal state x_*.

We show the onset of the ill-posed effects on the control u_* and state x_* in Figure 2.7. It is, perhaps, surprising to see how abruptly the effects of ill-posedness take place once γ crosses the numerically observed threshold of 0.01. We see that once $\gamma \approx 0.05$, x_* oscillates so wildly that even a discretization of 10^6 points cannot resolve the intermediate points of its oscillations.

From this toy problem, we learn the value of the Tikhonov regularization in optimal control. We also learn the merit of the hybrid optimization method as an effective tool for computationally solving optimal control problems. For these reasons, we will omit details about which values of γ are best or how effective different optimization strategies are. Instead, we will state which values of γ are sufficient in numerically solving the optimal control problems of each chapter in this dissertation. Additionally, the bulk of our optimal control results will be the

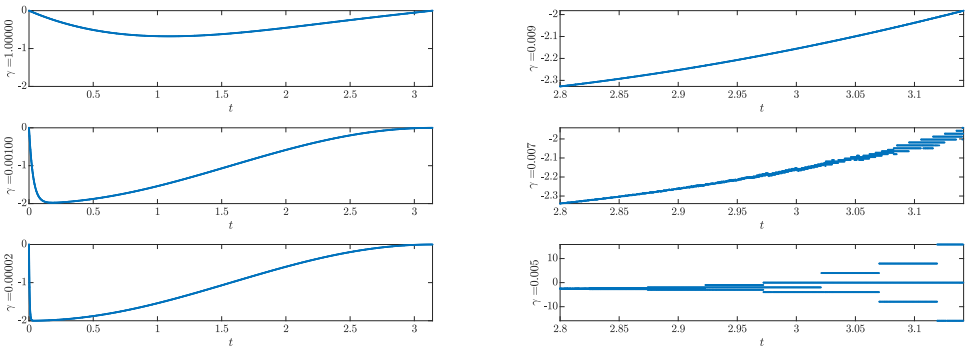

(a) (b)

Figure 2.7 The onset of ill-posedness as γ is reduced. Shown here are the optimal controls u_*, given by Equation (2.53) and shown in Panel (a), and the optimal states x_* in the vicinity of the boundary point $t = \pi$, given by Equation (2.54) and shown in Panel (b).

result of the hybrid optimization method and further details, such as the level of refinement from GRAPE on a CRAB control will mostly be neglected.

CHAPTER 3

OPTIMAL CONTROL OF HAMILTONIAN DYNAMICAL SYSTEMS IN BOSE-EINSTEIN CONDENSATES

3.1 Introdution

As discussed in Section 1.1, manipulating Bose-Einstein condensates (BEC) trapped by an external field is an important problem in nanoscale engineering. In this chapter, we consider the control of solutions to the Gross-Pitaevskii Equation (GPE)

$$i\partial_t \psi = -\frac{1}{2}\partial_x^2 \psi + V(x, u(t))\psi + |\psi|^2 \psi \tag{3.1}$$

as a model for BEC in a time dependent potential. Recall the objective is to compute a time-dependent function $u \in H^1(0,T)$, which controls the shape of the external trap $V(x,u(t))$, in order to drive the initial condition $\psi(x,0) = \psi_0(x) \in H^1(\mathbb{R})$ to some desired state. The precise control problem we consider will be stated in Section 3.4.

The novelty of this chapter lies in the model reduction we use to improve the computational complexity of the control problem. The reduced model is constructed via a Galerkin truncation and motivates the use of insights from Hamiltonian mechanics. In the following sections, we illustrate the method using two somewhat standard experiments from quantum control, [33, 46, 63, 72].

3.2 The Squeezing Problem

The first problem we address is that of squeezing and elongation discussed in Section 1.1 and shown in Figure 1.1. As a model problem, we consider the squeezing of a stationary wave packet centered about the origin and trapped in a quadratic potential, i.e. $V(x,u(t)) = \frac{1}{2}ux^2$ in Equation (3.1), with the endpoints of the control fixed as $u(0) = u_0 > 0,\ u(T) = u_T > u_0$.

We pursue the following Galerkin ansatz of the wavefunction ψ,

$$\psi(x,t) = \sum_{n=0}^{\infty} c_n(t)\varphi_n(x;u(t)), \tag{3.2}$$

where each of the $\varphi_n(x;u(t))$ are instantaneously normalized eigenfunctions of the equation

$$-\frac{1}{2}\partial_x^2\varphi_n + \frac{1}{2}ux^2\varphi_n = E_n\varphi_n, \tag{3.3}$$

i.e., the linear Schrödinger equation with a u-dependent quadratic potential. The eigenfunctions $\varphi_n(x;u)$ are well-known; they are Hermite functions and can be generated by means of the Rodrigues formula

$$\varphi_n(x;u) = (-1)^n \frac{\pi^{-1/4}}{\sqrt{2^n u^{n/4}\, n!}} u^{1/8} e^{\frac{u^{1/4}x^2}{2}} \partial_x^n e^{-u^{1/4}x^2}. \tag{3.4}$$

The first three are

$$\varphi_0(x;u) = \xi e^{-\frac{1}{2}\sqrt{u}x^2}, \tag{3.5a}$$

$$\varphi_1(x;u) = \sqrt{2}\xi u x e^{-\frac{1}{2}\sqrt{u}x^2}, \tag{3.5b}$$

$$\varphi_2(x;u) = \sqrt{2}\xi u \left(2\sqrt{u}x^2 - 1\right) e^{-\frac{1}{2}\sqrt{u}x^2}, \tag{3.5c}$$

where $\xi = \pi^{-1/4}u^{1/8}$. We truncate this expansion after the third term, and discard the single odd term involving $\varphi_1(x;u)$ because of the even symmetry engineered into the problem. For convenience, these first two even eigenstates and their time dependent coefficients will be relabeled as the $n = 0, 1$ states. We pursue a numerical justification for this truncation and discuss it later on in this section.

In order to derive the equations governing the time-dependent coefficients present in expansion (3.2), we substitute the expansion into the GPE (3.1) and project onto each mode using the standard $L^2(\mathbb{R})$ inner product. Letting $\dagger$ denote complex conjugation and overhead dots denote time derivatives, the resulting ODE

are

$$i\dot{c}_0 = \frac{\sqrt{u}c_0}{2} - \frac{i\dot{u}c_1}{4\sqrt{2}u} + \xi^2\left(\frac{|c_0|^2 c_0}{\sqrt{2}} + \frac{|c_1|^2 c_1}{32} + \frac{3|c_1|^2 c_0}{4\sqrt{2}} - \frac{|c_0|^2 c_1}{2} + \frac{3c_1^2 c_0^\dagger}{8\sqrt{2}} - \frac{c_0^2 c_1^\dagger}{4}\right), \quad (3.6)$$

and

$$i\dot{c}_1 = \frac{5\sqrt{u}c_1}{2} + \frac{i\dot{u}c_0}{4\sqrt{2}u} + \xi^2\left(\frac{41|c_1|^2 c_1}{64\sqrt{2}} - \frac{|c_0|^2 c_0}{4} + \frac{3|c_0|^2 c_1}{4\sqrt{2}} + \frac{|c_1|^2 c_0}{16} + \frac{c_1^2 c_0^\dagger}{32} + \frac{3c_0^2 c_1^\dagger}{8\sqrt{2}}\right). \quad (3.7)$$

These equations can be written in Hamiltonian form as

$$i\dot{c}_n = +\partial_{c_n^\dagger}\mathcal{H}, \qquad n = 0, 1, \quad (3.8a)$$

$$i\dot{c}_n^\dagger = -\partial_{c_n}\mathcal{H}, \qquad n = 0, 1, \quad (3.8b)$$

where the Hamiltonian $\mathcal{H}\left(c_0, c_0^\dagger, c_1, c_1^\dagger; u\right)$ is given by

$$\mathcal{H} = \frac{\sqrt{u}}{2}\left(|c_0|^2 + 5|c_1|^2\right) - \frac{\dot{u}}{2\sqrt{2}u}\Im\left\{c_0 c_1^\dagger\right\} + \xi^2\left(\frac{|c_0|^4}{2\sqrt{2}} + \frac{41|c_1|^4}{128\sqrt{2}} + \frac{3|c_0|^2|c_1|^2}{4\sqrt{2}} + \frac{3\Re\left\{c_0^2 c_1^{\dagger 2}\right\}}{8\sqrt{2}} - 2\Re\left\{c_0 c_1^\dagger\right\}\left(|c_0|^2 - \frac{|c_1|^2}{8}\right)\right). \quad (3.9)$$

It is easy to see the "discrete" mass $M_d(t) = |c_0(t)|^2 + |c_1(t)|^2$ is conserved by the dynamics of the Hamiltonian system (3.8). Moreover, since we assume the wavefunction ψ is normalized, $M_d(t)$ should be chosen to equal $M(t) = ||\psi(\cdot, t)||^2_{L^2(\mathbb{R})} = 1$. We further assume the initial state is at a local minimum of the Hamiltonian $\mathcal{H}$ with $\dot{u}$ set to 0 since, presumably, this state is stationary for some time before an intended transformation through the control $u(t)$ occurs in a physical setting.

In order to validate the use of the finite-dimensional dynamics (3.8) as a model problem, we perform the following numerical study. We fix the time domain

$t \in [0, T],\ T > 0$, and use a linear ramp of the form $u(t) = (u_T - u_0)\frac{t}{T} + u_0$. In particular, we choose $u_0 = 1,\ u_T = 100$, and $T = 2.5$. The comparisons we make involve the full numerical solution of the GPE (3.1), denoted ψ_{GPE}, projected onto the span of the two even modes, i.e.,

$$\psi_{\text{proj}}(x,t) = \sum_{n=0}^{1} \langle \psi_{\text{GPE}}(x,t), \varphi_n(x;u(t)) \rangle_{L_2(\mathbb{R})}\, \varphi_n(x;u(t)) := \sum_{n=0}^{1} c_n^{\text{proj}} \varphi_n(x;u(t)), \tag{3.10}$$

and the Galerkin representation (3.2) with $c_n(t)$ determined by a numerical solution of Equations (3.8).

We solve the GPE using a second order in time split-step Fourier method detailed in Appendix A.1. Consistent with previous assumptions, we use an initial condition of the form

$$\psi_0^*(x) = c_0^*(0)\varphi_0(x,u_0) + c_1^*(0)\varphi_1(x,u_0), \tag{3.11}$$

i.e., a superposition of the first two even states. The initial values $c_0^*(0)$ and $c_1^*(0)$ are chosen to minimize Hamiltonian (3.9) with $\dot{u}\big|_{t=0} = 0$. We solve the initial value problem governed by Hamilton's Equations (3.8), also with initial values $c_0^*(0), c_1^*(0)$, by using a fourth-order Runge-Kutta method. We provide visual comparisons of these numerical solutions in Figure 3.1.

We find the finite-dimensional dynamics, facilitated by the two even mode Galerkin expansion (3.2), works well to capture the qualitative behaviors of the GPE (3.1). First, we find good visual agreement in the so-called Rabi frequency, i.e. the frequency of energy transfer between the first two even modes. This agreement is exhibited by the similar periodic behavior between $c_n(t)$, which is determined by Equations (3.8), and $c_n^{\text{proj}}(t) = \langle \psi_{\text{GPE}}(\cdot,t), \varphi_n(\cdot;u(t)) \rangle_{L_2(\mathbb{R})}$, which is determined by a projection from the numerical solution of the GPE. Secondly, we find there is only about a 3% discrepancy between the discrete mass $M_d(t)$ and the projection of the full mass $M(t)$ onto the discrete modes by the end of the control process at $t = T$, i.e., $\frac{|M(T) - M_d^{\text{proj}}(T)|}{M(T)} \approx 0.03$ We see in Figure 3.1 this

discrepancy can be mainly attributed to the tails in the support of the distribution $|\psi_{\text{GPE}}|^2$.

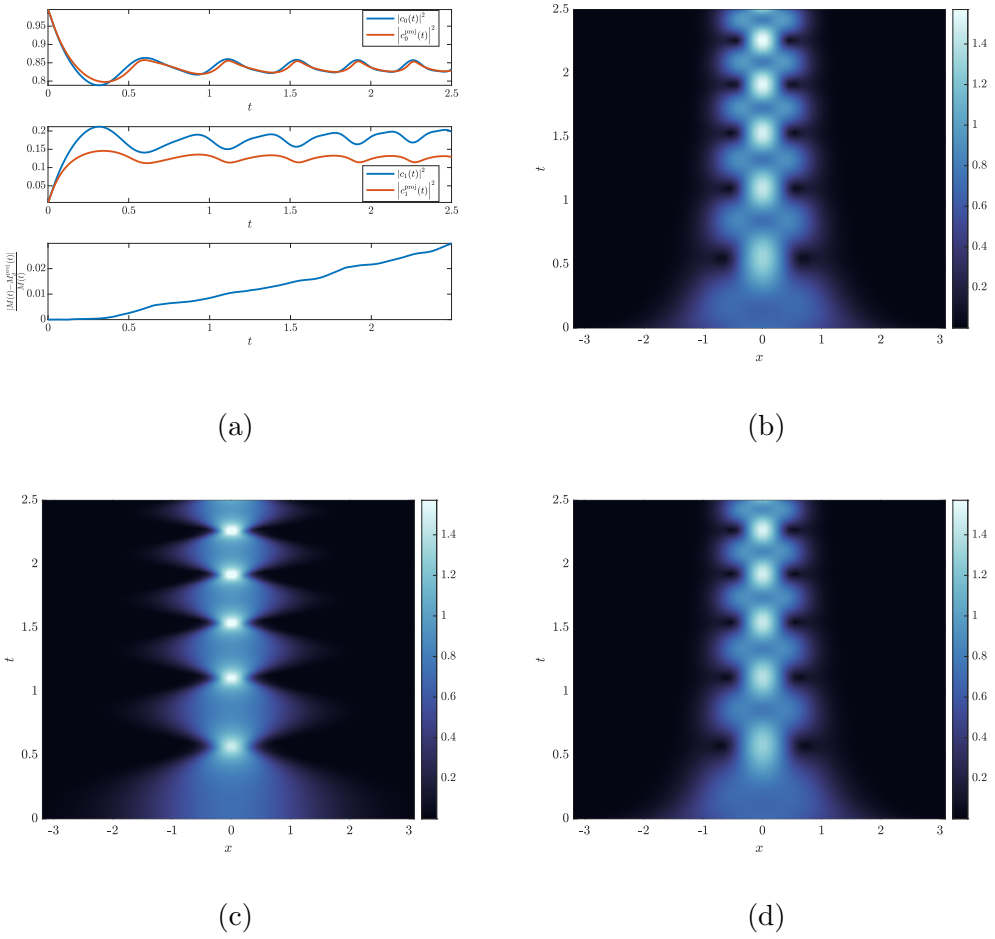

Figure 3.1 A numerical demonstration showing comparisons between a full numerical solution of Equation (3.1), shown in Panel (c) in absolute value squared, and the finite-dimensional approximation (3.2) with both initial conditions set by Equation (3.11). Panel (a) shows the numerical solution of Equations (3.6), (3.7), the projected coefficients c_n^{proj} defined in Equation (3.10), and the mass discrepancy between the mass $M(t)$ of the full numerical solution and the projected discrete mass $M_{\text{proj}}(t)$. Panel (b) shows the resulting ansatz (3.2) in absolute value squared with the numerical coefficients $c_n(t)$ from Panel (a). Panel (d) is the quantity $|\psi_{\text{proj}}(x,t)|^2$ given by Equation (3.10).

One of our primary goals in this chapter is to find an optimal control $u(t)$ which squeezes the width of an initial wavefunction, prepared mostly in the ground state, without exciting a significant long-term transfer of mass to higher states. Because of the strong numerical agreements demonstrated by Figure 3.1, we

conclude the Hamiltonian dynamical system (3.8) provides a sound model for purposes of constructing a potentially successful optimal control problem.

We now seek to further interpret the model dynamical system (3.8) for purposes of constructing an appropriate optimal control problem. To this end, we systematically pursue appropriate changes of variables which reduce the number of degrees of freedom. As currently stated, Hamiltonian (3.9) has two degrees of freedom and is time-dependent, or two and a half degrees of freedom for short. Through the use of canonical transformations, changes of variables which preserve the form of Hamilton's equations, we reduce the dimensionality of the squeezing problem to one and a half degrees of freedom. This allows the use of phase plane techniques which provide further insight into our problem.

We begin by converting to action-angle coordinates through the canonical transformation

$$c_0 = \sqrt{\rho_0} e^{-i\theta_0}, \quad c_1 = \sqrt{\rho_1} e^{-i\theta_1}. \tag{3.12}$$

Hamiltonian (3.9) then becomes

$$\begin{aligned}\mathcal{H} = &\frac{\sqrt{u}}{2}\left(\rho_0 + 5\rho_1\right) - \frac{\dot{u}}{4u}\sqrt{2\rho_0\rho_1}\sin\phi + \frac{3\xi^2}{8\sqrt{2}}\rho_0\rho_1\cos(2\phi) \\ &+ \frac{\sqrt{2}\xi^2}{256}\left(64\rho_0^2 + 96\rho_1\rho_0 + 41\rho_1^2 + \left(8\rho_1^{3/2}\sqrt{2\rho_0} - 56\rho_0^{3/2}\sqrt{2\rho_1}\right)\cos(\phi)\right),\end{aligned} \tag{3.13}$$

where $\phi = \theta_0 - \theta_1$. The advantage of using action-angle coordinates here is that the dependence of Hamiltonian (3.13) on a single phase ϕ becomes clear. By Noether's Theorem, this symmetry implies the freedom to eliminate either of the cyclic variables ρ_0 or ρ_1 through a conserved quantity; in this case through $M_d = \rho_0 + \rho_1 = 1$. An appropriate choice turns out to be $\rho_0 = 1 - J$ and $\rho_1 = J$ so that

$$\begin{aligned}\mathcal{H} = &\frac{\sqrt{u}}{2}\left(1 + 4J\right) + \frac{\xi^2}{128\sqrt{2}}\left(9J^2 - 32J + 64\right) - \frac{\dot{u}}{2\sqrt{2}u}\sqrt{(1-J)J}\sin(\phi) \\ &+ \frac{\xi^2}{16}\left(\sqrt{(1-J)J}(8 - 7J)\cos(\phi) + 3\sqrt{2}(1-J)J\cos(2\phi)\right)\end{aligned} \tag{3.14}$$

The problem has now been reduced to a one and a half degree of freedom system, as desired. We pursue two more canonical transformations in order to visualize the phase portrait in more familiar variables. The first maps back to polar coordinates via $\eta = \sqrt{J}e^{i\phi}$, where η is a complex-valued generalized coordinate. The second and final canonical transformation

$$\eta = \frac{q + ip}{\sqrt{2}}, \quad \eta^\dagger = \frac{q - ip}{\sqrt{2}}, \tag{3.15}$$

reminiscent of the familiar Dirac ladder operators, yields

$$\begin{aligned}\mathcal{H}(q,p,u) &= \frac{\xi^2}{512\sqrt{2}}\left(57p^4 - 160p^2 + 18p^2q^2 - 39q^4 + 32q^2 + 256\right) \\ &+ \sqrt{u}\left(q^2 + p^2 + \frac{1}{2}\right) + \frac{\xi^2}{64}\sqrt{2 - p^2 - q^2}\left(9q^3 - 16q + 9p^2q - \frac{8\sqrt{2\pi}\dot{u}}{u}p\right).\end{aligned} \tag{3.16}$$

We visualize the phase portrait associated with Hamiltonian (3.16) in the following way. We use the same numerical setting as that of Figure 3.1. We denote the initial and final Hamiltonians $\mathcal{H}(q,p,u_0)$, $\mathcal{H}(q,p,u_T)$ as $\mathcal{H}_0$, $\mathcal{H}_T$, respectively. We plot the contour lines of $\mathcal{H}_0, \mathcal{H}_T$ and their respective stable fixed points. This visual diagram, shown in Figure 3.2, further demonstrates the failure of a simple linear ramp control when squeezing the condensate in (q,p) coordinates. The phase portrait reveals how significant Rabi oscillations present in Figure 3.1 are simply the radial distance between the final state $(q(T), p(T))$ and the nearest stable fixed point (q^*, p^*) of Hamiltonian (3.16). This insight is the basis of the optimal control strategy of this chapter and is discussed further in Section 3.4.

We can characterize the persisting dynamics by using a standard linearization about the stable fixed point (q^*, p^*) [66]. Assume the control $u > 1$ is constant for $t \geq T$, and let $Q = q - q^*,\ P = p - p^*$. The resulting linear system is given by

$$\frac{d\mathbf{x}}{dt} := \frac{d}{dt}\begin{pmatrix} Q \\ P \end{pmatrix} = \begin{pmatrix} \partial_q\partial_p\mathcal{H} & \partial_p^2\mathcal{H} \\ -\partial_q^2\mathcal{H} & -\partial_p\partial_q\mathcal{H} \end{pmatrix}_{(q^*,p^*)} \begin{pmatrix} Q \\ P \end{pmatrix} := A\mathbf{x}. \tag{3.17}$$

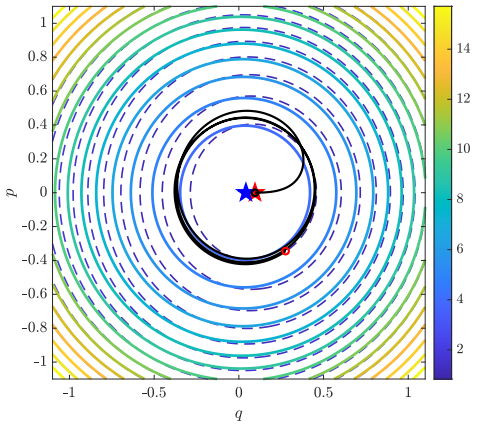

Figure 3.2 Phase portraits for $\mathcal{H}_0$, shown by dotted lines and a red star at its stable fixed point, and $\mathcal{H}_T$, shown by solid lines and a blue star at its stable fixed point. The black line represents the evolution of the coefficients (3.2) from Figure 3.1 after being mapped to (q, p) coordinates. The black circle is the corresponding intial state, and red circle the final state.

It is straightforward to show

$$\ddot{Q} + \omega_0^2(u)Q = 0, \tag{3.18}$$

where the natural frequency $\omega_0(u)$ is given by

$$\omega_0^2(u) = \det(A) = \left(\partial_p^2\mathcal{H}\partial_q^2\mathcal{H} - \partial_q\partial_p\mathcal{H}\partial_p\partial_q\mathcal{H}\right)\Big|_{(q^*,p^*)}. \tag{3.19}$$

This is given explicitly by

$$\omega_0^2(u) = 4u\left(1 - \frac{25}{512\pi}u^{-1/2}\right). \tag{3.20}$$

After further letting $\zeta^2 = \left(2\sqrt{u} - \frac{5\xi^2}{8\sqrt{2}}\right)\left(2\sqrt{u} + \frac{5\xi^2}{8\sqrt{2}}\right)^{-1}$, $\tilde{q} = q(T) - q^*$, and $\tilde{p} = p(T) - p^*$, we see that

$$q = q^* + \tilde{q}\cos(\omega_0 t) + \tilde{p}\zeta\sin(\omega_0 t) + \mathcal{O}(\tilde{q}^2, \tilde{p}^2, \tilde{q}\tilde{p}), \tag{3.21a}$$

$$p = p^* + \tilde{p}\cos(\omega_0 t) - \tilde{q}\zeta^{-1}\sin(\omega_0 t) + \mathcal{O}(\tilde{q}^2, \tilde{p}^2, \tilde{q}\tilde{p}), \tag{3.21b}$$

where $\mathcal{O}(\tilde{q}^2, \tilde{p}^2, \tilde{q}\tilde{p})$ is shorthand for terms quadratic in $\tilde{q}$ and $\tilde{p}$.

In conclusion, this section reveals that a successful optimal control strategy should drive the state of the condensate to the global minimum of the finite dimensional Hamiltonian (3.9). Furthermore, sub-optimality is almost entirely characterized by the amplitude of simple harmonic motion, given by Equations (3.21), about the fixed point (q^*, p^*).

3.3 The Splitting Problem

We refer to the problem of topologically changing the support of the condensate, mentioned in Section 1.1 and shown in Figure 1.2, as the "splitting" problem. In the case of one spatial dimension and "splitting" potential $V(x,u) = \frac{1}{2}x^2 + u\delta(x)$, the linear Schrödinger equation is exactly solvable for each value of u. For this reason, we use this potential and pursue the same strategy as in Section 3.2, i.e., track the evolution of the time-dependent coefficients in the appropriate eigenfunction expansion and use canonical transformations to gain a visual understanding of the resulting dynamics.

In order construct a Galerkin ansatz such as the one used in Section 3.2, we must solve the following eigenvalue problem

$$-\frac{1}{2}\partial_x^2\varphi_n + \frac{1}{2}x^2\varphi_n + u\delta(x)\varphi_n = E_n\varphi_n. \tag{3.22}$$

We provide brief details here on how to solve eigenvalue problem (3.22), but a more thorough computation and discussion is provided in work due to Viana-Gomes and Peres [73]. First, note that integrating (3.22) in a neighbourhood about the origin leads to a jump condition on the derivative:

$$\lim_{\varepsilon\to 0}\partial_x\varphi(x)\Big|_{-\varepsilon}^{+\varepsilon} = 2u\varphi\Big|_{x=0}. \tag{3.23}$$

Since the jump condition is automatically satisfied by any odd function in $C^1(\mathbb{R})$, the odd-parity states are still given by the Rodrigues formula (3.4) with the value

of u set to 1 there. Therefore, only the even-parity states feel the effect of the delta-function at the origin and must be modified.

Now, upon searching for solutions of the form $\varphi = e^{-x^2/2}w(x)$, letting $z = x^2$, and writing the energy in the more customary form $E = \nu + \frac{1}{2},\ \nu \in \mathbb{R}$, Equation (3.22) and condition (3.23) become

$$z\partial_z^2 w + \left(\frac{1}{2} - z\right)\partial_z w + \frac{\nu^2}{2}w = 0, \quad z > 0, \tag{3.24a}$$

$$\partial_z w\big|_{z=0} = uw\big|_{z=0}. \tag{3.24b}$$

Equation (3.24a) is called Kummer's equation and admits solutions of the form

$$w(z) = A_\nu U\left(-\frac{\nu}{2}, \frac{1}{2}, z\right) + B_\nu M\left(-\frac{\nu}{2}, \frac{1}{2}, z\right) \tag{3.25}$$

where the second term involves Kummer's function

$$M(a, b, z) = \sum_{n=0}^{\infty} \frac{a^{(n)} z^n}{b^{(n)} n!}, \tag{3.26}$$

with $(\cdot)^{(n)}$ denoting the rising factorial defined as

$$a^{(n)} := \prod_{k=0}^{n-1}(a + k), \tag{3.27}$$

and the first term involves Tricomi's confluent hypergeometric function

$$U(a, b, z) = \frac{\Gamma(1-b)}{\Gamma(a+1-b)}M(a, b, z) + \frac{\Gamma(b-1)}{\Gamma(a)}z^{(1-b)}M(a+1-b, 2-b, z), \tag{3.28}$$

with Γ denoting the standard gamma function. The coefficients A_ν and B_ν are simply appropriate normalization constants. Since it can be shown the function $M\left(-\frac{\nu}{2}, \frac{1}{2}, z\right)$ is not in $L^2(\mathbb{R})$, [73], we must set $B_\nu = 0$ in Equation (3.25).

The behavior of the Tricomi function $U(\cdot, \cdot, z)$ near the origin in the context of boundary condition (3.24b) leads to the following nonlinear equation

$$\nu - u\frac{\Gamma\left(1 - \frac{\nu}{2}\right)}{\Gamma\left(\frac{1}{2} - \frac{\nu}{2}\right)} = 0 \tag{3.29}$$

in ν. Briefly note that if the control satisfies u=0, then from Equation (3.29), ν=0, and we recover the even Hermite basis given by the Rodrigues formula (3.4), as we expect. In general, a numerical solution of Equation (3.29), demonstrated in [73], shows there is a countably infinite sequence of solutions $\{\nu_n\}$ each satisfying $\nu_{n+1} = \nu_n + 2$. Thus it suffices to solve Equation (3.29) on the interval [0,1], the interval containing the ground state value of ν, since this determines all other solutions. For $\nu \in [0, 1]$, the first two even eigenfunctions are given by

$$\varphi_j(x;\nu) = N_j(\nu)e^{-\frac{x^2}{2}}U\left(-\frac{\nu+2j}{2}, \frac{1}{2}, x^2\right) := N_j(\nu)e^{-\frac{x^2}{2}}U_j(x^2,\nu), \quad j = 0, 1, \tag{3.30}$$

where $N_j(\nu)$ are ν-dependent normalization constants given by

$$N_j^{-2}(\nu) = \int_{\mathbb{R}} e^{-x^2}U_j^2\left(x^2,\nu\right)dx, \quad j = 0, 1. \tag{3.31}$$

These eigenfunctions $\varphi_j(x;\nu)$ will serve as the set of basis functions in the ensuing Galerkin expansion.

Note that as $\nu \to 1$, the control u has infinite strength, i.e., $u \to \infty$, since the gamma function has a pole at the origin. In this case, the first two even eigenfunctions reduce to the simple form of "split" wavefunctions

$$\varphi_0(x;1) = 2^{\frac{1}{2}}\pi^{-\frac{1}{4}}\,|x|\,e^{-\frac{x^2}{2}}, \tag{3.32a}$$

$$\varphi_1(x;1) = 2\pi^{-\frac{1}{4}}3^{-\frac{1}{2}}\left(|x|^3 - \frac{3}{2}\,|x|\right)e^{-\frac{x^2}{2}}, \tag{3.32b}$$

which can be seen in Figure 3.3.

Proceeding with the same strategy from Section 3.2, we have after projecting onto each mode using the standard $L^2(\mathbb{R})$ inner product,

$$\begin{aligned} i\dot{c}_0 = \alpha_0 c_0 + \alpha_1 c_1 + u\left(\beta_0 c_0 + \beta_1 c_1\right) + \gamma_0|c_0|^2c_0 + \gamma_2|c_1|^2c_1 + 2\gamma_3|c_0|^2c_1 \\ + \gamma_3 c_0^2c_1^\dagger + 2\gamma_4 c_0^\dagger c_1^2 + \gamma_4|c_1|^2c_0 - i\Delta c_0, \end{aligned} \tag{3.33}$$

$$\begin{aligned} i\dot{c}_1 = \alpha_1 c_0 + \alpha_2 c_1 + u\left(\beta_1 c_0 + \beta_2 c_1\right) + \gamma_3|c_0|^2c_0 + \gamma_1|c_1|^2c_1 + 2\gamma_4 c_0^2c_1^\dagger \\ + \gamma_2 c_0^\dagger c_1^2 + \gamma_4|c_0|^2c_1 + 2\gamma_2|c_1|^2c_0 + i\Delta c_1, \end{aligned} \tag{3.34}$$

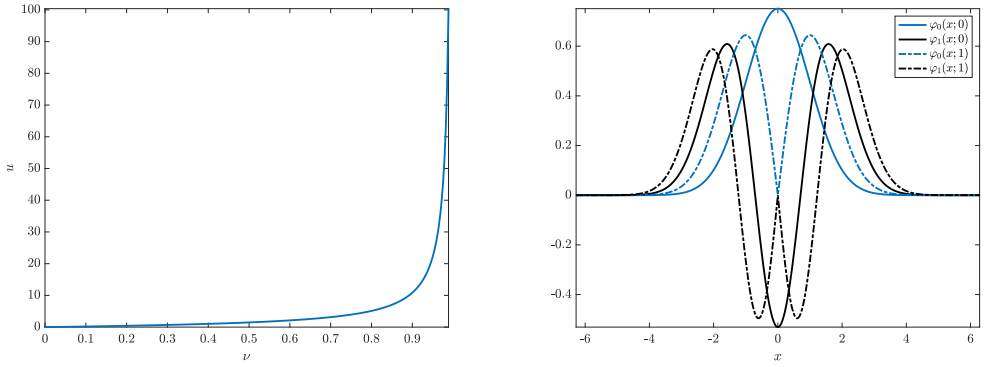

(a) (b)

Figure 3.3 Panel (a) shows $u(\nu)$ as determined by Equation (3.29). As can be seen, large values of u are needed to attain a value of ν close to 1. Panel (b) shows the first two excited even states in (3.30) for the values of $\nu = 0, 1$.

where

$$2\alpha_0 = \left\langle \varphi_0, x^2\varphi_0 - \partial_x^2\varphi_0 \right\rangle, \; 2\alpha_1 = \left\langle \varphi_0, x^2\varphi_1 - \partial_x^2\varphi_1 \right\rangle, \; 2\alpha_2 = \left\langle \varphi_1, x^2\varphi_1 - \partial_x^2\varphi_1 \right\rangle, \tag{3.35a}$$

$$\beta_0 = \langle \varphi_0, \delta(x)\varphi_0 \rangle, \; \beta_1 = \langle \varphi_0, \delta(x)\varphi_1 \rangle, \; \beta_2 = \langle \varphi_1, \delta(x)\varphi_1 \rangle, \tag{3.35b}$$

$$\gamma_0 = \left\langle \varphi_0^4 \right\rangle, \; \gamma_1 = \left\langle \varphi_1^4 \right\rangle, \; \gamma_2 = \left\langle \varphi_0, \varphi_1^3 \right\rangle, \; \gamma_3 = \left\langle \varphi_1, \varphi_0^3 \right\rangle, \; \gamma_4 = \left\langle \varphi_0^2, \varphi_1^2 \right\rangle, \tag{3.35c}$$

$$\Delta = \langle \varphi_0, \partial_t\varphi_1 \rangle = -\langle \partial_t\varphi_0, \varphi_1 \rangle. \tag{3.35d}$$

We make use of the relation

$$\partial_x U_j(x,\nu) = x\,(\nu + 2j)\,U\left(1 - j - \frac{\nu}{2}, \frac{3}{2}, x^2\right), \quad j = 0, 1, \tag{3.36}$$

in order to handle the spatial derivatives required of Equation (3.35a), after an integration by parts. Since the derivatives in relation (3.36) are only defined weakly at the origin, and smooth everywhere else, we make the computational choice of defining the derivatives at the origin as the average of the one-sided limiting values.

We calculate time derivatives of the Tricomi functions and normalization coefficients in Equation (3.30) numerically using finite centered differences. Meanwhile, we handle all quadratures required by inner products (3.35) numer-

ically using the trapezoidal rule. Since we also intend to solve the ODE (3.33) and (3.34) several times in an optimization routine, we store the values of the Tricomi functions (3.28) over space and time and call the values whenever we compute inner products (3.35).

We perform the same experiment as the one shown in Figure 3.1, but with $u(t) = 3t$ and $t \in [0, 10]$. In order to approximate the delta function in present in the splitting potential and in the Schrödinger equation (3.22), we use the heat kernel as a nascent delta function, i.e.,

$$\delta(x) = \lim_{a\to\infty} \frac{1}{2\pi a} e^{-\frac{x^2}{2a}}, \tag{3.37}$$

and use $a = 10$ as an approximation. Once again, we find good quantitative agreement between the GPE (3.1) and the model problem defined by the ODE (3.33), (3.34), and we show this in Figure 3.4.

Although many of the inner products required in constructing this finite dimensional problem cannot be computed in closed form, it is possible to show the Hamiltonian associated with ODE (3.33) and (3.34) for this problem is indeed given by

$$\begin{aligned}\mathcal{H} = &(\alpha_0 + u\beta_0)\left|c_0\right|^2 + (\alpha_2 + u\beta_2)\left|c_1\right|^2 + 2\left(\alpha_1 + \beta_1\right)\Re\left\{c_0 c_1^\dagger\right\} + \frac{1}{2}\gamma_0\left|c_0\right|^4 + \frac{1}{2}\gamma_1\left|c_1\right|^4 \\ &+ 2\left(\gamma_3\left|c_0\right|^2 + \gamma_2\left|c_1\right|^2\right)\Re\left\{c_0 c_1^\dagger\right\} + \gamma_4\left(\left|c_0\right|^2\left|c_1\right|^2 + 2\Re\left\{c_0^2 c_1^{\dagger 2}\right\}\right) + 2\Delta\Im\left\{c_0^\dagger c_1\right\}.\end{aligned} \tag{3.38}$$

Applying the same canonical transformations as in Section 3.2, we arrive at

$$\begin{aligned}\mathcal{H} = &\alpha_0 + \frac{\gamma_0}{2} + \sqrt{2 - p^2 - q^2}\left(q\left(\alpha_1 + \gamma_3 + \frac{1}{2}\left(\gamma_2 - \gamma_3\right)\left(p^2 + q^2\right) + \beta_1 u\right) + \Delta p\right) \\ &+ \frac{1}{2}(p^2 + q^2)\left(\alpha_2 - \alpha_0 - \gamma_0 + (\beta_2 - \beta_0)u\right) + \frac{\gamma_4}{2}\left(3q^2 - p^2\right) \\ &+ \frac{1}{8}\left(\gamma_0 + \gamma_1\right)\left(p^4 + q^4\right) + \frac{\gamma_4}{4}\left(p^4 - 3q^4\right) + \frac{1}{4}\left(\gamma_0 + \gamma_1 - 2\gamma_4\right)p^2 q^2 + \beta_0 u.\end{aligned} \tag{3.39}$$

We find the same leading order dynamics in the linearization about the stable fixed point (q^*, p^*), Equations (3.21), with natural frequency and amplitude parameters

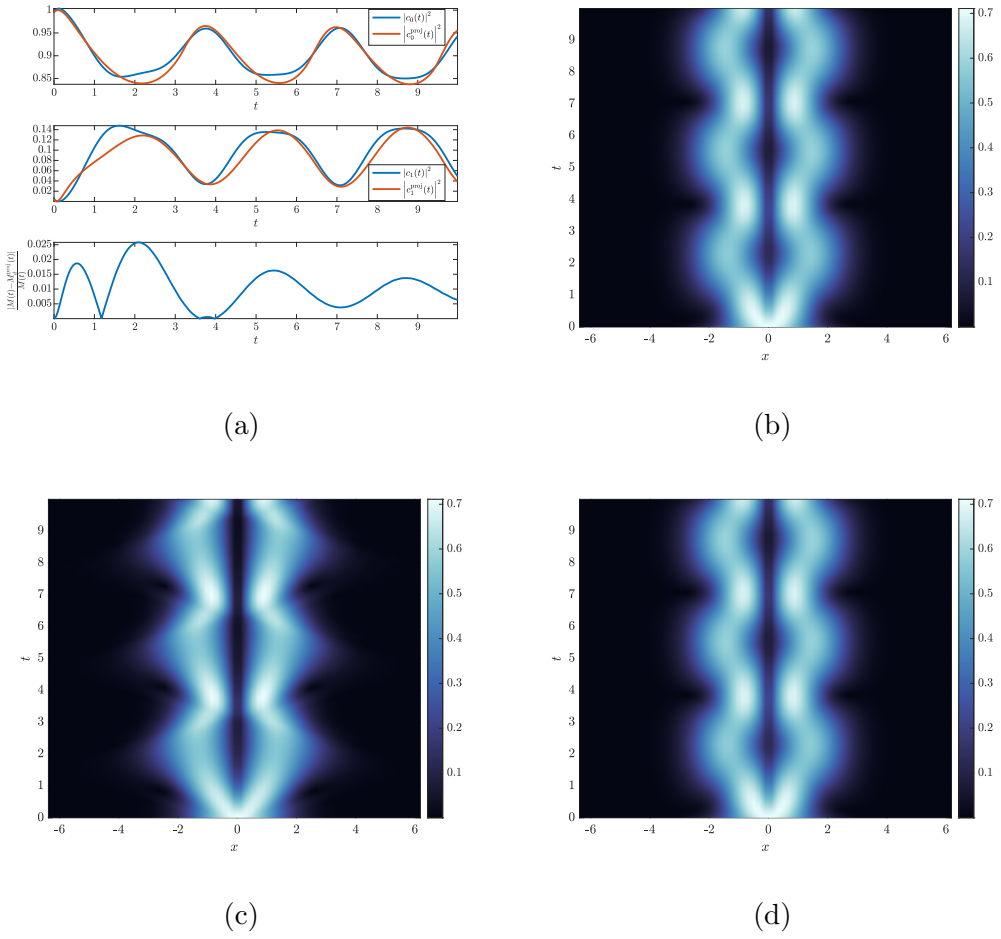

(a) (b) (c) (d)

Figure 3.4 A numerical demonstration showing comparisons between a full numerical solution of Equation (3.1), shown in Panel (c) in absolute value squared, and the finite-dimensional approximation (3.2), with eigenfunctions (3.22), and with both initial conditions set by the appropriately modified version of Equation (3.11). Panel (a) shows the numerical solution of Equations (3.33), (3.34), the projected coefficients c_n^{proj} defined in Equation (3.10), and the mass discrepancy between the mass $M(t)$ of the full numerical solution and the projected discrete mass $M_d^{\text{proj}}(t)$. Panel (b) shows the resulting ansatz (3.2) in absolute value squared with the numerical coefficients $c_n(t)$ from Panel (a). Panel (d) is the quantity $|\psi_{\text{proj}}(x,t)|^2$ given by Equation (3.10).

given by

$$\omega_0^2 = (\alpha_0 - \alpha_2 + \gamma_0 + \gamma_4 + \beta_0 u - \beta_2 u)(\alpha_0 - \alpha_2 + \gamma_0 - 3\gamma_4 + \beta_0 u - \beta_2 u), \quad (3.40)$$

$$\zeta^2 = (\alpha_0 - \alpha_2 + \gamma_0 + \gamma_4 + \beta_0 u - \beta_2 u)(\alpha_0 - \alpha_2 + \gamma_0 - 3\gamma_4 + \beta_0 u - \beta_2 u)^{-1}. \quad (3.41)$$

Clearly, the same physical interpretations and optimization strategies apply here as they did in Section 3.2.

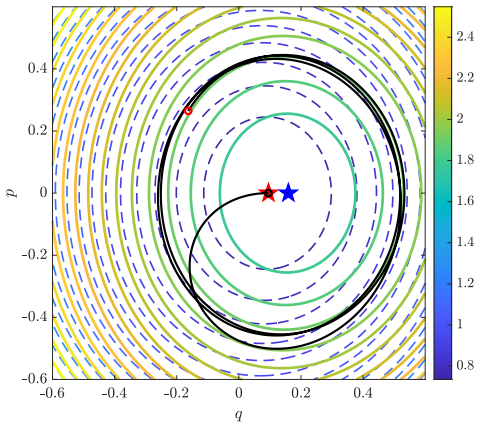

Figure 3.5 Phase portraits for $\mathcal{H}$ as in Equation (3.39) associated with the numerical experiment from Figure 3.4. The conventions are consistent with those in Figure 3.2.

3.4 Optimal Control Framework

We now state a general optimal control problem where the constraining dynamics are Hamiltonian. Soon after we will specialize to a particular form used to avoid significant Rabi oscillations motivated by Sections 3.2 and 3.3. To this end, let $u_0, u_T \in \mathbb{R}$ be boundary values for the control $u(t)$. The admissible class of controls $\mathcal{U}$ we consider is the set of all once weakly differentiable functions with prescribed boundary conditions, i.e. $\mathcal{U} = \{u \in H^1([0,T]) : u(0) = u_0, u(T) = u_T\}$. The general Hamiltonian optimal control problem we study is

$$\min_{u\in\mathcal{U}} J = \min_{u\in\mathcal{U}} \left\{ F(q,p,u,t)\Big|_{t=T} + \int_0^T G(q,p,u,\dot{u},t)\,dt \right\}, \quad (3.42)$$

subject to Hamilton's equations

$$\dot{q} = +\partial_p \mathcal{H}, \quad q(0) \in q_0 \in \mathbb{R}, \tag{3.43a}$$

$$\dot{p} = -\partial_q \mathcal{H}, \quad p(0) \in p_0 \in \mathbb{R}. \tag{3.43b}$$

Recall from Section 2.2 the first term in objective J is called the terminal cost and will be used to penalize deviations from some desired state of the Hamiltonian system. Also recall the second term is called the running cost and can serve different purposes in an optimal control problem, such as control regularization or penalizing resource expenditures.

Stating the necessary extremal conditions requires the use of Gateaux differentiation. To help compute the Gateaux derivatives, we convert the terminal cost into a running cost by using the fundamental theorem of calculus:

$$\begin{aligned} F\big|_{t=T} - F\big|_{t=0} &= \int_0^T \frac{dF}{dt} dt \\ &= \int_0^T \left(\frac{\partial F}{\partial q}\dot{q} + \frac{\partial F}{\partial p}\dot{p} + \frac{\partial F}{\partial u}\dot{u} + \frac{\partial F}{\partial t} \right) dt \\ &= \int_0^T \left(\frac{\partial F}{\partial q}\frac{\partial \mathcal{H}}{\partial p} - \frac{\partial F}{\partial p}\frac{\partial \mathcal{H}}{\partial q} + \frac{\partial F}{\partial u}\dot{u} + \frac{\partial F}{\partial t} \right) dt \\ &:= \int_0^T \left(\{F, H\} + \frac{\partial F}{\partial u}\dot{u} + \frac{\partial F}{\partial t} \right) dt, \end{aligned} \tag{3.44}$$

where the third line uses constraint (3.43) and the last line uses the definition of the Poisson brackets $\{\cdot, \cdot\}$. Recall the main advantage of expressing the terminal cost in (3.42) as the running cost (3.44) is in the ease of computing gradients with respect to the state and control variables.

By using the method of Lagrange multipliers, we express the Hamiltonian optimal control problem in unconstrained Lagrange form as

$$\min_{u \in \mathcal{U}} J = \min_{u \in \mathcal{U}} \left\{ \int_0^T \mathcal{L}\left(q, \dot{q}, p, \dot{p}, u, \dot{u}, \lambda, \mu\right) dt \right\}, \tag{3.45}$$

where

$$\mathcal{L} = \{F, H\} + \frac{\partial F}{\partial u}\dot{u} + \frac{\partial F}{\partial t} + G + \lambda^{\mathsf{T}} \left(\dot{q} - \frac{\partial \mathcal{H}}{\partial p} \right) + \mu^{\mathsf{T}} \left(\dot{p} + \frac{\partial \mathcal{H}}{\partial q} \right), \tag{3.46}$$

the notation $^{\mathsf{T}}$ denotes the matrix transpose, and where the cost $F\big|_{t=0}$ has been dropped since initial values for the state and control variables are specified, therefore fixed when taking derivatives. The necessary conditions for a locally extremal solution to Lagrange problem (3.45) are given by the Euler-Lagrange equations:

$$\frac{\delta \mathcal{L}}{\delta q} = \frac{\partial \mathcal{L}}{\partial q} - \frac{d}{dt}\frac{\partial \mathcal{L}}{\partial \dot{q}} = 0, \quad \left.\frac{\partial \mathcal{L}}{\partial \dot{q}}\right|_{t=T} = 0, \tag{3.47a}$$

$$\frac{\delta \mathcal{L}}{\delta p} = \frac{\partial \mathcal{L}}{\partial p} - \frac{d}{dt}\frac{\partial \mathcal{L}}{\partial \dot{p}} = 0, \quad \left.\frac{\partial \mathcal{L}}{\partial \dot{p}}\right|_{t=T} = 0, \tag{3.47b}$$

$$\frac{\delta \mathcal{L}}{\delta u} = \frac{\partial \mathcal{L}}{\partial u} - \frac{d}{dt}\frac{\partial \mathcal{L}}{\partial \dot{u}} = 0, \tag{3.47c}$$

$$\frac{\delta \mathcal{L}}{\delta \lambda} = \frac{\partial \mathcal{L}}{\partial \lambda} = 0, \tag{3.47d}$$

$$\frac{\delta \mathcal{L}}{\delta \mu} = \frac{\partial \mathcal{L}}{\partial \mu} = 0. \tag{3.47e}$$

In deriving these Euler-Lagrange equations, the terminal conditions are the results of an integration by parts against arbitrary functions $\phi \in C_c^\infty([0,T))$, i.e., the space of infinitely differentiable functions with compact support on the interval $[0,T)$, where the the interval of compact support has a closed/open bracket due to the problem's specified/unspecified initial/terminal conditions, respectively.

Motivated by intuition gained by the phase portraits in Sections 3.2 and 3.3, we specialize optimal control problem (3.45) to the case for when $F = \mathcal{H}$. This also has the advantage of simplifying the Euler-Lagrange equations since $\{\mathcal{H}, \mathcal{H}\} = 0$. Furthermore, we choose the simple Tikhonov regularization $G = \frac{\gamma}{2}\dot{u}^2$ as we did previously in Subsection 2.4.5. In this case, the necessary optimality conditions

reduce to

$$\frac{\delta\mathcal{L}}{\delta q} = \mu\frac{\partial^2\mathcal{H}}{\partial q^2} - \lambda\frac{\partial^2\mathcal{H}}{\partial q\partial p} + \dot{u}\frac{\partial^2\mathcal{H}}{\partial q\partial u} - \dot{\lambda} = 0, \qquad \left.\frac{\partial\mathcal{L}}{\partial\dot{q}}\right|_{t=T} = \lambda(T) = 0, \tag{3.48a}$$

$$\frac{\delta\mathcal{L}}{\delta p} = \mu\frac{\partial^2\mathcal{H}}{\partial p\partial q} - \lambda\frac{\partial^2\mathcal{H}}{\partial p^2} + \dot{u}\frac{\partial^2\mathcal{H}}{\partial p\partial u} - \dot{\mu} = 0, \qquad \left.\frac{\partial\mathcal{L}}{\partial\dot{p}}\right|_{t=T} = \mu(T) = 0, \tag{3.48b}$$

$$\frac{\delta\mathcal{L}}{\delta u} = \mu\frac{\partial^2\mathcal{H}}{\partial u\partial q} - \lambda\frac{\partial^2\mathcal{H}}{\partial u\partial p} + \dot{u}\frac{\partial^2\mathcal{H}}{\partial u^2} - \frac{d}{dt}\frac{\partial\mathcal{H}}{\partial u} - \gamma\ddot{u} = 0, \qquad u(0) = u_0,\ u(T) = u_T, \tag{3.48c}$$

$$\frac{\delta\mathcal{L}}{\delta\lambda} = \dot{q} - \frac{\partial\mathcal{H}}{\partial p} = 0, \tag{3.48d}$$

$$\frac{\delta\mathcal{L}}{\delta\mu} = \dot{p} + \frac{\partial\mathcal{H}}{\partial q} = 0. \tag{3.48e}$$

To summarize the equations concisely,

$$\frac{d}{dt}\begin{pmatrix} q \\ p \\ \lambda \\ \mu \\ \gamma\dot{u} \end{pmatrix} = A\begin{pmatrix} \frac{\partial\mathcal{H}}{\partial q} \\ \frac{\partial\mathcal{H}}{\partial p} \\ \lambda \\ \mu \\ \dot{u} \end{pmatrix} - \begin{pmatrix} 0 \\ 0 \\ 0 \\ 0 \\ \frac{d}{dt}\frac{\partial\mathcal{H}}{\partial u} \end{pmatrix}, \quad \begin{pmatrix} q(0) \\ p(0) \\ u(0) \end{pmatrix} = \begin{pmatrix} q_0 \\ p_0 \\ u_0 \end{pmatrix}, \begin{pmatrix} \lambda(T) \\ \mu(T) \\ u(T) \end{pmatrix} = \begin{pmatrix} 0 \\ 0 \\ u_T \end{pmatrix}, \tag{3.49}$$

where

$$A = \begin{pmatrix} 0 & 1 & 0 & 0 & 0 \\ -1 & 0 & 0 & 0 & 0 \\ 0 & 0 & \frac{\partial^2\mathcal{H}}{\partial q^2} & -\frac{\partial^2\mathcal{H}}{\partial q\partial p} & \frac{\partial^2\mathcal{H}}{\partial q\partial u} \\ 0 & 0 & \frac{\partial^2\mathcal{H}}{\partial p\partial q} & -\frac{\partial^2\mathcal{H}}{\partial p^2} & \frac{\partial^2\mathcal{H}}{\partial p\partial u} \\ 0 & 0 & \frac{\partial^2\mathcal{H}}{\partial u\partial q} & -\frac{\partial^2\mathcal{H}}{\partial u\partial p} & \frac{\partial^2\mathcal{H}}{\partial u^2} \end{pmatrix} = \left(\begin{array}{c|c} \mathcal{J} & \mathbf{0}_{2\times 3} \\ \hline \mathbf{0}_{3\times 2} & D\left(\frac{\partial\mathcal{H}}{\partial q}, -\frac{\partial\mathcal{H}}{\partial p}, \frac{\partial\mathcal{H}}{\partial u}\right) \end{array}\right), \tag{3.50}$$

with $\mathcal{J}$ denoting the corresponding skew-symmetric matrix and D denoting the Jacobian matrix.

Recall Equations (3.48a) and (3.48b) are called the costate equations and are solved backward in time from their respective terminal conditions. Equation

(3.48c), along with the prescribed boundary conditions on the control, is a two-point boundary value problem for u. Since solving these equations in closed form is often not possible, we resort to the numerical methods discussed in Chapter 2 in order to solve the optimal control problem (3.42).

3.5 Numerical Results

We use the hybrid optimization method of Section 2.4 in order to numerically solve optimal control problem (3.42) for the model problems of Sections 3.2 and 3.3. We choose the time horizon consistent with the numerical experiments shown in Figures 3.1 and 3.4, i.e., $T = 2.5$ for the squeezing problem and $T = 10$ for the splitting problem. For both problems, we use 15 sine modes and an admissible linear ramp for the CRAB algorithm, i.e., the CRAB we use is

$$u_r(t) = (u_T - u_0)\frac{t}{T} + u_0 + \sum_{j=1}^{15} \varepsilon_j \sin\left(\frac{j\pi t}{T}\right) \tag{3.51}$$

In order to determine the unknown coefficients ε_j using differential evolution, we use parameters of $F = 0.8$, $R_C = 0.9$, $N_P = 40$, and $N_{\max} = 30$ required by Algorithms (1) and (2). We also set Tikhonov parameter $\gamma = 10^{-4}$, and find this to be sufficient for avoiding the onset of possible ill-posedness such as that shown in Figure 2.7.

It is important to note that the value of $\mathcal{H}_T$ for both model problems depends on the quantity $\dot{u}\big|_{t=T}$. Since the Hamiltonian is abruptly changed at $t = T$ to one with constant control, the minimum value of the Hamiltonian we are truly interested in is independent of any terms which depend on the derivative of the control. For this reason, we choose to minimize the Hamiltonian with $\dot{u}$ set to 0 at $t = T$ which motivates the use of GRAPE in $\dot{H}_0^2([0, T])$. Recall that computing gradients using Equation (2.46) importantly preserves both Dirchlet and Neumann data. This allows us to use a line search for controls which perform more optimally with the respect to the modified Hamiltonian $\mathcal{H}_T\big|_{\dot{u}=0}$.

For both the squeezing and splitting problems, we show the Galerkin coefficients, computed controls, and resulting numerical solution of the GPE with optimal and linear controls up until some time T. We show the persisting dynamics afterwards with constant control $u(T)$, and the associated phase diagram in the appropriate coordinates. The result of squeezing is in Figure 3.8. Splitting is shown in Figure 3.10.

The total time for computing the optimal control policies is on the order of minutes. The squeezing problem takes an average of about half a minute while the splitting problem takes an average of a more honest 3-5 minutes on an average workstation. The splitting problem takes more time since for each evaluation of the objective in Equation (3.42) because we must compute the inner products of Equations (3.35).

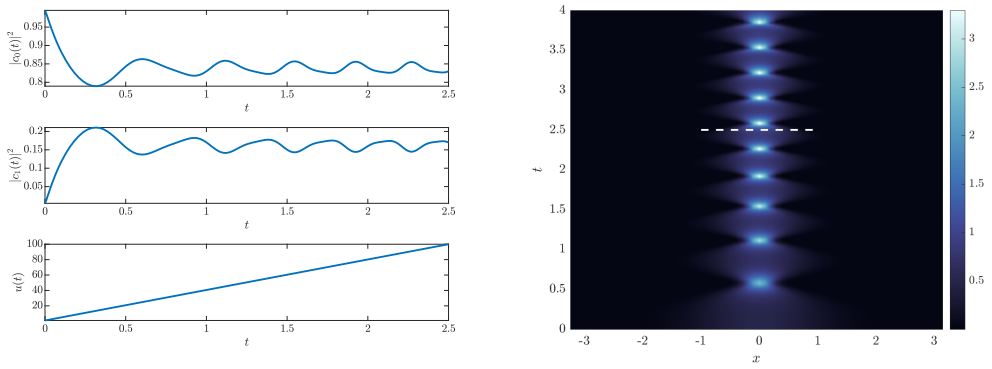

(a) (b)

Figure 3.6 The result of the squeezing experiment using a linear ramp. The conventions used here are consistent with Figure 3.1

Lastly, we are interested in a quantitative measure for comparing our results to solutions of the corresponding GPE. To this end, we use the infidelity term from the Hohenester objective (1.3) between the computed solution of the GPE and the corresponding ground state eigenfunction $\varphi_0(x)$ at time $t = T$. More precisely, we use

$$J^{\text{infidelity}}(t) = \frac{1}{2}\left(1 - |\langle \varphi_0(x,T), \psi(x,t)\rangle|^2_{L^2(\mathbb{R}^n)}\right). \tag{3.52}$$

We start by showing the result of using a linear ramp in Figure 3.6 for purpose of comparison. This figure is similar to Figure 3.1, yet the persisting dynamics, i.e., the dynamics after the time T, are better shown.

Then, in Figure 3.7, we show the result of using GRAPE to compute a local minimum downhill from the linear ramp in Figure 3.6. There, we show the locally optimal control, locally optimal state dynamics, the corresponding numerical solution of the GPE (3.1), the corresponding phase portrait for the reduced dynamics, and convergence of GRAPE.

We see that after using GRAPE, the bulk of the condensate's support is more concentrated at the origin. Indeed, this corresponds with the value of the Hamiltonian $\mathcal{H}_T$ having been reduced by nearly a factor of 2. Furthermore, since we know the numerical value of $\mathcal{H}_T$, we can use the efficiency E, i.e., Equation (2.56). We find that the efficiency is about 0.941. However, this result is only locally optimal, as to be expected, and so we must pursue controls which are globally optimal.

Turning to the complete hybrid method, we find results which are more optimal by all accounts. We show, in Figure 3.8, the result of using CRAB followed by GRAPE in $\dot{H}_0^2([0,T])$. The efficiency E is now about 0.972. We also see the infidelity $J^{\text{infidelity}}$ has been reduced by an order of magnitude with respect to the infidelity of the linearly controlled condensate.

We show similar results for the splitting problem of Section 3.3. Again, all conventions used here are similar to those of Figure 3.4. We first show the result of splitting using a linear ramp in Figure 3.9. We then show the result of CRAB in Figure 3.10. Recall, the absence of GRAPE is due to difficulties in differentiating the Hamiltonian (3.38) with respect to the control u. Despite this difficulty, we still find a control with an efficiency of about 0.962 and a condensate with significantly reduced infidelities.

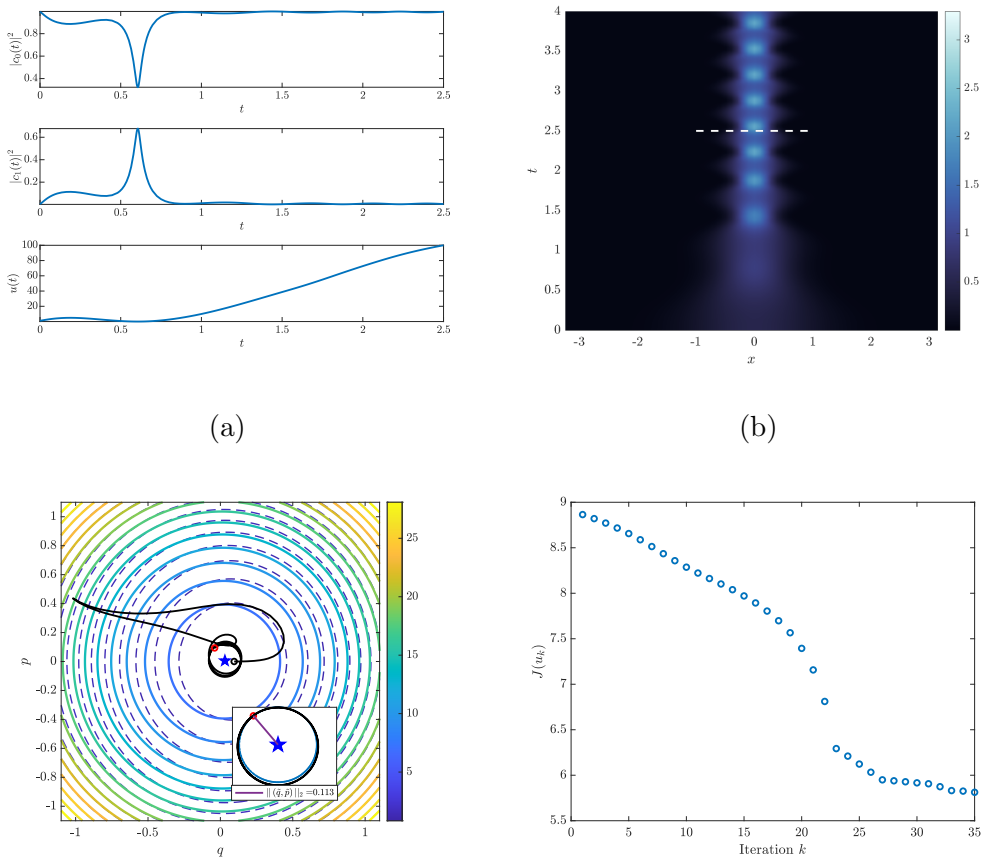

Figure 3.7 The result of using the GRAPE algorithm of Subsection 2.4.4 with the linear ramp from Figure 3.6 as an initial control. Conventions used here are similar to conventions used in Figures 3.1 and 3.2. Panel (a) shows the Galerkin coefficients which satisfy Equations (3.2) with optimal control u. Panel (b) is the numerical solution of the GPE with the optimal control u from Panel (a) up until the dotted black line. The persisting dynamics are computed with constant control $u(T)$. Panel (c) shows the resulting phase portrait with the inset showing the persistent dynamics. The black trajectory in the inset is the numerical solution of Equations (3.48d) and (3.48e) where the Hamiltonian is given by Equation (3.16). The nearby blue trajectory is given by Equations (3.21) which are the result of a linearization about the stable fixed point denoted by the central blue star. Panel (d) shows the convergence of GRAPE.

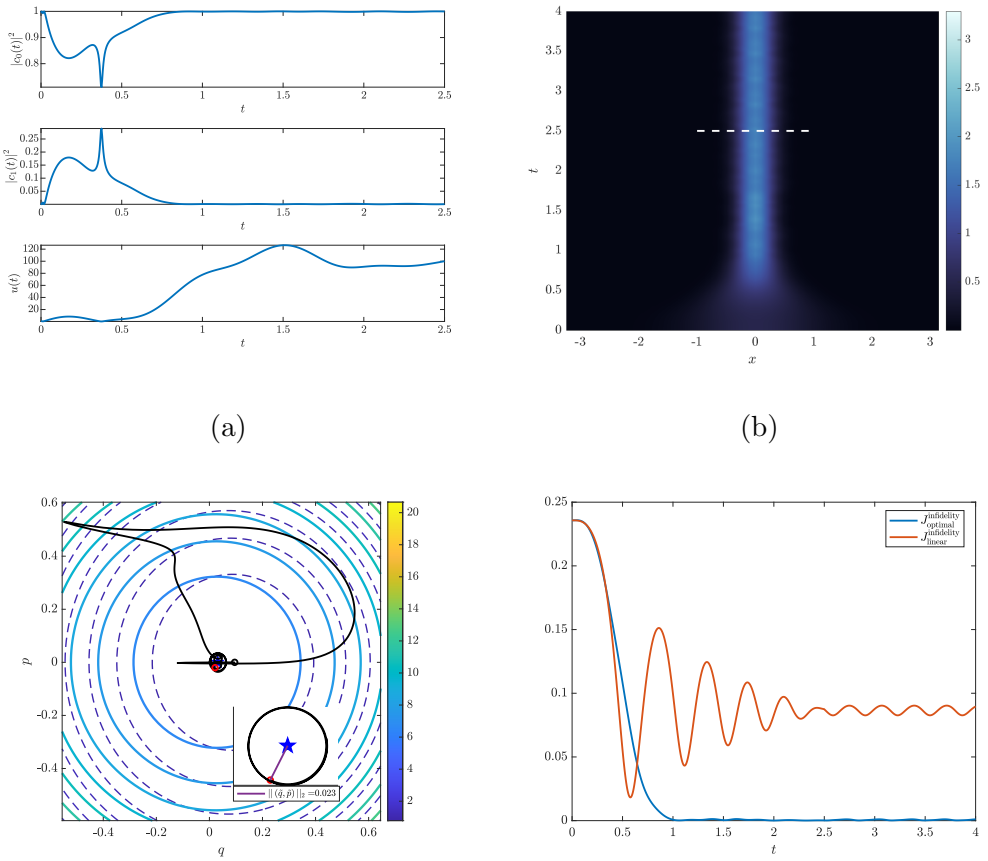

Figure 3.8 The result of using the hybrid optimization technique outlined in Section 2.4. The conventions used here are identical to those used in Figure 3.7. Panel (d) shows the infidelity (3.52) of the optimal control and infidelity of the linear control from Figure 3.6.

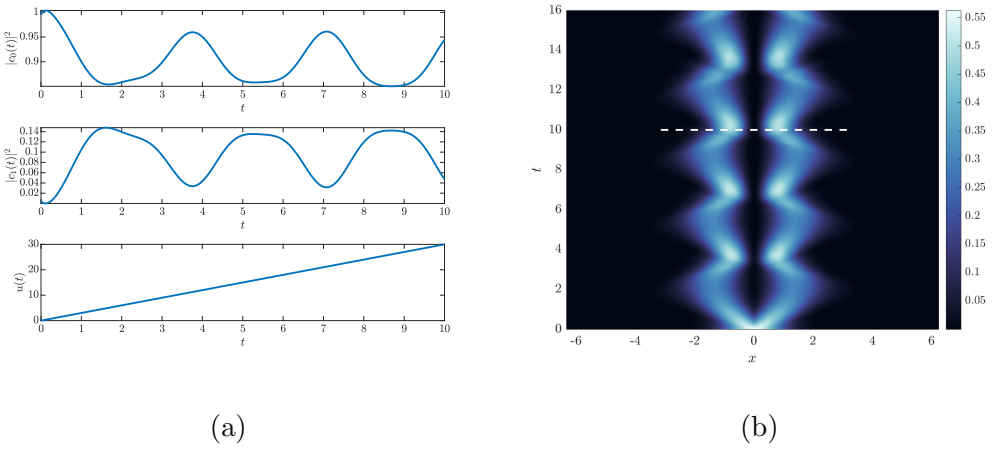

Figure 3.9 The result of the splitting experiment using a linear ramp. The conventions used here are consistent with Figure 3.4.

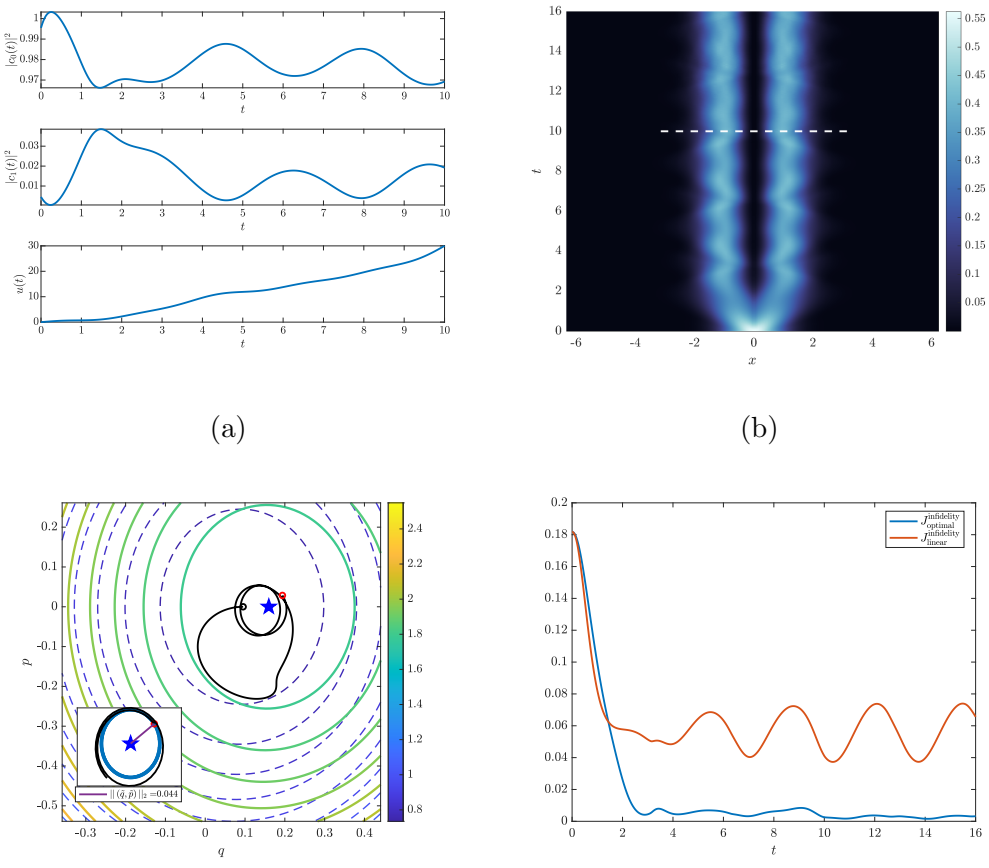

Figure 3.10 The result of using the CRAB method on the splitting problem of Section 3.2. The same conventions of Figures 3.4 and 3.8 are used here.

3.6 Experience Gained and Transition to More Difficult Control Problems

Although we pursue a reduction of the GPE dynamics to a single non-autonomous degree of freedom, optimal control problems in this dimensionally reduced setting are still highly effective by several accounts. Moreover, we provide a complete characterization of the physics of controlled condensates using standard dynamical systems techniques. It is easy to see the techniques of this chapter can be applied to other control problems constrained by Hamiltonian PDE, and perhaps to problems where posing an optimal control problem is challenging, if not impossible, without the visual aid of a phase diagram in a low dimensional setting.

On a more practical level, the reduced dynamical systems studied throughout this chapter offer opportunities to apply the methods of optimal control in a basic, yet still technologically relevant setting. Now equipped with this experience, transitioning to solving more challenging PDE constrained optimization setting is made simpler. The basic optimal control framework and methodology remains nearly invariant, and the bulk of the computational effort is placed on numerically solving the constraining PDE.

CHAPTER 4

OPTIMAL RESHAPING OF STATIONARY STATES IN LINEARLY DISPERSIVE MEDIA

4.1 Introduction

This chapter addresses another important problem from nanoscale engineering; the problem of reshaping light in a linearly refractive waveguide. As discussed in Section 1.3, Schrödinger's equation (1.5) governs the relevant state dynamics, and from this perspective, the control function we search for represents a confining potential. The work presented in this chapter is influenced by and aimed at extending work due to Kunkel and Leger [36].

We provide a natural generalization of the light reshaping problem of Kunkel and Leger which also allows the use of methods from the quantum control literature, e.g. [9, 14, 23, 34, 46, 63, 72]. Since the methods and formulations presented here are more general, this work is applicable to a potentially wider range of problems which the methods of Kunkel and Leger may not be able to address.

Another novelty of this chapter is in how we address the practical and computational aspects of a medium to large-scale optimization problem. Since the potentials we consider are multi-dimensional, i.e., they are functions of the waveguide's transverse and axial directions, we seek to appropriately reduce the search space of optimal controls. One of these reductions assumes a particular form of the potential along the transverse dimension with axially dependent parameters. Another reduction used, originally by Kunkel and Leger [36], is a partition of the optimal control problem into a small number of stages along the axial direction. The utility of these methods is demonstrated numerically on three reshaping problems including the reshaping problems shown in Figures 1.3 and 1.4.

4.2 General Problem Setup

The control problem we consider in this chapter uses the objective of Hohenester, et al., constrained by a class of linear dispersive wave equations which includes the Schrödinger Equation (1.5). The objective of the problem is to find an appropriately defined control which aids in dispersively evolving an initial stationary state into another stationary state at the axial end of the waveguide. With this in mind, let $x \in \mathbb{R}^n$ be the transverse coordinate, $\gamma > 0$ be a Tikhonov regularization parameter, and $z \in (0, l)$ be the axial coordinate, with $l > 0$. The optimal control problem we pose is

$$\inf_{u \in \mathcal{U}} J = \inf_{u \in \mathcal{U}} \left\{ \frac{1}{2} \left(||\varphi_d(\cdot)||^4_{L^2(\mathbb{R}^n)} - |\langle \varphi_d(\cdot), \psi(\cdot, l) \rangle|^2_{L^2(\mathbb{R}^n)} \right) + \frac{\gamma}{2} \int_0^l |\partial_z u|^2 \, dt \right\}, \quad (4.1)$$

subject to the dispersive initial value problem

$$i\partial_z \psi + P(x, u, D)\psi = 0, \quad (4.2a)$$

$$\psi(x, 0) = \varphi_0(x). \quad (4.2b)$$

The differential operator P is defined by

$$P(x, u, D) = \sum_{|\alpha| \leq m} a_\alpha(x, u) D^\alpha, \quad (4.3)$$

where the multi-index α is a set of n integers, P is at least a first-order operator, i.e., $m > 0$, the coefficients $a_\alpha(x, u)$ are functions in $C_b^0([0, l]; H^{m-1}(\mathbb{R}^n))$, and

$$D^\alpha := \frac{\partial^{\alpha_1}}{\partial x_j^{\alpha_1}} \cdots \frac{\partial^{\alpha_n}}{\partial x_j^{\alpha_n}}.$$

The space $C_b^k(\Omega)$ is the space of essentially bounded, k-times continuously differentiable functions, i.e.,

$$C_b^k(\Omega) := C^k(\Omega) \cap L^\infty(\Omega). \quad (4.4)$$

The only restrictions on the class of operators $P(x, u, D)$ we consider are that the point spectrum associated with P is non-empty and Whitham's dispersive

wave criteria is satisfied, i.e., the dispersion relation has only real roots and the determinant of its Hessian is non-vanishing [77]. The search for optimal controls is performed over the admissible class $\mathcal{U} = \{u \in H^1([0,l]) : u(0) = u_0, u(l) = u_l\}$.

The initial condition $\varphi_0(x)$ and the desired state $\varphi_d(x)$, are chosen such that

$$-P(x, u(0), D)\varphi_0(x) = \lambda_0\varphi_0(x), \tag{4.5a}$$

$$-P(x, u(l), D)\varphi_d(x) = \lambda_d\varphi_d(x), \tag{4.5b}$$

i.e., they are the initial and terminal eigenfunctions of the linear operators $P(x, u(z), D)$. We assume these eigenfunctions are both in the space $H^{m-1}(\mathbb{R}^n)$. We also assume that the eigenfunctions φ_0 and φ_d have the same "mass", i.e., $||\varphi_0||_{L^2(\mathbb{R}^n)} = ||\varphi_d||_{L^2(\mathbb{R}^n)}$ so that the infimum of the infidelity in objective (4.1) is 0.

Remark In the case of $P = \frac{1}{2}\Delta - V(x,u)$, the constraint dynamics (4.2a) reduce to the Schrödinger Equation (1.5). With the above assumptions in place, the regularity of the wavefunction ψ solving Equation (1.5) is known [44]; $\psi \in C^1([0,l]; H^1(\mathbb{R})^n)$. Moreover, in this case, the Schrödinger control problem with objective functional (4.1) is well-posed for sufficiently large $\gamma > 0$ [33]. General results on the regularity of wavefunctions ψ for operators P with an arbitrary multi-index α and well-posedness of the corresponding control problem is, of course, not known.

In Appendix B.1, we formally derive the optimality conditions for the problem with Objective (4.1) constrained by Equation (4.2a). We find

$$i\partial_z p = P^\dagger p, \qquad ip(x,l) = \langle \varphi_d, \psi(x,l)\rangle_{L^2(\mathbb{R}^n)}\, \varphi_d, \tag{4.6a}$$

$$\gamma\partial_z^2 u = -\Re\left\langle p, \partial_u P\psi\right\rangle_{L^2(\mathbb{R}^n)}, \qquad u(0) = u_0,\ u(l) = u_l, \tag{4.6b}$$

where † is the Hermitian adjoint operator. Note that these equations generalize the optimality conditions of the Pontryagin Principle (2.3.1) to a linear PDE setting

in the case of differential operators P smooth enough with respect to controls u. Equation (4.6a) is the adjoint equation of Equation (4.2a) and governs the axial evolution of the costate p backwards from the terminal condition. Equation (4.6b) governs the optimal control u, and together with the boundary conditions defined through the admissible class $\mathcal{U}$, is a boundary value problem on $[0, l]$.

4.3 Beam Reshaping with the Pöschl-Teller Potential

For the remainder of the chapter, we commit to numerical demonstrations involving Schrödinger's equation with transverse coordinate $x \in \mathbb{R}$. In order to demonstrate the beam reshaping problem in a simple setting, we consider initial and terminal eigenfunctions for which $V(x, u(0))$ and $V(x, u(l))$ can be computed in closed form.

It is well-known that the so-called Pöschl-Teller potential,

$$V(x) = -\frac{s(s+1)}{2}\operatorname{sech}^2(x),$$

has associated Legendre functions as eigenfunctions for the time-independent Schrödinger equation [54]. Therefore, we consider the problem of reshaping the ground state eigenfunction for $s = 1$ to the ground state corresponding to $s = 4$. We find that parametrizing the potential $V(x)$ with a depth control $u(z)$ and a width control $v(z)$ to be sufficient in our search for an optimal, axially varying Pöschl-Teller potential. More precisely, we assume the following form of the potential

$$V(x, u(z), v(z)) = -\frac{u(z)}{2}\operatorname{sech}^2(v(z)x), \tag{4.7}$$

where the initial and terminal eigenfunctions are given by

$$\varphi_0(x) = -\frac{1}{\sqrt{2}}\operatorname{sech}(x), \tag{4.8a}$$

$$\varphi_d(x) = -\frac{3}{2\sqrt{3}}\operatorname{sech}^2(x), \tag{4.8b}$$

and the appropriate control boundary conditions are

$$u(0) = 2, \quad u(l) = 20, \tag{4.9a}$$

$$v(0) = 1, \quad v(l) = 1. \tag{4.9b}$$

In the context of the dispersive constraint (4.2a), the differential operator $P(x, u, v, D)$ is $\frac{1}{2}\frac{\partial^2}{\partial x^2} - V(x, u, v)$. Optimality conditions (4.6a)–(4.6b), along with constaint (4.2a), reduce to

$$i\partial_z \psi = -\frac{1}{2}\partial_x^2 \psi + V(x, u(z), v(z))\psi, \qquad \psi(x, 0) = \varphi_0(x), \tag{4.10}$$

$$i\partial_z p = -\frac{1}{2}\partial_x^2 p + V(x, u(z), v(z))p, \qquad ip(x, l) = i\left\langle \varphi_d, \psi(x, l)\right\rangle_{L^2(\mathbb{R})} \varphi_d(x), \tag{4.11}$$

$$\gamma\partial_z^2 u = -\Re\left\langle p, \partial_u V\psi\right\rangle_{L^2(\mathbb{R})}, \qquad u(0) = u_0,\ u(l) = u_l, \tag{4.12}$$

$$\gamma\partial_z^2 v = -\Re\left\langle p, \partial_v V\psi\right\rangle_{L^2(\mathbb{R})}, \qquad v(0) = v_0,\ v(l) = v_l. \tag{4.13}$$

We briefly note that Equations (4.10)–(4.13) are linearized versions of the optimality conditions for the system whose dynamics are governed by the GPE (3.1), see e.g. [34].

We use the hybrid method outlined in Section 2.4 to solve the resulting optimal control problem. In order to solve the state equation (4.10) and costate equation (4.11), we use a split-step Fourier method identical to the one used for the GPE (3.1), mutatis mutandis, which is outlined in Appendix A.1. These methods assume periodic boundary conditions. Therefore, we truncate the transverse domain such that interference from the periodic boundary is minimal yet the domain is still small enough to make numerical computations feasible. Also, recall that in order to compute the control gradients of objective (4.1) which preserve boundary conditions (4.9a) and (4.9b), we require the numerical solution of the boundary value problems (2.45) with inhomogenieties given by Equations (4.12) and (4.13). To this end, we use Chebyshev collocation [70] with the second order

differentiation matrix given by

$$
\begin{aligned}
(D_N)_{00} &= \frac{2N^2+1}{6}, \\
(D_N)_{NN} &= -\frac{2N^2+1}{6}, \\
(D_N)_{jj} &= -\frac{x_j}{2\left(1-x_j^2\right)}, \qquad j = 1, ..., N-1, \\
(D_N)_{ij} &= \frac{c_i}{c_j}\frac{(-1)^{i+j}}{(x_i - x_j)}, \qquad j = 1, ..., N-1,
\end{aligned}
\tag{4.14}
$$

where N is the number of axial points, and use MATLAB's "backslash" command to invert it.

In this section, we choose the following domain and discretization parameters: $l = 3$, $l \times 2^7$ discretization points in z, and $x \in [-4\pi, 4\pi]$ with 2^{11} discretization points. In order to gauge the efficiency of a computed optimal control, we compare our results to a naive control strategy, i.e., assuming $u(z)$ and $v(z)$ are linear functions. We see the suboptimality of a naive control strategy in Figure 4.1.

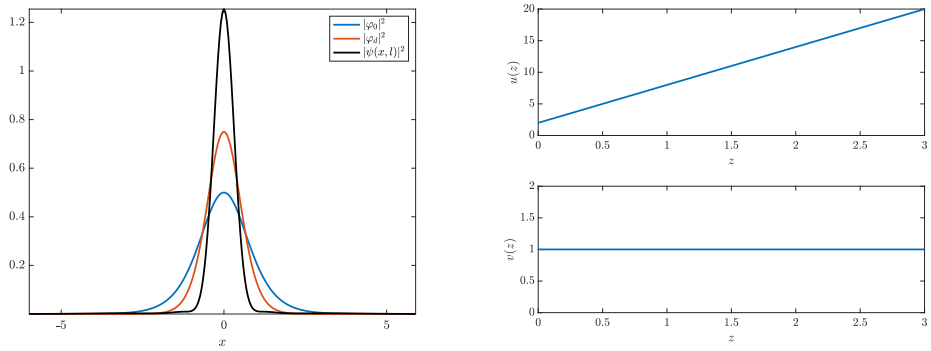

(a) (b)

Figure 4.1 The result of deepening the Pöschl-Teller potential (4.7) linearly over time without varying the width. Panel (a) shows the intensity profiles of the initial and terminal eigenfunctions and the computed solution of Schrödinger's Equation (4.10) with potential (4.7) corresponding to the controls in Panel (b).

To test GRAPE, the iterative indirect method of Subsection 2.4, we use the linear controls used to generate Figure 4.1 as initial controls. Also, we choose the Tikhonov regularization parameter $\gamma = 10^{-6}$, and backtracking parameters $\alpha = .4$ and $c = .5$ as they appear in the context of Inequality (2.39), for the remainder

of the chapter. We show, in Figure 4.2, the beam reshaping has only marginally improved. Although we see the gradient descent has converged, this result is not inspiring.

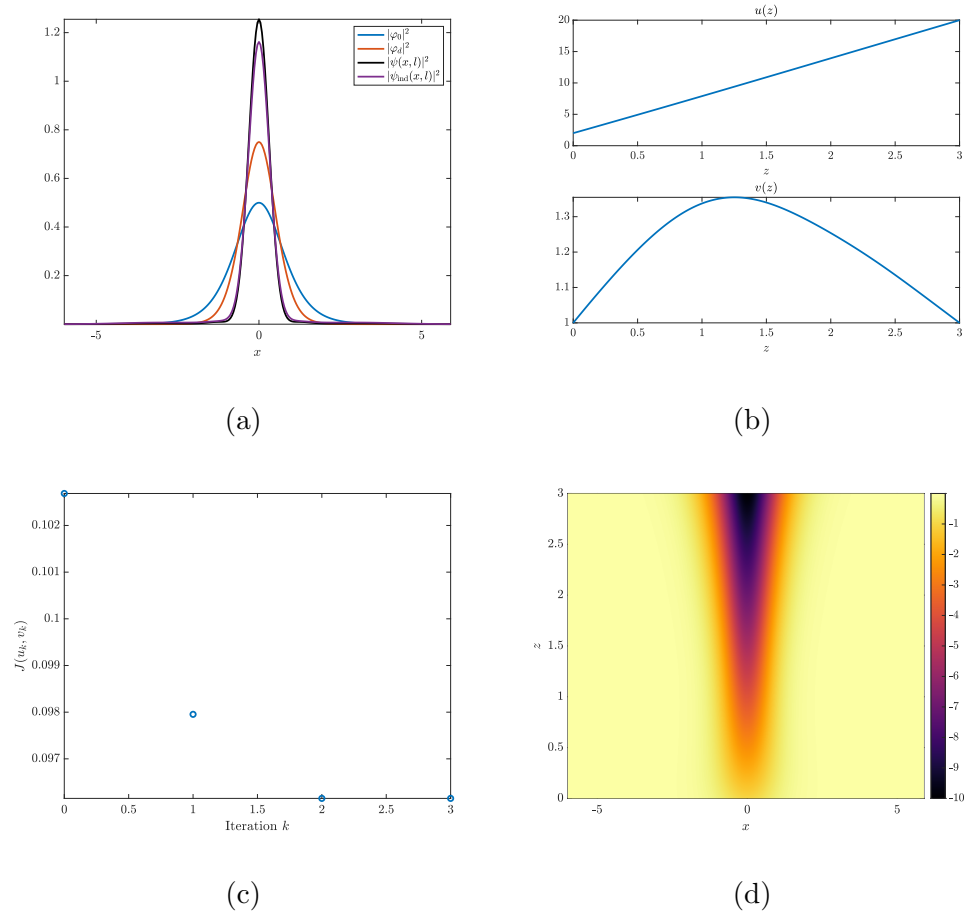

Figure 4.2 The result of using the gradient descent method of Subsection 2.4.4 using the linear controls of Figure 4.1 as initial guesses. Panel (a) shows intensity profiles for the relevant eigenfunctions and computed wavefunctions corresponding to linear controls and the computed controls shown in Panel (b). Panel (c) demonstrates the local convergence of the method while Panel (d) is the resulting potential $V(x, u(z), v(z))$, c.f. Equation (4.7).

We now turn to the CRAB method of Subsection 2.4.2. In the context of Algorithm 2, we use parameters $R_C = 0.9$, $F = 0.8$, $N_{\text{pop}} = 40$, and iterate 70 times. We use only 10 sine modes for each control function $u(z)$ and $v(z)$ required

by Equation (2.23), i.e.,

$$u_r(z) = (u_l - u_0)\sum_{j=1}^{10} \frac{r_u}{j^2} \sin\left(\frac{j\pi z}{l}\right) + (u_l - u_0)\frac{z}{l} + u_0, \tag{4.15a}$$

$$v_r(z) = \sum_{j=1}^{10} \frac{r_v}{j^2} \sin\left(\frac{j\pi z}{l}\right), \tag{4.15b}$$

where r_u and r_v are random variables drawn uniformly from $[-1, 1]$. We find several control functions u and v perform significantly better than the previous computations shown in Figures 4.1 and 4.2 with respect to the objective functional (4.1). One computational result is shown in Figure 4.3.

We see that the CRAB method essentially solves the Pöschl-Teller beam reshaping problem on its own without assistance of a further gradient descent. Although not shown, an application of a gradient descent method does not improve the result to machine precision. For this reason, we conclude the result of Figure 4.3 is a local minimum and extremely competitive among the many global minimizers that may exist for this optimal control problem.

4.4 The Beam Reshaping Problems of Kunkel and Leger

4.4.1 The Top Hat Problem

We now consider beam reshaping problems originally considered by Kunkel and Leger [36]. The first of these problems, shown in Chapter 4 through Figure 1.3, involves the transformation of some exactly known eigenfunction/potential pair into the "top hat" mode

$$\varphi_{\text{tophat}}(x) = Ae^{-ax^m}, \tag{4.16}$$

where A is a normalization coefficient, and, for the sake of computational demonstration, we choose $a = 10^{-3}$ and $m = 8$. The terminal potential which has φ_{tophat} as its ground state eigenfunction is not known in closed-form. Therefore, the first step in attacking the top hat problem is to numerically solve an inverse problem. The inverse problem of determining a potential given its eigenfunction is an example of an inverse scattering problem [52].

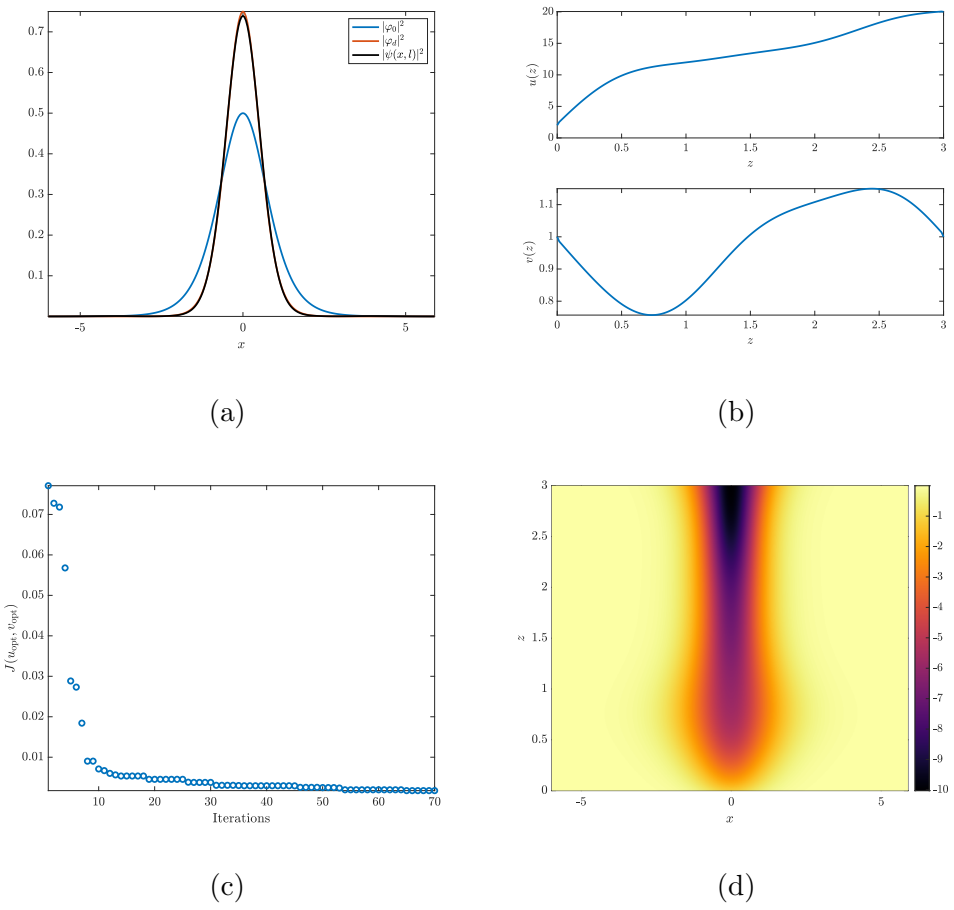

Figure 4.3 The result of using the CRAB method. The above panels demonstrate computational results in the same format as Figure 4.2. Panel (c) shows the fidelity of optimal members from each iteration of differential evolution and are denoted by u_{opt} and v_{opt}.

The inverse scattering problem we are now tasked with solving can be posed as the least squares problem:

$$\min_{V_l(x)\in C^0(\mathbb{R})} J = \min_{V_l(x)\in C^0(\mathbb{R})} \frac{1}{2}||\varphi_{\text{tophat}}(x) - \varphi(x; V_l(x))||^2_{L^2(\mathbb{R})} \tag{4.17}$$

subject to

$$-\frac{1}{2}\partial_x^2\varphi(x) + V_l(x)\varphi(x) = \lambda\varphi(x). \tag{4.18}$$

In order to solve this problem, we use MATLAB's `fmincon` to solve the least-squares problem (4.17) via routine optimization methods while using a pseudo-spectral method to compute the Schrödinger eigenfunctions from Equation (4.18). Solving this inverse scattering problem appears and is fairly routine outside of the issue of appropriately truncating the transverse domain. The naive approach of making the transverse domain sufficiently large and then truncating introduces significant round-off error. Fortunately, the so-called Sinh-Cloot change of variables $x = \sinh(c\xi),\ \xi \in [-\pi, \pi],\ c > 1$, facilitates solutions of Equation (4.18) in a way that suffers less severely from round-off [11]. Using the Sinh-Cloot change of variables, the linear operator present in Equation (4.18) is now

$$\begin{aligned} L &= -\frac{1}{2c^2}\operatorname{sech}(c\xi)d_\xi\left(\operatorname{sech}(c\xi)d_\xi\varphi\right) + V_l(x) \\ &= -\frac{1}{2c^2}\operatorname{sech}(c\xi)\Re\left\{\mathcal{F}^{-1}\left\{k^2\mathcal{F}\left\{\operatorname{sech}(c\xi)\varphi\right\} - ikc\mathcal{F}\left\{\operatorname{sech}(c\xi)\tanh(c\xi)\varphi\right\}\right\}\right\} + V_l(x), \end{aligned} \tag{4.19}$$

where $\mathcal{F}, \mathcal{F}^{-1}$ denote the forward and inverse Fourier transformation pair, respectively, which diagonalize the operator L [70]. We compute Fourier and inverse Fourier transforms via MATLAB's `fftw` and `ifftw` functions, and pass the operator as an anonymous function into MATLAB'S `eigs` in order to calculate the spectrum. We show the resulting top hat potential V_l from this procedure, with $c = 3$, in Figure 4.4

Once $V_l(x)$ has been computed, we are prepared to address the beam reshaping problem. We reduce the search space of possible potentials by assuming

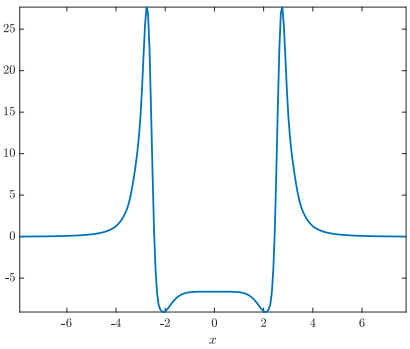

Figure 4.4 The resulting top hat potential which solves the inverse scattering problem (4.17) with top hat eigenfunction (4.16).

they take the following form:

$$V(x,z) = u(z)V_0(x) + v(z)V_l(x), \tag{4.20}$$

where $u(l) = v(0) = 0$, and $u(0) = v(l) = 1$. For sake of numerical demonstration, we choose $V_0(x)$ to be the Pöschl-Teller potential (4.7) with $s = 1$ and choose the length of the axial domain to be $l = 7$.

We show the results of the optimal control problem using the hybrid method of Section 2.4 in Figure 4.5. We use a CRAB given by

$$u_r(z) = \sum_{j=1}^{10} \frac{r_u}{j^2} \sin\left(\frac{j\pi z}{l}\right) + 1 + \frac{z}{l}, \tag{4.21a}$$

$$v_r(z) = \sum_{j=1}^{10} \frac{r_v}{j^2} \sin\left(\frac{j\pi z}{l}\right) - \frac{z}{l}, \tag{4.21b}$$

and use the DE parameters from Section 4.3 to search for the amplitudes r_u and r_v. The result is then refined by Algorithm (3) in the space $\dot{H}_0^1([0,l])$. In order to better show the solution of the Schrödinger equation over both the axial and transverse dimensions, we use the logarithmic scale

$$S(\psi) = \log(|\psi|^2 + \epsilon), \tag{4.22}$$

where $\epsilon > 0$. Figure 4.5(a) shows the agreement between the intensity profiles of $\varphi_d(x) = \varphi_{\text{tophat}}(x)$ (in red) and $\psi(x,l)$ (in black).

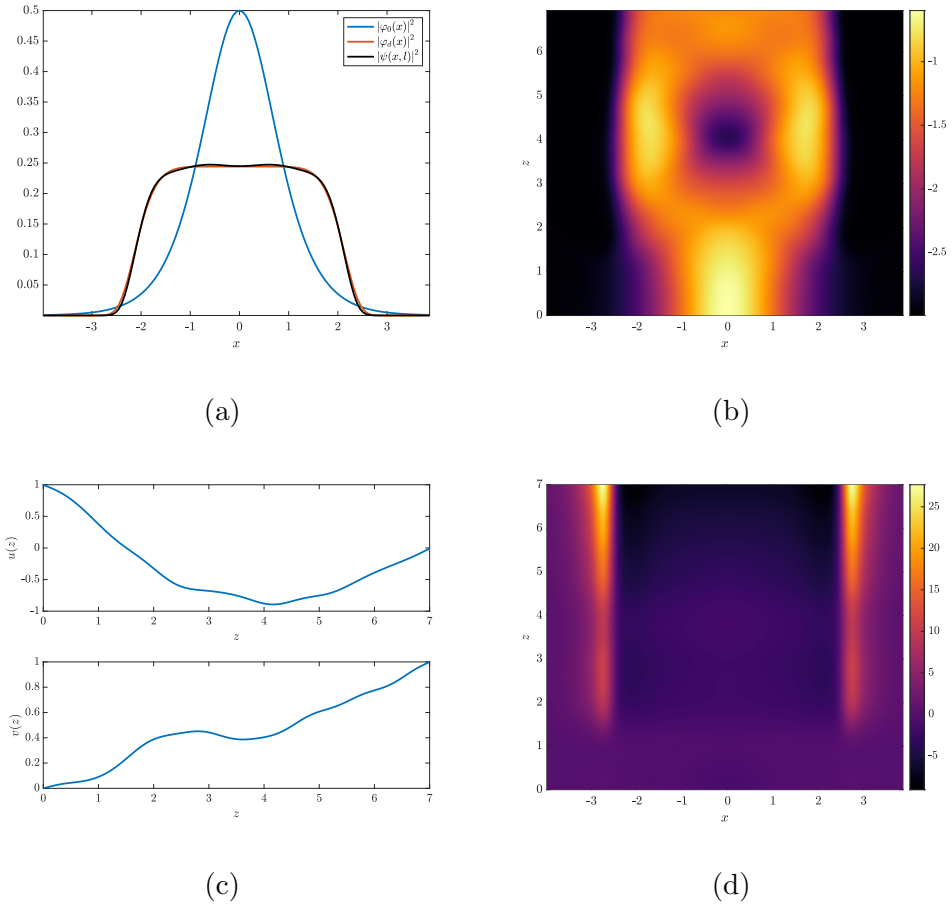

(a) (b)

(c) (d)

Figure 4.5 A numerical solution of the top hat problem. Panel (a) shows the intensity profiles for the initial, desired, and final computed wavefunctions . Panel (b) shows the axial evolution of the wavefunction intensity on the logarithmic scale (4.22) with $\epsilon = 0.5$. Panel (c) shows the computed controls $u(z)$ and $v(z)$ resulting from the hybrid method. Panel (d) shows the optimal potential resulting from panel (c) and the assumed form (4.20).

4.4.2 The Beam Combining Problem

The "beam combining" problem is another problem considered by Kunkel and Leger where the intention is to merge several pulses into one, c.f. Figure 1.4. To this end, we choose to use an initial configuration of three seperated Pöschl-Teller potentials, i.e.,

$$V_0(x) = -\frac{1}{2}\left(\operatorname{sech}(x-a)^2 + \operatorname{sech}(x+a)^2 + \operatorname{sech}(x)^2\right), \tag{4.23}$$

$$\varphi_0(x) = -\frac{1}{\sqrt{6}}\left(\operatorname{sech}(x-a) + \operatorname{sech}(x+a) + \operatorname{sech}(x)\right), \tag{4.24}$$

with a positive spacing parameter a. Although $\varphi_0(x)$ is not exactly an eigenfunction of $V_0(x)$, the approximation that $\varphi_0(x)$ is an eigenfunction improves upon choosing a large enough; we use a value of $a = 10$.

We find Kunkel and Leger's strategy of breaking the optimal control problem into two stages is valuable. In the context of this problem, we first perform an optimization on the interval $[0, 30]$ where we use $V_0(x)$ as an initial potential and the top hat potential solving Equation (4.17) and shown in Figure 4.4 as the terminal potential $V_l(x)$ in the ansatz (4.20). We use the CRAB (4.21), use DE parameters consistent with Section (4.3), and refine using a gradient descent in $\dot{H}_0^1([0, 30])$. We then perform a similar optimization on the interval $[40, 70]$ where the terminal data, i.e., the terminal potential and resulting terminal wavefunction, is used as initial data and the now terminal potential is given by a single Pöschl-Teller potential with $s = 3$.

We further refine our results by relaxing the restriction of the search space from the assumed form (4.20) via a gradient descent on a wider space. That is, we perform a full two-dimensional gradient descent on the potential $V(x, z)$ resulting from the two-stage optimization. To compute the gradient in this case requires a solution of the Dirichlet problem

$$\nabla_{x,z}^2 \nabla_V \mathcal{J} = -\delta_V \mathcal{J}, \tag{4.25a}$$

$$\nabla_V \mathcal{J}\big|_{\partial\Omega} = 0, \tag{4.25b}$$

where the inhomogeneity is given by

$$-\delta_V \mathcal{J} = \gamma \nabla^2_{x,z} V + \Re \langle p, \psi \rangle_{L^2(\mathbb{R})}, \tag{4.26}$$

$\nabla^2_{x,z}$ is the Laplacian operator over x and z, and $\partial\Omega$ is the boundary of the computational domain $[-15\pi, 15\pi] \times [0, 70]$. Note that this is the method of von Winckel and Borzi, from Subsection 2.4.4, in the space $\dot{H}^1_0(\Omega)$.

Note that the source term (4.26) in Equation (4.25a) arises from Equation (4.6a) and involves the computation of the Laplacian $\nabla^2_{x,z}$ which itself arises from the proper modification of the Tikhonov regularization in objective (4.1). In order to solve the Dirichlet problem (4.25), we use the standard trick of adding Kronecker tensor products, denoted $\otimes$, of differentiation matrices, each over their respective orthogonal coordinates x and z, with identity matrices I of the appropriate size. More specifically,

$$\nabla^2_{x,z} \approx I_x \otimes D^2_x + D^2_z \otimes I_z, \tag{4.27}$$

where D^2_x and D^2_z are second order Chebyshev matrices given by Equation (4.14), and where $I_x,\ I_z$ are appropriately sized identity matrices. The gradient $\nabla_V \mathcal{J}$ is then found by reshaping the source term $-\delta_V \mathcal{J}$, numerically inverting the matrix operator given by approximation (4.27), and reshaping the resulting vector in one-to-one correspondence with the computational domain Ω. We compute the Laplacian present in inhomogeneity (4.26), similarly.

We find this method modestly refines the result of using a two-stage optimal control framework. Although the refinement is slight, there is satisfaction in that the space of computationally viable potentials has been thoroughly searched. For sake of brevity, we choose to show, in Figures 4.6 and 4.7, the final result of the von Winckel and Borzi method in $\dot{H}^1_0(\Omega)$, after inputting the optimal controls computed through the two-stage hybrid optimization strategy.

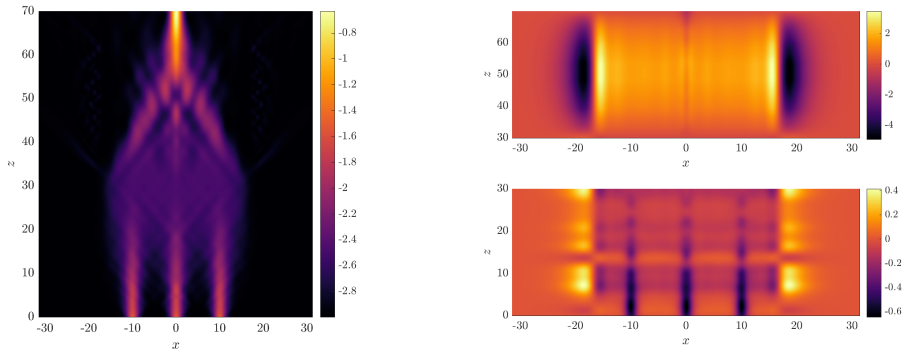

(a) (b)

Figure 4.6 A numerical solution of the beam combining problem (4.1) with initial data given by Equations (4.23), (4.24) and terminal data given by Equations (4.7), (4.8) with s=3. Panel (a) shows the resulting Schrödinger wavefunction $\psi(x, z)$ using the logarithmic scale (4.22) with $\epsilon = .1$, and Panel (b) shows the two stages of the computed optimal potential $V(x, z)$.

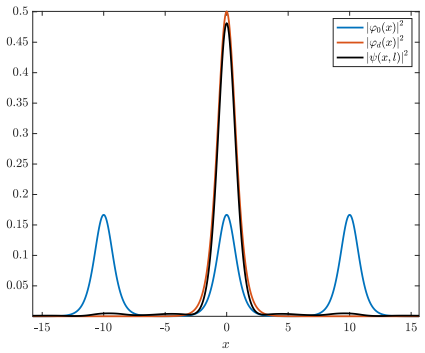

(a)

Figure 4.7 The initial, desired, and final computed intensity profiles, $|\varphi_0(x)|^2$, $|\varphi_d(x)|^2$, and $|\psi(x, l)|^2$, respectively, corresponding to Figure 4.6.

4.5 Conclusion and Future Work

The work presented in this chapter further demonstrates our capability of solving reshaping problems using the tools from the quantum control literature. We learn the utility of intuitive control strategies when tackling optimizations over large dimensional spaces. Indeed, we find that without using intuition to guide our searches, attempts to solve any of the reshaping problems in this chapter are extremely challenging.

In addition, the control problem (4.1) has constraints from a somewhat wide class of dispersive wave equations given by the Equation (4.2a). We observe, in Appendix B.1, the formally derived optimality conditions for the optimal control problem (4.1) are analogous to the optimality conditions in Pontryagin's principle (2.3.1). We pose future mathematical work concerning this observation here.

Problem: Well-Posedness of Eigenfunction Reshaping Problems Given an open set $\Omega \subset \mathbb{R}^n$, a spatial variable $x \in \Omega$, an evolution parameter $z \in [0, l]$, $l > 0$, the initial condition $\psi_0 \in \mathcal{B}_{\psi_0}(\Omega)$, desired condition $\varphi_d \in \mathcal{B}_{\psi_d}(\Omega)$, desired function space $\mathcal{B}_\psi$, and multi-index α, determine the admissible class $\mathcal{U}$ and admissible variable coefficients $a_\alpha(x, u(z)) \in \mathcal{B}_A$, present in the constraining Equation (4.2a), such that the optimality conditions of the control problem (4.1) are given by

$$\begin{aligned} i\partial_z \psi &= +\delta_{p^\dagger} \mathcal{H}, & \psi &\in \mathcal{B}_\psi \\ i\partial_z p^\dagger &= -\delta_\psi \mathcal{H}, & p &\in \mathcal{B}_\psi^*, \\ ip(x,l) &= \langle \varphi_d(\cdot), \psi(\cdot, l) \rangle_{L^2(\mathbb{R}^n)} \varphi_d(x), \\ \mathcal{J}[u^*] &= \min_{u \in \mathcal{U}} \mathcal{J}[u], \end{aligned} \tag{4.28}$$

where $\mathcal{B}_\psi^*$ is the dual of $\mathcal{B}_\psi$ and the Hamiltonian $\mathcal{H}$ is

$$\mathcal{H} = \Re \left\{ \langle p, P\psi \rangle_{L^2(\Omega)} - \langle \varphi_d, \psi \rangle_{L^2(\Omega)} \langle \partial_z \psi, \varphi_d \rangle_{L^2(\Omega)} \right\} + \frac{\gamma}{2} |\partial_z u|^2 . \tag{4.29}$$

Additionally, determine the saturation conditions analogous to those of Theorem (2.3.1).

The solution of this problem would first address the following question: for which domains Ω, initial conditions $\psi_0(x)$, and desired states $\varphi_d(x)$ can the regularity of the coefficients $a_\alpha(x, u(z))$ be determined such that the optimal control problem (4.1) is well-posed? The solution would then provide the admissible spaces $\mathcal{B}_A$ and $\mathcal{U}$.

It is, perhaps, more helpful to consider the simpler and particularly useful instances of this problem, such as when the wavefunction ψ is governed by a Schrödinger or Dirac operator and the spatial domain is given by $\Omega = \mathbb{R}^n$. Fixing the function spaces $\mathcal{B}_{\psi_0}$ and $\mathcal{B}_{\psi_d}$, the feasibility of the desired space $\mathcal{B}_\psi$ is determined by the possible choices of $\mathcal{B}_A$. If $\mathcal{B}_\psi$ is feasible, this leaves us with determining the space $\mathcal{U}$ such that the conditions (4.28) and the appropriate saturation condition, e.g. that the Hamiltonian $\mathcal{H}(\psi^*, p^*, u^*)$ is a constant independent of $x \in \mathbb{R}^n$ and z, follow.

We believe the solution of this problem appropriately generalizes Pontryagin's principle in this context. We are aware of similar work done for fixed-end point, free-time optimal control problems constrained by the Schrödinger equation (4.10) [40] and the wave equation [41], but none that precisely address the above stated problem, or one from a more general perspective. We hope that in posing this problem, we not only inspire future mathematical work, but also continue to motivate the use of the optimal control strategies used throughout this dissertation to problems in other mathematically similar, yet technologically different contexts.

In the coming chapter, we transition to a different experimental setting where the chief difficulty of designing technology is in posing the appropriate optimal control problem. Equipped with the computational methodologies developed so far throughout this dissertation, we address various PDE constrained optimization problems over the next three chapters. This methodology allows us to focus

more of our attention on the subtler issues associated with analytically and computationally modeling technology design through optimal control theory.

CHAPTER 5

APODIZER DESIGN TO EFFICIENTLY COUPLE LIGHT INTO A FIBER BRAGG GRATING

5.1 Experimental and Technological Context

Systems that dramatically slow light have been observed in a wide variety of experimental settings over the past two decades and offer enticing technological applications involving efficient optical switches, sensitive interferometry, and optical quantum memory [21]. Of the several experimental platforms which can generate slow light, fiber Bragg gratings (FBGs) offer the considerable advantage of having structural properties which can be tailored specifically to the light source characteristics.

An FBG is an optical element whose index of refraction varies periodically. The grating enables the fiber to attain a strong dispersion of light over a short distance due to a resonance between the grating's period and electromagnetic wavelengths near the Bragg wavelength $\lambda_{\mathrm{B}} = 2\bar{n}\Lambda$, where $\bar{n}$ denotes the average index of refraction in the fiber and Λ denotes the period of the structure, see Figure 1.5. The FBG strongly couples forward and backward propagating waves near the resonant wavelength. This creates a photonic bandgap, i.e., an interval of frequencies of low-amplitude light which are back-reflected. This bandgap is centered at the Bragg angular frequency $\omega_{\mathrm{B}} = \frac{\pi c}{\bar{n}\Lambda}$, where c is the speed of light in vacuum.

In the presence of materials with an appreciable Kerr nonlinearity, i.e., materials in which the index of refraction responds proportionally to the electric field intensity [49], high intensity light will shift the Bragg frequency. For positive nonlinearities, the refractive index increases with intensity, therefore shifting the Bragg frequency ω_{B} to lower ones. Lower frequencies near the value of the frequency ω_{B} in the absence of the Kerr effect are still Bragg reflected, but even more so with higher intensities. Meanwhile, higher frequencies are hardly

reflected at higher intensities. Therefore, at the edges of a high intensity region of light, the light is continuously Bragg reflected into the high intensity region which propagates through the grating seemingly unimpeded. Systems, such as these, which exhibit coherent structures arising from a balance between nonlinear effects and dispersion typically lead to the existence of solitary waves.

Indeed, Aceves and Wabnitz constructed a two-parameter class of solitary wave solutions [3], often called Bragg solitons to distinguish them from the classical notion of a soliton [52]. These waves solve evolution equations derived from Maxwell's equations using coupled-mode theory, which we briefly discuss in Section 5.2, and can travel with a speed anywhere from the speed of light in the medium down to zero. The existence of Bragg solitons demonstrates the possibility of slow light in FBG's. While Bragg solitons can in theory propagate at slow speeds, it is difficult to initialize such waves experimentally. To create a Bragg soliton, one must input light at a frequency inside the bandgap, and such frequencies are strongly reflected. Neglecting nonlinear effects, the FBG essentially acts as a band-stop filter, reflecting wavelengths whose frequency is within the bandgap.

To overcome this, Mok, et al. [48], use a two-pronged strategy to couple light into an FBG. First, they use an apodized grating, i.e., the grating strength is ramped up gradually from zero. Secondly, they input so-called out-gap solitons, wave packets with a mean frequency outside of the bandgap. As a result of the apodization, the light coupled into the grating has its frequency gradually shifted into the bandgap. Although this experiment is the first of its type and generated a pulse with a group velocity 16% that of light in vacuum, this pulse contained only about 20-30% of the the input energy, while the remaining light was back-reflected, rendering the setup highly inefficient.

In order to address this inefficiency, Rosenthal and Horowitz [57], designed a two-segment apodization function that allowed the creation of a pulse that retains about 68% of the incident energy and with a speed roughly 3.2% of light speed.

Despite this remarkable improvement in efficiency, the authors provide limited mathematical detail about the process behind discovering such a design. This leaves room for quantitative investigations into the efficiency of generating slow light using FBGs.

We build on the method of Rosenthal and Horowitz by mathematically formulating an appropriate optimal control problem. The objective of the problem is to design an apodization profile which maximizes the coupling of light into the FBG. By jointly optimizing the apodization profile with that of an additional parameter, the grating chirp, we achieve a higher coupling efficiency of 82.6% transmission, while further reducing the pulse speed to about 0.5% that of light.

This chapter is organized as follows: in Section 5.2, we provide the physical model and give precise details of the numerical experiments performed in the previous works mentioned that motivate ours. We attempt to gain intuition behind the experiment by performing fits of the numerical data to the Aceves and Wabnitz waveform. We also gain an understanding of the light/apodization interaction via computations of the associated power spectra. In Section 5.3, we formulate the optimal control problem which seeks to maximize the energy transmitted into the fiber while treating the grating structure as the control. We provide the necessary optimality conditions for the control problem and then present our numerical results in Section 5.4.

5.2 The Physical and Numerical Model

5.2.1 Brief Overview of Coupled-Mode Theory

The evolution of the electric field propagating in an optical fiber is governed by the one dimensional non-linear wave-equation

$$\partial_\tau^2 \left(n^2(z, E^2)E \right) = \partial_z^2 E, \tag{5.1}$$

in dimensionless units where the speed of light $c = 1$, and where z denotes the axial direction of propagation. Let ε be a small contrast of the index of refraction

n so that it can be modeled as [31]

$$n = 1 + \varepsilon \left(\nu(\varepsilon z) \cos(2k_{\mathrm{B}} z + 2\Phi(\varepsilon z)) + |E|^2 \right) \tag{5.2}$$

Here the coefficient ν describes the strength of the grating and Φ' describes the chirp, i.e., the local modulation of the grating's wavelength. The final term describes a Kerr nonlinearity with small Kerr coefficient ε.

Using a two-scale expansion with an ansatz,

$$E = \sqrt{\varepsilon} \left(u(\varepsilon z, \varepsilon\tau) e^{i(k_{\mathrm{B}}(z-\tau)+\Phi)} + v(\varepsilon z, \varepsilon\tau) e^{-i(k_{\mathrm{B}}(z+\tau)+\Phi)} \right) + \mathcal{O}\left(\varepsilon^{\frac{3}{2}}\right) \tag{5.3}$$

and letting $x = \varepsilon z$, $t = \varepsilon\tau$ denote the slow variables, the following system of hyperbolic equations, known as the nonlinear coupled-mode equations (NLCME),

$$\begin{aligned} i\partial_t u + i\partial_x u + \kappa(x) v + \eta(x) u + \left(|u|^2 + 2|v|^2 \right) u = 0, \\ i\partial_t v - i\partial_x v + \kappa(x) u + \eta(x) v + \left(2|u|^2 + |v|^2 \right) v = 0. \end{aligned} \tag{5.4}$$

arise as solvability conditions on the forward and backward slowly varying envelopes $u(x,t), v(x,t)$, respectively [31]. The coefficient $\kappa(x)$ is proportional to the local strength $\nu(x)$ of the grating while $\eta(x)$ is proportional to the local chirp $\Phi'(z)$. We refer to regions where $\kappa(x)$ and $\eta(x)$ are 0 as the bare fiber to indicate the absence of the grating.

For low-amplitude light, the NLCME reduce to a set of linear coupled-mode equations

$$\begin{aligned} i\partial_t u + i\partial_x u + \kappa(x) v + \eta(x) u = 0, \\ i\partial_t v - i\partial_x v + \kappa(x) u + \eta(x) v = 0. \end{aligned} \tag{5.5}$$

When κ and η are constant, this system has a dispersion relation given by

$$\Omega(Q) = \eta \pm \sqrt{Q^2 + \kappa^2}. \tag{5.6}$$

By introducing a chirp $\eta(x)$ into the grating, we see that this both shifts the center of and widens the bandgap, i.e., the set of frequencies $\Omega \in (\eta - \sqrt{Q^2+\kappa^2}, \eta + \sqrt{Q^2+\kappa^2}$ that are strongly reflected by the grating, see Figure 5.1.

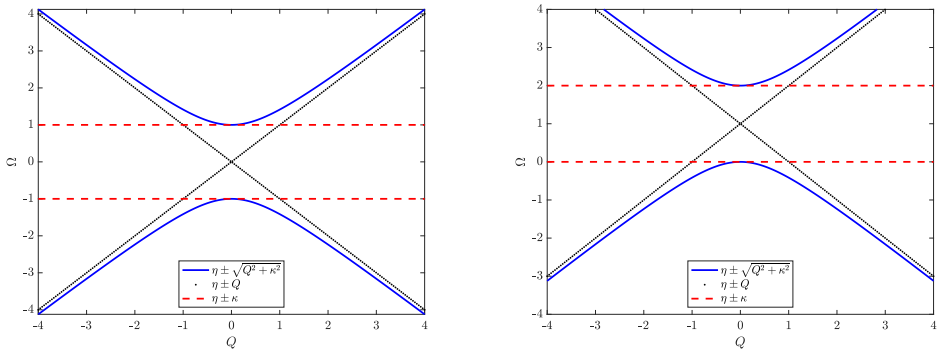

(a) (b)

Figure 5.1 Introducing a chirp η shifts and the bandgap present in the linear coupled-mode equations' (5.5) dispersion relation (5.6). Both panels have κ set to 1. Panel (a) has η set to 0 while Panel (b) has η set to 1.

In the case of a uniform grating, that is, where $\kappa \equiv \kappa_0$ and $\eta \equiv 0$, the NLCME admit a two-parameter family of translationally invariant solitary wave solutions, called Bragg solitons [3],

$$\begin{aligned} u_{\mathrm{B}} &= \sqrt{\frac{\kappa_0(1+c)}{3-c^2}}\left(1-c^2\right)^{1/4} W(X)\exp\left(i\phi(X) - iT\cos\theta\right), \\ v_{\mathrm{B}} &= -\sqrt{\frac{\kappa_0(1-c)}{3-c^2}}\left(1-c^2\right)^{1/4} W^*(X)\exp\left(i\phi(X) - iT\cos\theta\right), \end{aligned} \tag{5.7}$$

where

$$\begin{aligned} X &= \kappa_0\left(1-c^2\right)^{-1/2}(x-ct), \\ T &= \kappa_0\left(1-c^2\right)^{-1/2}(t-cx), \\ \phi(X) &= \frac{4c}{3-c^2}\arctan\left(\tanh\left(X\sin\theta\right)\tan\frac{\theta}{2}\right), \\ W(X) &= \sin\theta\ \mathrm{sech}\left(X\sin\theta - \frac{i\theta}{2}\right), \end{aligned} \tag{5.8}$$

with free parameters $0 \leq \theta \leq \pi$ and $-1 < c < 1$. The dependence of the Bragg soliton on the parameters, we can see, is quite complicated, but we make a few observations. The parameter c describes the velocity of the pulse, appears in a Lorentz contraction, and, through the factors $(1 \pm c)^{1/2}$, controls the relative amplitude of the forward and backward envelopes. Note that for stationary Bragg solitons, $c = 0$, the frequency of the stationary oscillation is given by $\kappa_0 \cos\delta$ so

as δ is increased from 0 to π, the frequency of the standing wave moves from the right edge of the band gap to the left edge, while always remaining inside the gap.

It is important to note the NLCME possess two conserved quantities, an energy

$$E = \int_{-\infty}^{\infty} \left(|u|^2 + |v|^2\right) dx := \int_{-\infty}^{\infty} \mathcal{E} dx, \tag{5.9}$$

and a momentum

$$P = i \int_{-\infty}^{\infty} \left(\partial_x u^\dagger u + \partial_x v^\dagger v\right) dx := \int_{-\infty}^{\infty} \mathcal{P} dx, \tag{5.10}$$

where $\dagger$ denotes complex conjugation. Allowing the coefficients to vary in space breaks the translation invariance, so that conservation of momentum fails to hold, however energy remains conserved. We make use of the energy (5.9) in posing an optimal control problem in Section 5.3.

5.2.2 The Numerical Setting

Using the physical modelling discussed in Subsection 5.2.1, we can now provide the numerical setting of the Rosenthal and Horowitz experiment. Let $\kappa(x)$ be the grating profile that grows from $\kappa = 0$ for $x \leq 0$ to a value κ_0 for $x \geq a > 0$. The pulse is launched with a fixed profile from a point $x = x_{\text{input}} < 0$ in the bare fiber and has a momentum directed toward the apodization region $x_{\text{apod}} \in [0, a]$. The Rosenthal and Horowitz experiment does not take into consideration the utility of a chirp $\eta(x)$. For this reason, we set $\eta \equiv 0$ in this section and postpone discussions of $\eta's$ role until we define the relevant optimal control problem in Section 5.3.

The existence of the solitary wave (5.7) demonstrates that slow light in FBGs is theoretically possible. Mok, et al., achieve 20% energy transmission, and significant slowing of light by simply using a raised cosine profile. Rosenthal and Horowitz significantly improve on the energy transmission by using two-segment apodization profiles of the form

$$\kappa(x) = \begin{cases} \frac{\zeta\kappa_0}{2}\left(1 - \cos\frac{\pi x}{L_1}\right) & 0 < x \leq L_1 \\ \zeta\kappa_0 + \frac{\kappa_0}{L_2}(1-\zeta)(x - L_1) & L_1 < x < a = L_1 + L_2. \end{cases} \tag{5.11}$$

The Mok, et al., design is simply the case $\zeta = 1$, and we provide a graph of the apodization profile (5.11), with $\zeta = 0.995$ in Figure 5.2.

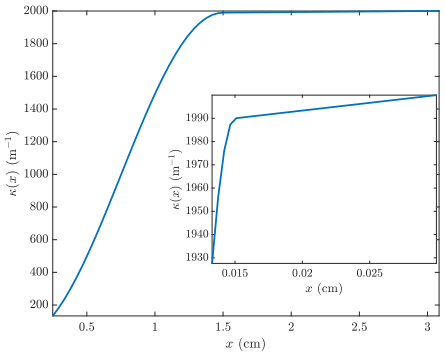

Figure 5.2 The Rosenthal and Horowitz apodization function (5.11), with $\zeta = 0.995$, $\kappa_0 = 2\text{mm}^{-1}$, and $L_1 = L_2 = 1.5\text{cm}$.

The experiment is modelled as a signaling problem, i.e., the solution is initialized by a time-dependent boundary condition at the "input" endpoint. Rosenthal and Horowitz use a three parameter family of input pulse data of the form

$$u(x_{\text{input}}, t) = A\text{sech}\left(\frac{t - \phi}{\sigma}\right) e^{-i\Omega t}, \quad v(x, 0) = 0, \tag{5.12}$$

where x_{input} denotes the left-most endpoint of the spatial domain, as an initial gap soliton outside the forbidden band gap of the dispersion relation (5.6). The intention of the experiment is to have **out–gap soliton** of the form (5.12) interact with the apodization (5.11), and, through the coupled-mode dynamics (5.4), transform into an **in–gap soliton** of the form (5.7).

We show a numerical reproduction of the Rosenthal and Horowitz experiment, alongside results of the Mok, et al., design, in Figure 5.3. There, we observe the vastly improved energy transmission resulting from choosing $\zeta = 0.995$, instead of $\zeta = 1$, in the apodization function (5.11). The choices of the remaining apodization

parameters, in SI units, are $L_1 = 1.5\text{cm}$, $L_2 = 1.5\text{cm}$, $\kappa_0 = 2\text{mm}^{-1}$, while the signalling data parameters are $A = 16.4\text{W}$, $\sigma = 96.4\text{ps}$, $\phi = 4\text{ns}$, and $\Omega = 0.398\text{GHz}$.

We use a second order in time operator splitting method, detailed in Appendix A.1, to solve Equation (5.4) with a spatial discretization of 4000 points and temporal discretization of 12000 points. We solve Equation (5.4) out to 6 ns, set $x_{\text{input}} = -20$ cm, and set the right endpoint to 16 cm. The numerical method and majority of these parameters will remain consistent throughout this chapter, unless otherwise noted.

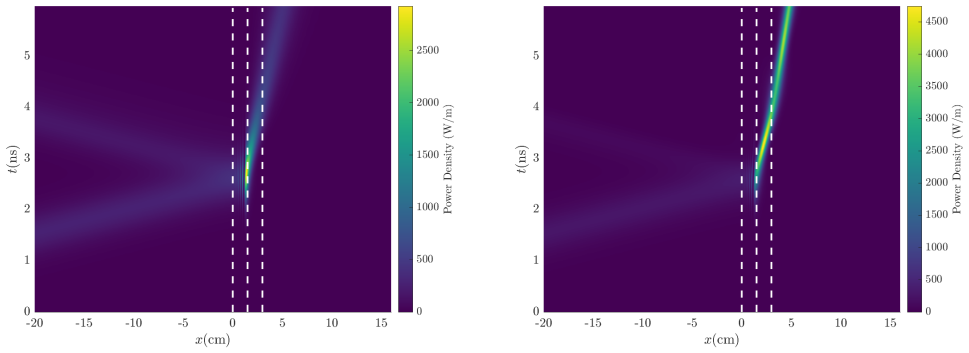

(a) (b)

Figure 5.3 Numerical simulations of Equation (5.4) with the apodization design (5.11) consistent with the parameters detailed in the text. Dashed lines provided to help visualize the regions in space over which the two segment apodization varies, cf. (5.11) and Figure 5.2. Panel (a) corresponds to the original Mok, et al., design, i.e., $\zeta = 1$, while Panel (b) has $\zeta = 0.995$.

To justify the incredible performance of the two-segment apodization function, Rosenthal and Horowitz appeal to ideas from soliton perturbation theory. They argue that the second segment of the apodization function *adiabatically* shifts the high-intensity waveform, initially at $x = L_1$, into the band gap, and, as a result, minimizes back-reflection. We believe the nature of this argument to be somewhat ad hoc, and the efficiency of the Rosenthal and Horowitz apodization as well as the interpretation of its results requires further investigation.

In order to gain traction with understanding the Rosenthal and Horowitz results shown in Figure 5.3, we attempt to fit spatial solitary waves of the form (5.7) to the numerical simulation data at specific times. The first fit is performed at the time $t = 3.42$ns, which is near the critical excitation time. By critical excitation time, we mean the time when the highly compressed waveform has reached its maximum amplitude. We also perform a fit at $t = 6$ns, well after the waveform has exited the apodization region $x \in [0, a]$. We show the fitting parameters and result at $t = 3.42$ns in Figure 5.4 and at $t = 6$ns in Figure 5.5. In these fits, we see somewhat convincing evidence the excited waveforms are Bragg solitons, especially in the power density.

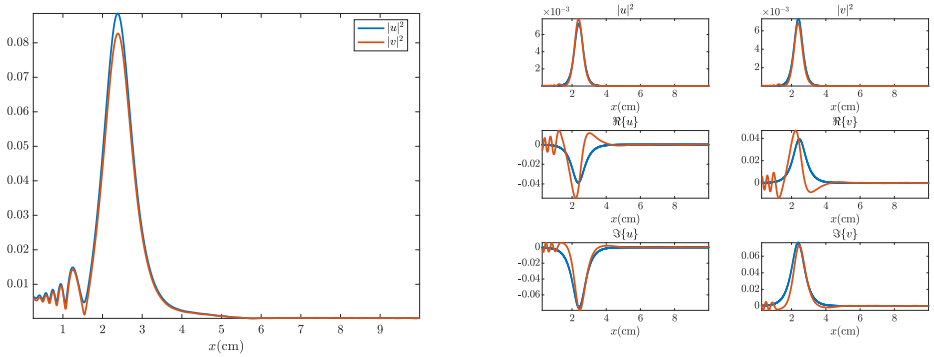

Figure 5.4 A least-squares fit of a Bragg soliton of the form (5.7) to the solution of the Rosenthal experiment at the critical excitation time $t = 3.42$ns. The least squares fit is performed on the waveform featured in Panel (a). Panel (b) displays the resulting fit with Bragg soliton parameters $c = 0.003$, $\theta = 6.14$, $\Psi_0 = 1.96$, and $T = -17900$.

The next step we take in order to better interpret the results of the Rosenthal and Horowitz experiment is to make use of spatial and temporal power spectra. Recall that the power spectrum of a function $f \in L^1(\mathbb{R})$ is the squared absolute value of the Fourier transform

$$\hat{f}(k) = \int_{-\infty}^{\infty} f(x) e^{-ikx} dx. \tag{5.13}$$

We show the spatial power spectrum of each moment in time, which, by Plancherel's theorem, is $\hat{\mathcal{E}}(k,t) = |\hat{u}(k,t)|^2 + |\hat{v}(k,t)|^2$, in Figure 5.6. Meanwhile, in Figure 5.7, we show the temporal power spectrum of each point in space, i.e.,

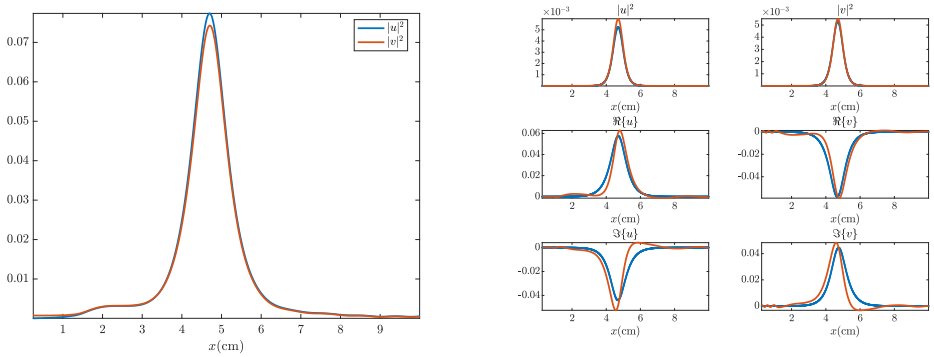

Figure 5.5 An attempt to fit a Bragg soliton of the form (5.7) in least squares to the solution of the Rosenthal experiment at the final time $t = 6$ns. The Bragg soliton parameters found are $c = -0.004,\ \theta = 6.16,\ \Psi_0 = 4.61$, and $T = -21,200$.

$\hat{\mathcal{E}}(x,\omega) = |\hat{u}(x,\omega)|^2 + |\hat{v}(x,\omega)|^2$. These power spectra are easily computed via the `fftw` function in MATLAB and visualized using the logarithmic scale (4.22) with $\epsilon = 1$.

We see that, indeed, allowing the apodization to vary slowly in space helps to broaden the spatial power spectrum centered about the $k = 0$ mode in Figure 5.6. We also see that this manifests in a denser temporal power spectrum in the forbidden band gap centered about $\omega = 0$ in Figure 5.7. At the critical excitation time, the Rosenthal and Horowitz scheme allows the incident out-gap soliton and the excited back-reflected out-gap soliton enough time to transfer their power spectra to the power spectrum centered at the in-gap soliton frequency. In this way, we begin to understand the adiabadicity hypothesis of Rosenthal and Horowitz.

We recenter our focus back on understanding to what extent the Rosenthal and Horowitz scheme is efficient. A brute force search over the dimensionless apodization parameters ζ and $\lambda \in (0,1)$, which determines the apodization lengths given by

$$L_1 = 3(1-\lambda) \text{ cm}, \quad L_2 = 3\lambda \text{ cm}, \tag{5.14}$$

easily addresses the desire to know the local efficiency of the Rosenthal and Horowitz apodization. We see, in Figure 5.8, the choice $(\lambda,\zeta)_{\text{RH}} = (0.5, 0.995)$ is not locally optimal. The optimal parameters $(\lambda,\zeta)_*$ we find through this search

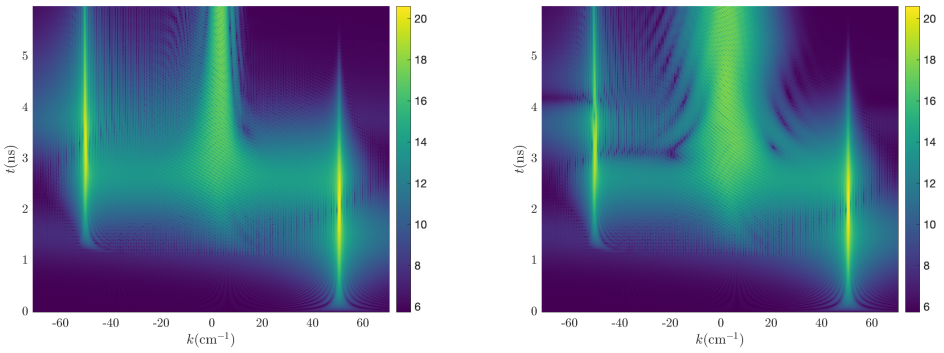

(a) (b)

Figure 5.6 Spatial power spectra $\hat{\mathcal{E}}(k,t)$, in the logarithmic scale (4.22), for the numerical data shown in Figure 5.3. The Mok, et al., power spectrum is shown in Panel (a) while the Rosenthal and Horowitz power spectrum is shown in Panel (b).

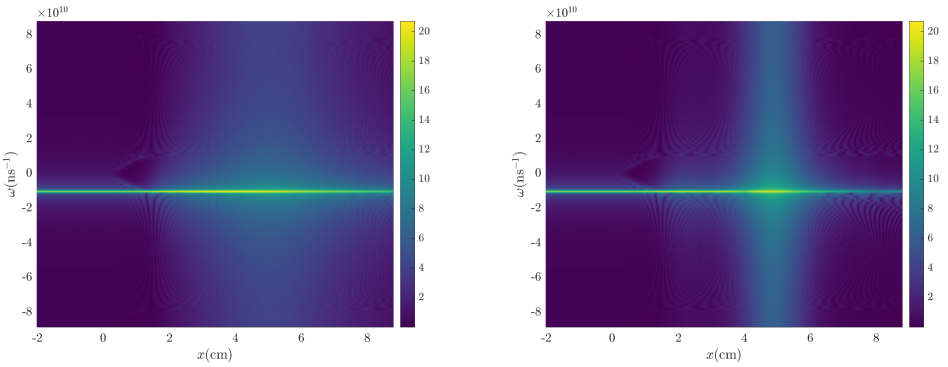

(a) (b)

Figure 5.7 Temporal power spectra $\hat{\mathcal{E}}(x,\omega)$, in the logarithmic scale (4.22), for the numerical data shown in Figure 5.3. The Mok, et al., power spectrum is shown in Panel (a), while the Rosenthal and Horowitz power spectrum is shown in Panel (b).

are in fact $(0.567, .99244)$. This greatly encourages the use of optimal control theory in a pursuit of apodization functions which optimally couples light into a Bragg grating.

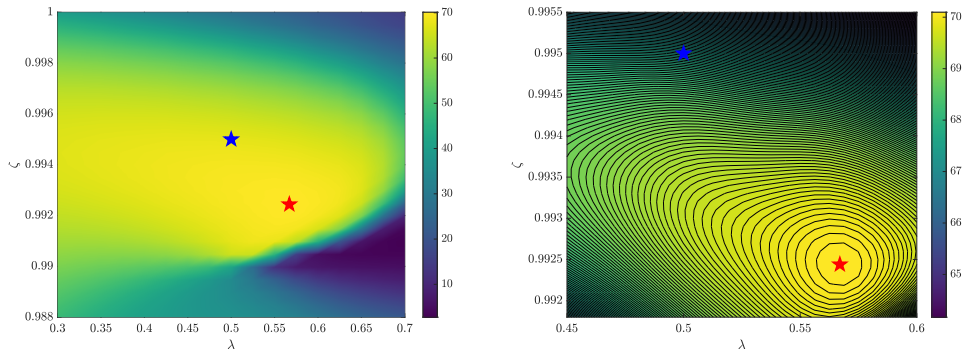

(a) (b)

Figure 5.8 A brute force search for the greatest transmitted fraction of energy in the 2-parameter family of apodizers, of the form (5.11), (5.14), with all other conventions consistent with that of Figure 5.3. The Rosenthal and Horowitz apodizer is the sub-optimal point $(\lambda, \zeta)_{\mathrm{RH}} = (0.5, 0.995)$, shown by the blue star, while the globally optimal point is $(\lambda, \zeta)_* = (0.567, .99244)$, shown by the red star.

5.3 The Optimal Control Formulation and Optimality Conditions

We now precisely formulate an optimal control problem whose objective is to find the grating structures which simultaneously fulfill the desired outcome of the Rosenthal and Horowitz experiment, yet maximize the transmission of light into the constant grating portion of the optical fiber. To this end, we make use of the following local conservation law

$$\partial_t \mathcal{E} + \partial_x \mathcal{F}_{\mathcal{E}} = 0, \tag{5.15}$$

where $\mathcal{F}_{\mathcal{E}}$ is the local energy flux. Note that this conservation law is the differential form of energy conservation, where the energy is given by Equation (5.9).

We treat the grating functions $\kappa(x)$ and $\eta(x)$ as the control functions, and assume that the apodization region is of fixed width $a > 0$, consistent with the Rosenthal and Horowitz apodization function (5.11). In addition, we

use the conventions consistent with those of Figure 5.2, including signalling data (5.12), length of the spatial domain, duration of simulation time, and number of discretization points. The admissible class $\mathcal{C}$ of grating functions we search over is the space of absolutely continuous functions such that

$$\kappa(x) = \begin{cases} 0 & x \leq 0, \\ \\ \kappa_0 & a \leq x, \end{cases} \quad \text{and} \quad \eta(x) = \begin{cases} 0 & x \leq 0, \\ \\ 0 & a \leq x. \end{cases} \tag{5.16}$$

Now, the optimal control problem we seek to solve is

$$\min_{(\kappa,\eta)\in\mathcal{C}} \mathcal{J} = \min_{(\kappa,\eta)\in\mathcal{C}} \left\{ -\int_0^T \mathcal{F}_{\mathcal{E}}(u,v;a)dt + \frac{\gamma}{2}\int_0^a \left(\partial_x^2\kappa^2 + \partial_x^2\eta\right) dx \right\}, \tag{5.17}$$

subject to the differential equation constraint (5.4).

The first term in the objective $\mathcal{J}$ has the appearance of a running cost in time. However, the following simple calculation demonstrates that this term can instead be written as

$$\int_0^T \mathcal{F}_{\mathcal{E}}(u,v;a)dt = \int_0^T \int_\infty^a \partial_x \mathcal{F}_{\mathcal{E}} dt dx = \int_a^\infty \int_0^T \partial_t \mathcal{E} dt dx = \int_a^\infty \mathcal{E}(x,T)dx, \tag{5.18}$$

by the fundamental theorem of calculus, Fubini's theorem, and conservation law (5.15). In this sense, the term which promotes a greater energy flux into the constant grating portion can be written as a running cost of terminal energy in space. The second term in objective $\mathcal{J}$ is the usual Tikhonoff regularization, yet appropriately taken over space. The inclusion of this regularization is motivated by its successful application throughout the earlier chapters of this dissertation.

In order to solve Problem (5.17), we again employ the use of the hybrid optimization method of Section 2.4. Since the line search portion of the hybrid method requires computations of the gradient, we formally derive the

Euler-Lagrange equations in Appendix B.1. We find

$$i\partial_t\lambda + i\partial_x\lambda + \left(\eta + 2\mathcal{E} + u^{\dagger 2}\right)\lambda + \left(\kappa + 4v^\dagger \Re\{u\}\right)\mu = 0, \tag{5.19}$$

$$i\partial_t\mu - i\partial_x\mu + \left(\eta + 2\mathcal{E} + v^{\dagger 2}\right)\mu + \left(\kappa + 4u^\dagger \Re\{v\}\right)\lambda = 0, \tag{5.20}$$

$$\lambda(x,T) = 2iH(x-a)\Re\left\{u(x,T)\right\}, \tag{5.21}$$

$$\mu(x,T) = 2iH(x-a)\Re\left\{v(x,T)\right\}, \tag{5.22}$$

$$\gamma\partial_x^2\kappa = \int_0^T \Re\left\{\lambda^\dagger v + \mu^\dagger u\right\} dt, \tag{5.23}$$

$$\gamma\partial_x^2\eta = \int_0^T \Re\left\{\lambda^\dagger u + \mu^\dagger v\right\} dt, \tag{5.24}$$

where $H(x-a)$ is Heaviside's function. As usual, we find two costate equations, Equations (5.19) and (5.20), which are evolved backward in time from the terminal conditions, Equations (5.21) and (5.22). We use the numerical method detailed in Appendix A.2 to solve these costate equations. Equations (5.23) and (5.24) are used in the computation of control gradients as required by Algorithm (3). Computations of the gradient are performed in the space $\dot{H}_0^1([0,a])$, and we use the Chebyshev differentiation matrices (4.14) in order to solve the resulting boundary value problem.

5.4 Numerical Results

We now present the results of using the hybrid optimization method of Section 2.4 on optimal control problem (5.17). We relax the constraint that the optimization is performed solely over $x \in [0,a]$, which is used as notational convenience, and instead allow the domain $x \in [x_0,a]$, where $a > x_0 > 0$. In all simulations, we find the Tikhonoff parameter γ on the order of 10^{-6} to be satisfactory. We use differential evolution parameters $N_{\text{pop}} = 50,\ F = 0.8,\ C_R = 0.9$, and $N_{\max} = 30$ as required by Algorithm (2).

The 12 mode CRAB ansatz we use throughout this section is

$$\kappa_r(x) = (\kappa_0 - \kappa_{\mathrm{RH}}(x_0)) \sum_{j=1}^{12} \frac{r_\kappa}{j^2} \sin\left(j\pi \frac{x - x_0}{a - x_0}\right) + (\kappa_0 - \kappa_{\mathrm{RH}}(x_0)) \frac{x - x_0}{a - x_0} + \kappa(x_0), \tag{5.25a}$$

$$\eta_r(x) = \frac{\kappa_0}{100} \sum_{j=1}^{12} \frac{r_\eta}{j^2} \sin\left(j\pi \frac{x - x_0}{a - x_0}\right), \tag{5.25b}$$

on the optimization domain $x \in [x_0, a]$, where r_κ and r_η are random variables drawn uniformly from $[-1, 1]$, κ_{RH} is a Rosenthal and Horowitz apodization (5.11) with free parameters (λ, ζ), and $\kappa_0 = 2\mathrm{mm}^{-1}$, consistent with the constant grating portion of κ_{RH}. From experience, we find that chirp functions which are about two orders of magnitude smaller than κ_0 perform well; this is why we include the factor of 100 in the CRAB ansatz for η. All other conventions regarding numerical simulations are consistent with those used so far throughout this chapter.

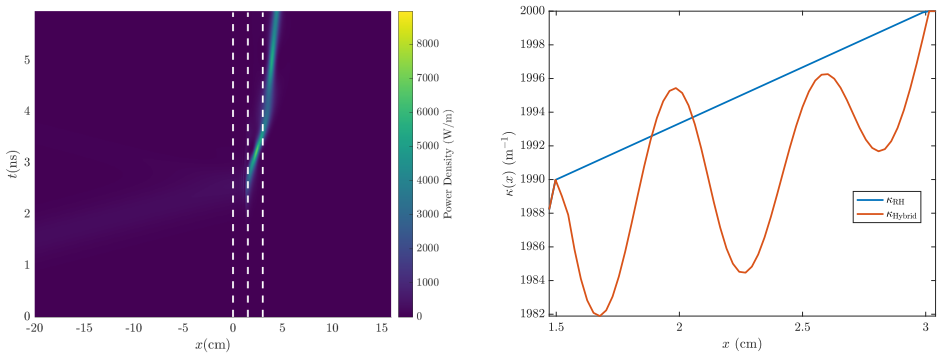

(a) (b)

Figure 5.9 The result of using the hybrid method to find more efficient apodization functions κ nearby the $(\lambda, \zeta)_{\mathrm{RH}}$ apodization. 72.9% of the incident light is now coupled into the grating. The conventions of Panel (a) are consistent with those of Figure 5.3.

Motivated by the results of the brute force search shown in Figure 5.8, we begin by searching for nearby grating functions that perform optimally relative to the Rosenthal and Horwitz apodizer (5.11), which successfully couples about 68% of the energy of the signalling data into the grating. We set $x_0 = 1.5\mathrm{cm}$

and $a = 3$cm consistent with the apodization parameters $(\lambda, \zeta)_{\text{RH}}$, and use the associated Rosenthal and Hororwitz function everywhere else outside $[x_0, a]$.

Without taking the chirp η into account, the hybrid method finds an apodization function which couples 72.9% of the incident light into the grating, and we show this in Figure 5.9. We also show, in Figure 5.10, that by performing an optimization over the domain consistent with the optimal parameters $(\lambda, \zeta)_*$ shown in Figure 5.8, we find an apodization function which couples 74.1% of the incident light.

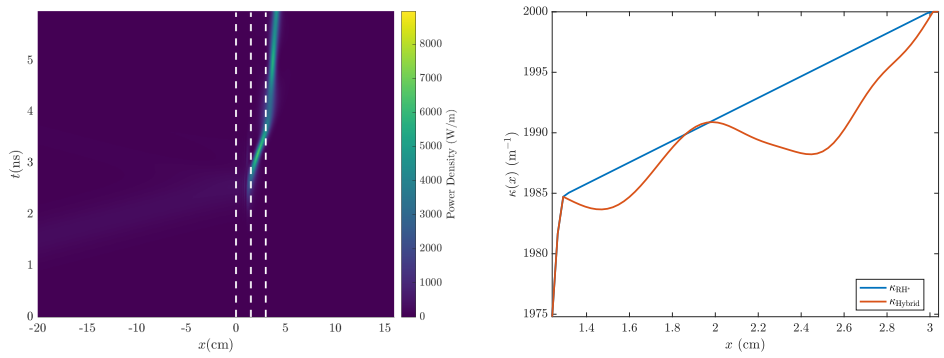

(a) (b)

Figure 5.10 The result of using the hybrid method to find more efficient apodization functions κ which are nearby the $(\lambda, \zeta)_*$ apodization. 74.1% of the incident light is now coupled into the grating.

By keeping the optimization domain consistent with the parameters $(\lambda, \zeta)_*$, yet including a chirp in the optimization, we show, in Figure 5.11, grating functions which couple 77.7% of the incident light. From the optimal apodization functions, shown in Figures 5.9–5.11, we observe a clear pattern: the nearby efficient apodization functions have a large negative gradient to the right of the optimization boundary point x_0.

For this reason, we slightly extend the width of the optimization domain to $[1.19, 3.4]$cm, and perform the search again. We show, in Figure 5.12, grating functions which now successfully couple 82.6% of the incident light. The extension of the domain is chosen judiciously. We extend the domain so that the entire grating structure is still reasonably within some technological constraint, e.g.,

15% larger than the total size of the Rosenthal and Horowitz apodization region. The left endpoint x_0 is chosen ad hoc until we find an optimal grating function κ such that $\kappa'(x_0) > 0$.

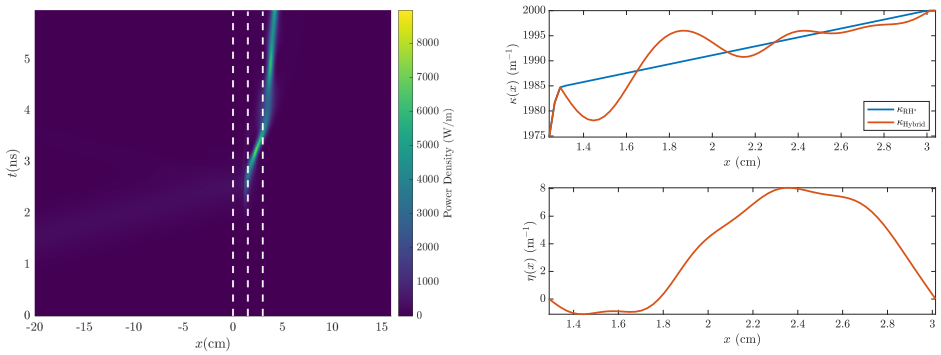

(a) (b)

Figure 5.11 The result of including a chirp in the search for efficient grating functions near the $(\lambda, \zeta)_*$ apodization. 77.7% of the incident light is now coupled into the grating.

We also show, in Figure 5.12, the resulting spatial and temporal power spectra. We learn that allowing the optimization domain to be slightly wider, we can make significant gains by slightly increasing the spectral power exchange time between the out-gap coupled modes and the in-gap one. We also find that the resulting in-gap soliton has a group velocity with a magnitude 0.53% that of light speed. We emphasize this unintended, yet fortuitous improvement in the slow down of the coupled light against the result of the original $(\lambda, \zeta)_{\mathrm{RH}}$ apodization visually in Figure 5.13.

Changing the width of the optimization domain introduces an unsystematic aspect to our method. Therefore, we turn toward searching for optimal grating functions on the original domain $x \in [0, 3]$cm. We first perform a gradient descent, using Algorithm (3), downhill from the $(\lambda, \zeta)_{\mathrm{RH}}$ apodization function to find a grating structure that is locally optimal over the entire the admissible space $\mathcal{C}$. We find grating functions which are 78.2% efficient and show the results in Figure 5.14.

The final result we show, in Figure 5.15, is one which does not involve the Rosenthal and Horowitz class of apodization functions (5.11). Remarkably, our

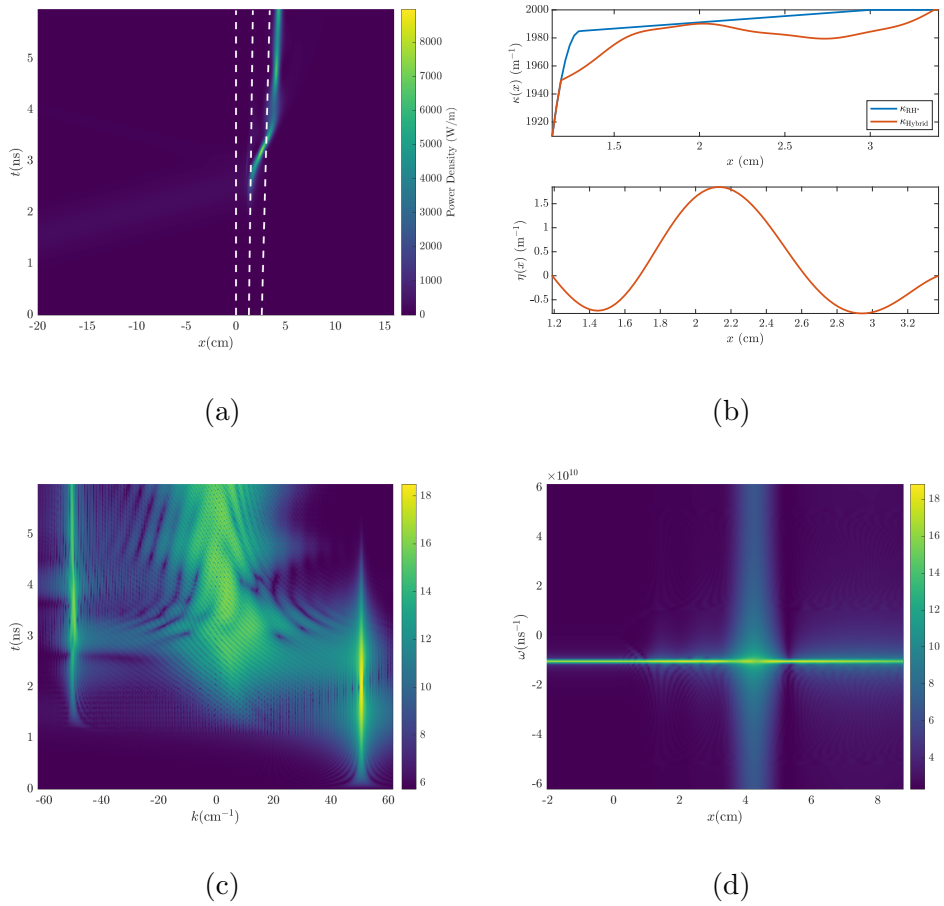

Figure 5.12 The result of relaxing the optimization domain to be slightly wider, i.e., $x_0 = 1.19$cm and $a = 3.4$cm. Panel (c) shows the computed spatial power spectrum, while Panel (d) shows the computed temporal power spectrum. The spectral densities show a greater coupling of light into the band gap than that of Figures 5.6 and 5.7.

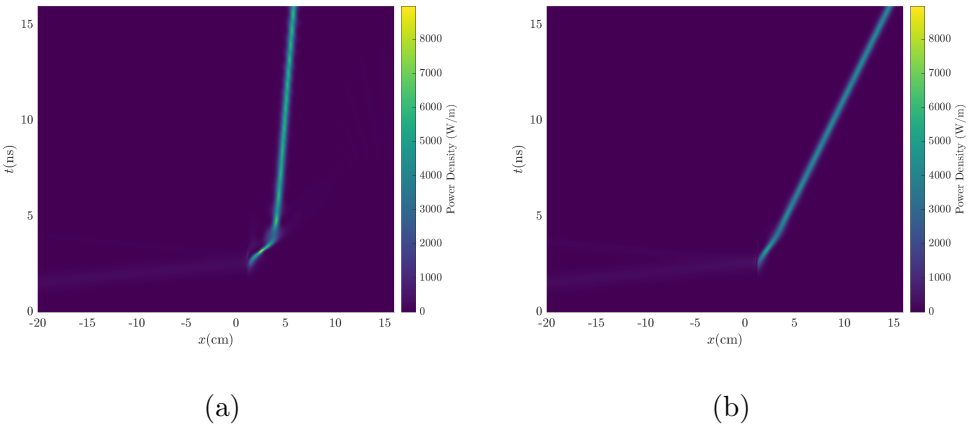

Figure 5.13 A long time simulation consistent with the results of Figure 5.12. Panel (a) is the result of the locally optimally grating structure, while Panel (b) is the result of the $(\lambda, \zeta)_{\mathrm{RH}}$ apodization.

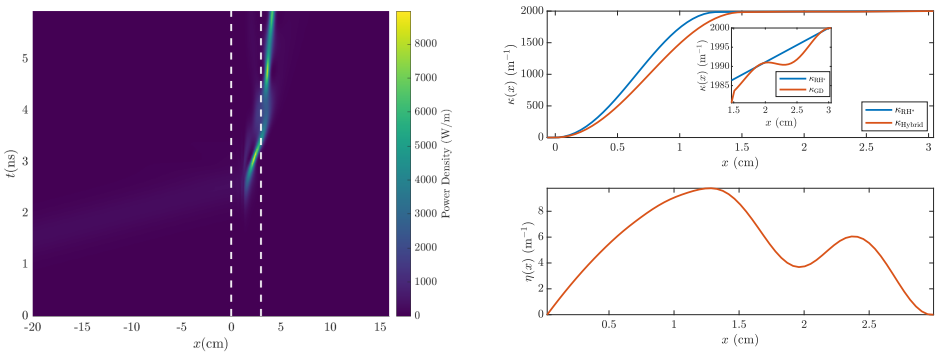

(a) (b)

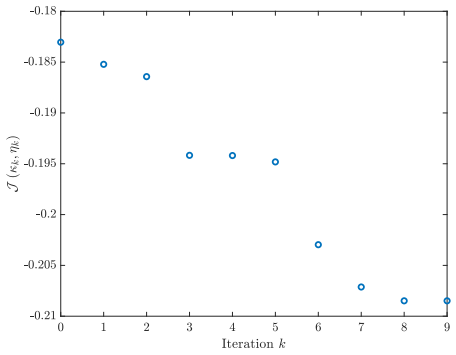

(c)

Figure 5.14 The result of using the gradient descent method (3) in order to find locally optimal grating functions downhill from the $(\lambda, \zeta)_*$ apodization. 78.2% of the incident light is coupled into the grating. Panel (c) shows the local convergence of the gradient descent on the objective functional (5.17).

best grating structure, which is only 66% efficient, is similar in profile to the Rosenthal and Horowitz shape near the ends of the boundary. Since the resulting grating structure is found after 12 hours of computational time on a personal computer, the value of Rosenthal and Horowitz's intuition behind their design should not be understated.

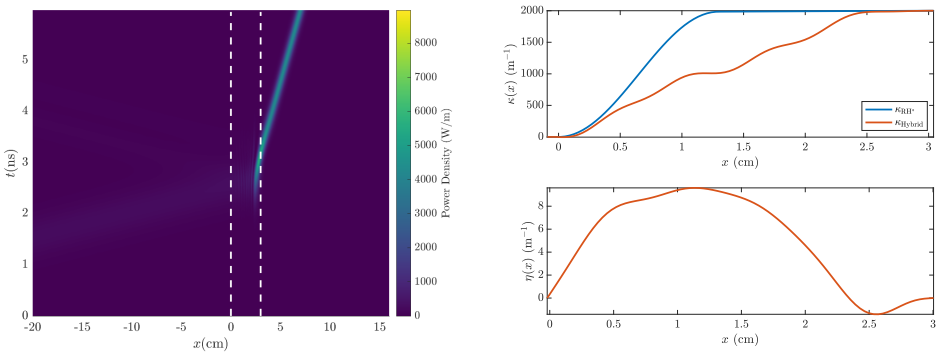

(a) (b)

Figure 5.15 The result of using the hybrid method with the optimization domain $x \in [0, 3]$cm. The efficiency of the grating structure is comparable to that of the $(\lambda, \zeta)_{\mathrm{RH}}$ apodization function at around 66%.

5.5 Concluding Remarks

In this chapter, we formulate a simple and physically motivated optimal control problem aimed at efficiently coupling light into an FBG. By employing numerical optimization methods widely used in the quantum control literature, we demonstrate the viability of optimal control in the design of fiber Bragg gratings which act as efficient compressors and pulse-delayers. We optimize previously reported designs, and provide guidance on how to explore the space of possible designs. Consistent with the work of previous chapters, the methodology used here can be applied, with suitable modifications, to other problems constrained by dispersive equations.

In addition, by considering the chirp of the grating as part of the design, we see an improvement in both the transmission of the light and the effectiveness of the grating as a pulse-delayer. Moreover, we find the globally optimal apodization

functions for this problem are most likely ones which have features similar to the Rosenthal and Horowitz design. We also observe that in cases where we see significant gains in the transmission of light into the fiber, we find this comes at the cost of decoherence through two possible mechanisms: radiation buildup and solitary wave fissioning.

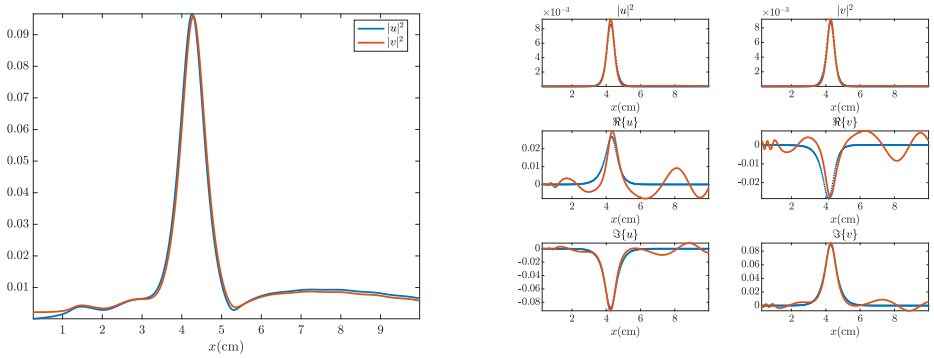

Figure 5.16 Panel (a) displays solutions of Equation (5.4) at $t = 5$ns corresponding to the optimal grating structures in Figure 5.12 and. Panel (b) shows a Bragg soliton fitting with parameters $c = -0.007$, $\theta = 31.3, \Psi_0 = 2.66$, and $T = -13071$. Evidence of solitary wave decoherence is present.

Evidence of radiation buildup is seen in the contrast between the tails of the power densities shown in Figures 5.4 and 5.5. Further evidence exists through the temporal power spectra at spatial points well beyond the apodization region in Figure 5.12 and the associated Bragg soliton fits in Figure 5.16. We find that the grating structure is only 78.1% effective in terms of *coherent* energy since 94.5% of the total belongs to the Bragg soliton rendering this result to be less impressive.

Some decoherence may be due to solitary wave fissioning, although we do not observe clear evidence of its presence here. Even if evidence of the onset of fissioning is unconvincing, its presence is certainly possible and well-understood. Fissioning, as a culpable mechanism of decoherence, has been well-studied over the past few decades. Indeed, numerical studies by Mak and Malomed [43] demonstrate the possibilities of Bragg soliton splitting, albeit in a slightly different experimental context. Theoretical insight behind this mechanism is based on the inverse scattering formalism and the mechanism has been accounted for

in nearly-integrable versions of the Korteweg-deVries equation in work due to Zabusky and Tappert [67] and the Benjamin-Ono equation in work due to Choi [15].

We believe the numerical results of this section, in particular those of Figure 5.12, serve as an impetus for investigating the coupled-mode dynamics more thoroughly. The intention behind our studies is to gain insight into an optimization framework tailored toward maintaining coherence and fidelity in highly intense solitary waves. For these reasons, this dissertation continues forward with optimal control problems involving nearly-integrable dispersive wave equations.

CHAPTER 6

OPTIMAL CONTROL OF SOLITONS IN NEARLY-INTEGRABLE SETTINGS

6.1 Introduction

In this chapter, we propose a method for designing locally inhomogeneous media intended to coherently transform spatial solitons. In the homogeneous setting, the evolution equations are integrable, i.e., they are exactly solvable and possess an infinite number of conservation laws. By nearly-integrable, we mean the evolution equations would be integrable in the absence of these localized inhomogenieties. The optimal control problem is formulated in terms of a certain time-dependent spectrum associated with the inverse scattering formalism. We provide a numerical demonstration of the optimal control problem's merit for when the constraining dynamics are given by the Korteweg-deVries equation.

6.2 Canonical Examples of Nearly-Integrable Systems

Many nonlinear wave equations are known to support solitons as exact solutions. In fact, there are an infinite number of integrable PDE which can be constructed via the so-called AKNS hierarchy [52]. Despite the presence of this vast zoo of solitons and integrable equations, certain equations, like the Korteweg deVries (KdV) equation, nonlinear Schrödinger (NLS) equation, and the Toda lattice, recur throughout many textbooks and serve as great educational and historical gateways to the beautiful mathematics of integrable systems. Many of these integrable equations serve as model problems in several different physical situations. Indeed, integrable nonlinear wave equations almost universally appear as solvability conditions when seeking uniform approximations to difficult wave propagation problems such as those governed by Maxwell's equations, the Navier-Stokes equation, or even continuum limits of discrete anharmonic oscillators.

As a model problem, consider the perturbed KdV equation as it appears in the context of surface gravity waves:

$$\partial_t q + 6q\partial_x q + \partial_x^3 q + \Gamma(t)q = 0, \tag{6.1}$$

where t is a slowly varying spatial scale, x is the reference frame coordinate of a propagating unidirectional solitary wave, $\Gamma(t) = \frac{9}{4}\partial_t \log D$, $D(t)$ is proportional to the slowly varying depth below the fluid surface, and $q(x,t)$ is proportional to the leading order contribution to the fluid velocity potential. Equation (6.1) appears as a solvability condition for free-surface dynamics constrained by ideal fluid flow; see [52] for a complete derivation and more detailed account of the relevant physics.

Consider an initial soliton of the form

$$q(x,0) = \alpha^2 \operatorname{sech}^2 \frac{\alpha x}{2}, \tag{6.2}$$

with $\alpha > 0$, which exactly solves Equation (6.1) in the absence of topography gradients $\partial_t D$. We show, in Figure 6.1, a numerical simulation of Equation (6.1) with initial condition (6.2) and sigmoidally-shaped topography D. The initial soliton fissions into four solitons as it interacts with the topography. Numerical evidence that the fissioned solitary waves are indeed solitons is captured by the expected KdV soliton-soliton interaction: solitons exchange every one of their conserved quantities upon colliding which manifests a phase shift as the only directly observable effect. The number of solitons which can fission from the initial soliton is accounted for by work due to Zabusky [67] and only depends on the relative change in depth across the shelves of the topography and the parameter α. This problem serves as the canonical example of soliton fissioning; one of two generic features of nearly-integrable dynamics.

Another expected feature of nearly-integrable dynamics is the shedding or buildup of radiation. Consider the following perturbed NLS equation

$$i\psi_t + \frac{1}{2}\partial_x^2 \psi + |\psi|^2 \psi + i\partial_t \log D(t)\psi = 0, \tag{6.3}$$

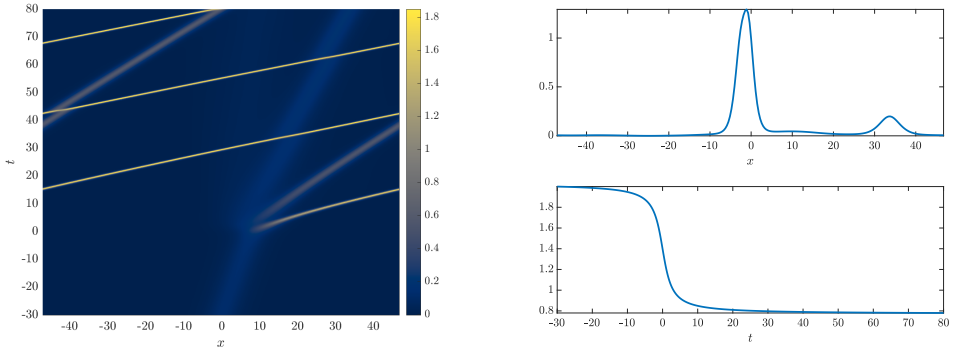

(a) (b)

Figure 6.1 Numerical solution of equation (6.1) in Panel (a) using the split-step Fourier, integrating factor technique with periodic boundary conditions detailed in Appendix A.3. Evidence soliton fissioning is seen through the phase shift of interacting solitons as they wrap around the periodic domain. The initial condition (6.2) has $\alpha = 1/2$. Panel (b) shows the final computed solution q, top, and the topography $D(t)$, bottom.

with 2-parameter family of initial soliton conditions

$$\psi(x,0) = 2\lambda \operatorname{sech}(2\lambda x) e^{icx} e^{\frac{i\pi}{4}}, \tag{6.4}$$

as a model system. We show, in Figure 6.2, the resulting dynamics are somewhat complex where we see a mix of soliton fissioning and radiation shedding in the tails. The purpose of this numerical experiment is to show, in general, it can be quite difficult to resolve the main soliton after it has been perturbed, unlike the numerical experiment of Figure 6.1.

6.3 A Soliton Control Strategy and its Optimality Conditions

The aim of building a soliton-specific control strategy is to avoid losses of coherence due to either fissioning or radiation shown in Figures 6.1 and 6.2. To this end, we seek a clear representation of the mass content present in the intended coherent soliton. Indeed, there is a well-known formula for the KdV equation, called the trace formula, which fulfills this desire:

$$\int_{-\infty}^{\infty} q dx = 4 \sum_{k=1}^{N} \eta_k + \frac{2}{\pi} \int_0^{\infty} \ln\left(1 - |R(\xi)|^2\right) d\xi. \tag{6.5}$$

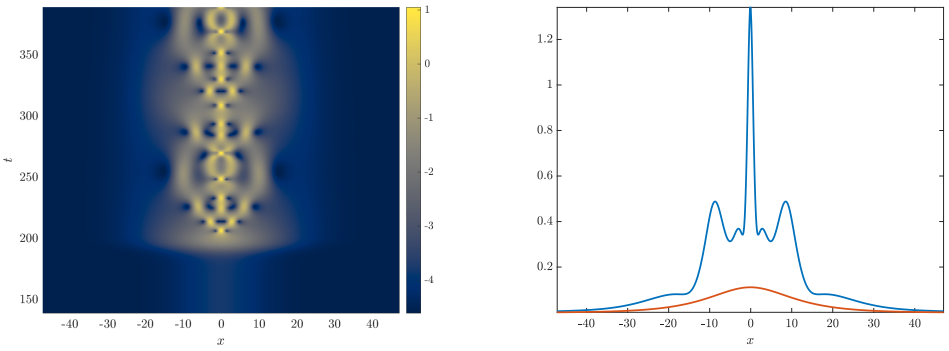

(a) (b)

Figure 6.2 Panel (a) shows a numerical solution of the NLS equation (6.3) using the split-step Fourier method of Appendix A.1 and periodic boundary conditions. Here, $\lambda = 0.5$, $c = 0.01$ are used in initial condition (6.4). Panel (b) shows the presence of soliton fissioning and radiation buildup.

A derivation of this formula and a primer on the inverse scattering formalism for the KdV equation are provided in Appendix C. Trace formulae such as (6.5) generally exist for integrable nonlinear wave equations [52], so the methods developed here are applicable to other problems involving the coherent control of solitons.

The left-hand side of Equation (6.5) is the total mass of solutions to Equation (6.1) and is not conserved due to the presence of the topography profile D. In fact, it is straightforward to show that by integrating Equation (6.1) by parts over $\mathbb{R}$, the local mass changes through

$$\int_{\mathbb{R}} q(x,t)dx = \frac{\alpha^2}{2}\left(\frac{D(0)}{D(t)}\right)^{\frac{9}{4}} \int_{\mathbb{R}} \operatorname{sech}^2 \frac{\alpha x}{2} dx = 2\alpha \left(\frac{D(0)}{D(t)}\right)^{\frac{9}{4}} := \beta D^{-\frac{9}{4}}. \tag{6.6}$$

The first N terms on the right-hand side of Equation (6.5) correspond to the N bound states of the eigenvalue problem,

$$\partial_x^2 \psi + \left(\zeta^2 + q(x,t)\right)\psi = 0, \tag{6.7}$$

where $\zeta = i\eta$, associated with the KdV equation through the inverse scattering transform. The singular values η_k account for the mass of each soliton. The last term on the right-hand side of Equation (6.1) accounts for the radiation buildup

through the continuous spectrum of the eigenvalue problem (6.7) and is the Fresnel reflection coefficient of q.

We show, in Figure 6.3, the computed differences among the various terms in the trace formula (6.5). We see that, indeed, the trace formula is a computationally accurate way of accounting for the mass of each fissioned soliton, even if each of the solitons is distorted by their mutual interactions at a given moment.

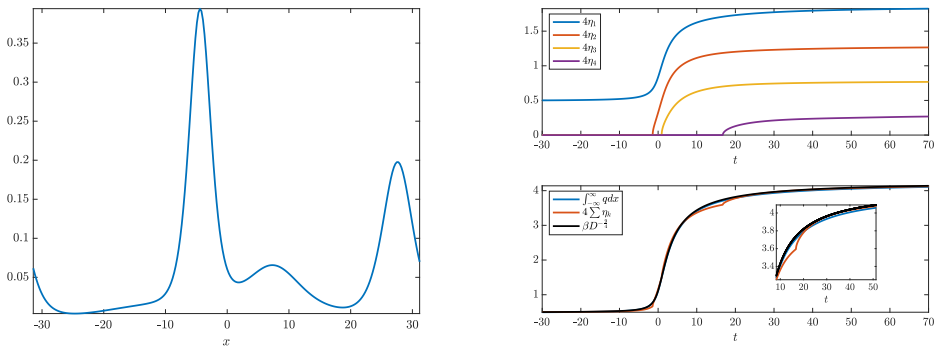

(a) (b)

Figure 6.3 Demonstration of the accuracy of the trace formula (6.5). Panel (a) shows the computed solution of Equation (6.1) at $t = 70$ with periodic boundary conditions and initial condition (6.2) with $\alpha = \frac{1}{4}$. Panel (b) shows the scaled singular values η_k, computed by the spectral method used to solve the inverse scattering problem (4.17). The bottom portion compares a direct computation of the mass via the periodic trapezoidal rule, the sum of the scaled singular values, and the mass law (6.6).

Now, consider the perturbed KdV equation (6.1) and its associated trace formula (6.5). The physical intuition we gain from the trace formula (6.5) is that as a soliton evolves in an inhomogeneous medium, the soliton can only shed mass due to two mechanisms: fissioning and radiation buildup. Since we would like to maximize the mass in the main soliton, evolved from the soliton initial condition (6.2), and assuming q is strictly real so that the Schrödinger operator in Equation (6.7) is self-adjoint, it's clear we're interested in minimizing

$$\Lambda_{\mathcal{J}} = \int_{-\infty}^{\infty} q dx - 4\eta_1. \tag{6.8}$$

Therefore, a natural optimal control problem to study is

$$\inf_{D\in\mathcal{D}} \mathcal{J} = \frac{1}{2} \inf_{D\in\mathcal{D}} \int_0^T \left(\Lambda_{\mathcal{J}}^2 + \gamma \partial_t D^2\right) dt \tag{6.9}$$

subject to the perturbed KdV equation (6.1) and intial soliton condition (6.2). The use of the admissible class

$$\mathcal{D} = \left\{ D \in H^1\left([0,T]\right) : D(0) = D_0, D(T) = D_T, D_0 > D_T > 0 \right\}$$

ensures the mass, given by Equation (6.6) does not grow arbitrarily large.

The usual Tikhonov term has been introduced to regularize the objective to ensure well-posedness of the control problem. We choose to use $\Lambda_{\mathcal{J}}$ in a running cost, instead of a terminal cost, for two reasons: it is far easier to prove existence of minimizers and simpler to derive the necessary optimality conditions. We show, in Appendix B.3, the nature of the difficulty in using a terminal cost.

However, the drawback of using a running cost is that evaluations of $\mathcal{J}$ require a greater amount of computation time. By using a terminal cost, an evaluation of $\mathcal{J}$ requires one solve of Equation (6.1) and one solve of the eigenvalue problem (6.7) at $t = T$. By using a running cost, we must instead solve the eigenvalue problem (6.7) several times for each evaluation of $\mathcal{J}$.

In Appendix B.3, we show the necessary optimality conditions are given by

$$\partial_x^2\varphi + (q - \eta_1^2)\varphi - 2\partial_x^2\psi_1 - 2\left(\psi_1\varphi + 4\beta D^{-\frac{9}{4}}\eta_1^{-1}\right)\left(\partial_x^2\psi_1 + (q-\eta_1^2)\psi_1\right) = 0, \tag{6.10}$$

$$\gamma\partial_t^2 D - \frac{9}{4}\partial_t\frac{pq}{D} + \frac{9}{4}D^{-2}\partial_t D + \frac{9}{4}\beta^2 D^{-\frac{11}{2}} - 9\eta_1\beta D^{-\frac{13}{4}} = 0, \tag{6.11}$$

$$\partial_t p + 6q\partial_x p + \partial_x^3 p - \Gamma(t)p - \varphi\psi_1 - \frac{1}{2}\eta_1\psi_1^2 = 0, \tag{6.12}$$

$$p(x,T) = 0, \tag{6.13}$$

where p is the adjoint state to q, φ is the adjoint state to eigenfunction ψ_1 corresponding to the singular value η_1, $\varphi \in L^2(\mathbb{R})$, and $D \in \mathcal{D}$.

6.4 A Numerical Demonstration

We now provide a demonstration of the control strategy outlined in Section 6.3. This demonstration simply serves as a proof of concept for the soliton control strategy, and a more serious undertaking of determining the efficiency of our strategy will be done when this method is applied to the problem of Chapter 5 in Chapter 7.

To this end, we use the sigmoidally shaped topography shown in Figure 6.1 as a reference. Since the optimality conditions (6.12)–(6.11) take a fair amount of commitment to solve, with the only available solution technique being a costly finite difference method, we choose to only use the CRAB method in the optimization. We leave further exploration of the optimal control problem using the GRAPE methodology as future work. Instead, we rely on a CRAB, analogous to Equation (5.25), with differential evolution parameters consistent with those used in Section 5.4.

We see, in Figure 6.4, topographies which perform more optimally than the initial topography of Figure 6.1. There is now 5% more mass in the primary soliton while the amplitude of the secondary soliton has been reduced by a factor of two. We also see, in Figure 6.5, the fissioning happens less abruptly than before. This is seen both in the solution of Equation (6.1) and the eigenfunction ψ_1 solving Equation (6.7). We note that the resemblance of the solutions of Equation (6.1) and Equation (6.7) in Figure 6.5 is reflected through the fact that the initial condition (6.2) is a Pöschl-Teller potential (4.7) with respect to the ground state eigenfunction ψ_1 which takes the form of Equation (4.8).

Although our numerical results for this section are not that enticing, it is difficult to judge the extent to which our demonstration can be optimized. We believe we thoroughly search the space of admissible topographies, corresponding to the boundary values of the initial topography in Figure 6.4, using our method. Indeed, what we see is that our numerical simulations are constrained by and verify a theoretical result due to Mei [42].

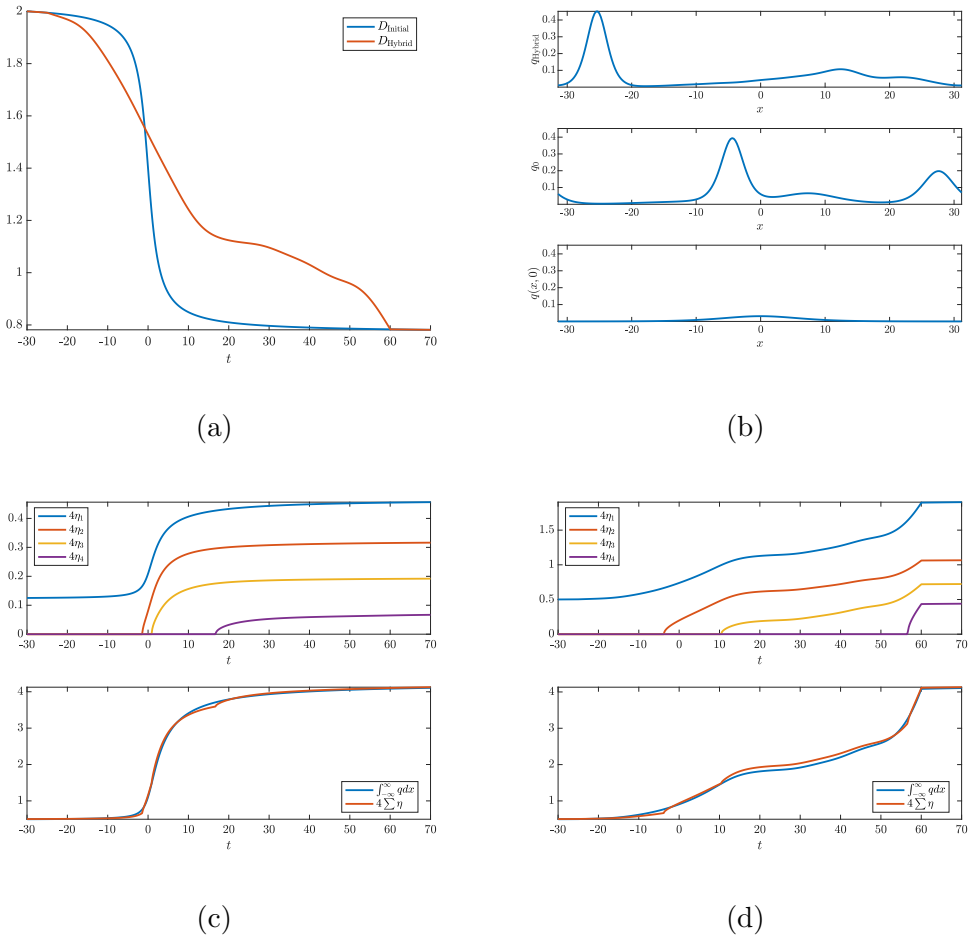

Figure 6.4 The result of using the CRAB method in order to solve the optimal control problem (6.9). Panel (a) shows the initial and resulting topographies. Panel (b) shows the resulting solutions of Equation (6.1) and the initial condition. Panels (c) and (d) show the corresponding mass decomposition via the trace formula (6.5) for the initial and optimized topographies, respectively.

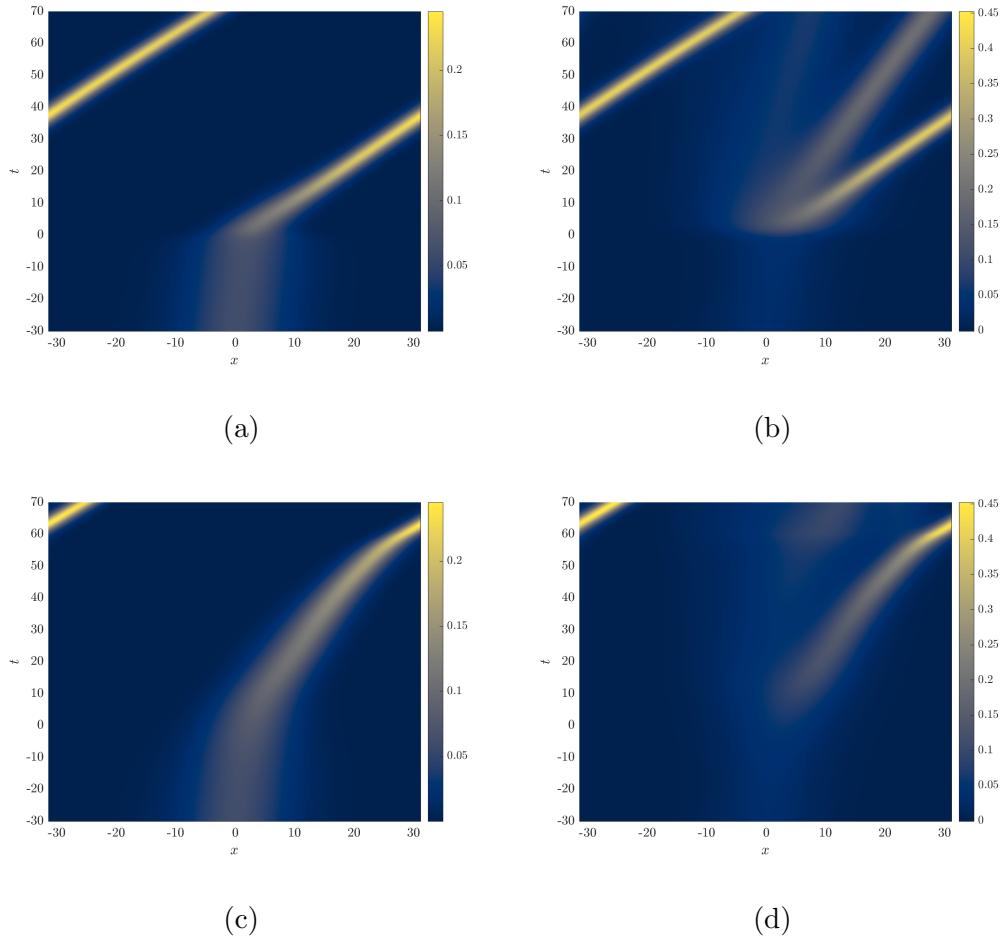

Figure 6.5 Shown here are the eigenfunctions $|\psi_1|^2$ solving Equation (6.7). Panel (a) corresponds to the numerically computed potential q, which solves Equation (6.1) with the initial topography from Figure 6.4, in Panel (b). Panel (c) corresponds to the potential q, resulting from the optimized topography shown in Figure 6.4, displayed in Panel (d).

Mei predicts that if the topography varies slowly over t, then the number of solitons that will fission is determined only by the change in depth $D(0) - D(T)$. Mei's result, in the context of our demonstration, predicts we should observe four solitons after the topographical interaction, and we see that this result is quite robust in that it also holds for topographies that transition rapidly as those shown in Figure 6.4.

We also note, going forward, our method is intended for a refinement of the results of Chapter 5. The results of Chapter 5 indicate that gaining even a few percentage points of efficiency is a difficult task. Moreover, our refinement method motivates the efficient design of FBG as a two-stage optimal control problem, similar to the strategy used for the beam combining problem of Chapter 4, where the refinement is taken over the second stage. In this way, the soliton control method creates an opportunity to use an optimal control formulation which is not otherwise available.

CHAPTER 7

DESIGNING BRAGG GRATINGS USING COHERENT SOLITON CONTROL

7.1 Intended Goal of the Chapter

When modeling BEC in Chapter 3, we learn it is a worthwhile task to seek mathematically motivated control strategies through simplifications of the constraining dynamics. In studying profile reshaping problems in Chapter 4, we learn the merit of computing optimal controls in stages. Equipped with this experience, we seek simpler models of coupled-mode wave propagation in FBGs so that the soliton-specific techniques of Chapter 6 can be employed to refine the numerical results of Chapter 5 through a two-stage optimal control problem.

We search for simpler evolution equations by using the standard method of multiple scales [7, 47]. We find, not surprisingly, the reduced model is a nearly-integrable equation of nonlinear Schrödinger-type. We show, numerically, simulated coupled-mode data can be mapped to nonlinear Schrödinger solitons in the correct frame of reference.

We then pose an optimal control strategy of the same flavor as that of Chapter 6 over the latter portion of the apodization region given by Equation (5.11). We solve the control problem with the numerical techniques of Chapter 2. Finally, we use the optimal grating structure found in the nonlinear Schrödinger regime, couple this with the optimal grating structure found through a maximization of the global full-width at half maximum over the first apodization region, and numerically solve the NLCME (5.4) with the full grating structure to verify its overall performance.

This chapter unifies the skills, knowledge, and experience gained from Chapters 2–6. In this way, the work presented here is the culmination of the work done in this dissertation.

7.2 The Nonlinear Schrödinger Regime

7.2.1 Multiple Scale Analysis

Recall the apodization function (5.11) varies slowly in x over its second apodization region. In addition, we see that the group velocity v of the excited in-gap soliton shown in Figure 5.8 is, to good approximation, constant. By investigating the dynamics in a frame of reference which moves at the velocity v, we expect to find simpler evolution laws than that of Equations (5.4) in the original coordinates x and t.

In order to find the frame of reference which moves with the group velocity v and the evolution law, let us define the small parameter

$$\varepsilon := \sqrt{\frac{\max_x \partial_x \kappa}{\max_{x,t} \{|u|, |v|\}}}. \tag{7.1}$$

This parameter is, indeed, small for the simulation shown in Figure 5.8, and is about two orders of magnitude smaller than the scale of the apodization function κ. We assume the grating structures vary very slowly, i.e., $\kappa = \kappa(\varepsilon^2 x)$ and $\eta = \eta(\varepsilon^2 x)$. Furthermore, assume the relevant dynamics evolve over the two time scales t and $T = \varepsilon t$, and the three length scales, x, $X = \varepsilon x$, and $\zeta = \varepsilon^2 x$. The reason for these choices in scales will become more apparent in Subsection 7.2.2.

For the purposes of a multiple-scales analysis, assume the following expansion

$$w = \varepsilon w_0 + \varepsilon^2 w_1 + \varepsilon^3 w_2 + \mathcal{O}(\varepsilon^4), \qquad w_i = \begin{pmatrix} u_i \\ v_i \end{pmatrix}, \qquad i = 0, 1, 2. \tag{7.2}$$

By substituting the multiple-scale expansion (7.2) into the NLCME (5.4), using the multiple-scale operators

$$\partial_t \to \partial_t + \varepsilon \partial_T, \tag{7.3}$$

$$\partial_x \to \partial_x + \varepsilon \partial_X + \varepsilon^2 \partial_\zeta, \tag{7.4}$$

and collecting terms in powers of ε, we find, to leading order,

$$\mathcal{L}_0 w_0 = 0, \tag{7.5}$$

where the linear operator is given by $\mathcal{L}$

$$\mathcal{L}_0 = i \begin{pmatrix} \frac{\partial}{\partial t} + \frac{\partial}{\partial x} + \eta & \kappa \\ \kappa & \frac{\partial}{\partial t} - \frac{\partial}{\partial x} + \eta \end{pmatrix}. \tag{7.6}$$

Solutions of Equation (7.6) are of the form

$$w_0 = A(X, T, \zeta)\varphi_+ e^{i\Phi}, \tag{7.7}$$

where the phase

$$\Phi = \int_0^x Q(s)ds - \Omega t, \tag{7.8}$$

is defined through the dispersion relation

$$(\Omega - \eta)^2 = \kappa^2 + Q^2. \tag{7.9}$$

The Lorentz factor embedded in this definition is denoted by $\gamma = (1 - v^2)^{-1/2}$, while the group velocity is computed through $v = \partial_Q \Omega$. The linear eigenfunction φ_+, sometimes referred to as a Bloch state [19], in the ansatz (7.7) is given by

$$\varphi_+ = \frac{1}{\sqrt{2\sqrt{Q^2 + \kappa^2}}} \begin{pmatrix} \frac{\kappa}{\sqrt{\sqrt{Q^2+\kappa^2} - Q}} \\ -\sqrt{\sqrt{Q^2 + \kappa^2} - Q} \end{pmatrix}. \tag{7.10}$$

To next order, $\mathcal{O}(\varepsilon^2)$, we find the inhomogeneous linear equation

$$\mathcal{L}_0 w_1 = -\mathcal{L}_1 w_0, \tag{7.11}$$

where the operator $\mathcal{L}_1$ is given by

$$\mathcal{L}_1 = i \begin{pmatrix} \frac{\partial}{\partial T} + \frac{\partial}{\partial X} & 0 \\ 0 & \frac{\partial}{\partial T} - \frac{\partial}{\partial X} \end{pmatrix}. \tag{7.12}$$

The inhomogeniety present on the right-hand side of Equation (7.11) introduces terms that are resonant with the spectrum of the operator $\mathcal{L}_1$. Eliminating these resonant terms, via the Fredholm alternative, gives a solvability condition: the

envelope A depends *only* on the combination of variables $X + vT$. This gives us the correct frame of reference $\xi := X + vT$ to study the coupled-mode dynamics given by Equations (5.4) through the evolution of the envelope $A(\xi, \zeta)$ present in ansatz (7.7).

Introducing the coordinate ξ renders (7.11) solvable, and we search for solutions linearly independent from the ansatz at the previous order. To this end, we use

$$w_1 = B(\xi, \zeta)\varphi_- e^{i\Phi}, \tag{7.13}$$

where the Bloch state φ_- is given by

$$\varphi_- = \frac{1}{\sqrt{2\sqrt{Q^2+\kappa^2}}} \begin{pmatrix} \sqrt{\sqrt{Q^2+\kappa^2} - Q} \\ \frac{\kappa}{\sqrt{\sqrt{Q^2+\kappa^2}-Q}} \end{pmatrix} \tag{7.14}$$

and is linearly independent from the Bloch state used in the ansatz (7.7) at order $\mathcal{O}(\varepsilon)$, as desired. By substituting w_1 into Equation (7.11), we find the envelope B can be related to A by

$$B(\xi, \zeta) = -\frac{i\partial_\xi A}{\gamma\eta + 2\gamma^2\kappa}. \tag{7.15}$$

Now, to $\mathcal{O}(\varepsilon^3)$, the nonlinear terms make an appearance, and we find that

$$\mathcal{L}_1 w_2 = -\mathcal{L}_2 w_1 - \mathcal{N}(w_0), \tag{7.16}$$

where

$$\mathcal{L}_2 = i \begin{pmatrix} \frac{\partial}{\partial\zeta} & 0 \\ 0 & \frac{\partial}{\partial\zeta} \end{pmatrix}, \qquad \mathcal{N}(w_0) = \begin{pmatrix} \left(|u_0|^2 + 2|v_0|^2\right) u_0 \\ \left(2|u_0|^2 + |v_0|^2\right) v_0 \end{pmatrix}. \tag{7.17}$$

Assuming the ansatz at this order

$$u_2 = C(\xi, \zeta)\varphi_- e^{i\Phi}, \quad v_2 = C(\xi, \zeta)\varphi_- e^{i\Phi}, \tag{7.18}$$

and suppressing resonant terms, once again via the Fredholm alternative, we find the solvability condition on $C(\xi, \zeta)$ is such that

$$C(\xi,\zeta) = \frac{i}{\eta + 2\gamma\kappa}\left(\partial_\xi B - \gamma(1-v)\partial_\zeta A + \frac{i\gamma}{2}\left(v^2+2v-3\right)|A|^2 A\right). \tag{7.19}$$

Substituting (7.15) and (7.19) into equations (7.16), we find the the envelope $A(\xi, \zeta)$ satisfies the following nonlinear-Schrödinger equation (NLSE):

$$i\partial_\zeta A = -\frac{\beta}{2}\partial_\xi^2 A + \Gamma|A|^2 A, \tag{7.20}$$

where the ζ dependent coefficients $\beta(\zeta)$ and $\Gamma(\zeta)$ are given by

$$\beta(\zeta) = \frac{2}{\gamma^2 v\left(\eta + 2\gamma\kappa\right)}, \tag{7.21}$$

$$\Gamma(\zeta) = \frac{(3-v^2)}{2v}. \tag{7.22}$$

Here, the ζ dependence of β and Γ is reflected through the ζ dependence of the group velocity v, the chirp η, the apodization strength κ, and v-dependent Lorentz factor γ. We also note that an equation of this type is not entirely new. Indeed, for the chirpless case $\eta \equiv 0$, an identical equation is derived by DeSterke [21].

7.2.2 Mapping the Simulated Data to Solitons

The passage toward numerically modeling coupled-mode dynamics via the model envelope equation (7.20) is through the characteristic coordinate ξ. From the various numerical simulations shown throughout Chapter 5, we observe that the excited solitary wave typically travels at a near constant group velocity in the second apodization region given by Equation (5.11). By viewing the simulated data over space and time, mappping coupled-mode data onto the coordinate ξ is done by simple geometric means.

First, we search for points of maximum coupled-mode power $|u|^2 + |v|^2$. This is done by fixing time and then computing the pointwise maximum in space. We compute the best-fit curve through these maximal points, and then interpolate simulated coupled-mode data along the characteristic direction

perpendicular to this best-fit curve via MATLAB's `scatteredInterpolant`. We display these computed characteristic coordinates in Figure 7.2.2 as it relates to the coupled-mode data from Figure 5.3.

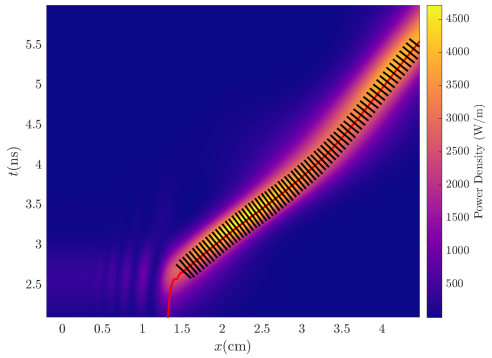

Figure 7.1 Tracking the Rosenthal and Horowitz coupled-mode wave front from Figure 5.3. The curve of maximal power is drawn in red with the computed characteristic coordinates ξ in black. Observe the group velocity in the apodization region $x \in [1.5, 3]$ cm is nearly constant which is further reflected by a constant slope in the coordinate ξ throughout this region.

We see, in Figure 7.2.2, a family of characteristic coordinates determined by the evolution parameter ζ. That is, the evolution of the characteristc coordinate ξ takes place as we move along the coordinate $\varepsilon^2 x$. In this sense, the NLSE (7.20) is an evolution equation for the coupled-mode data mapped onto the characteristic coordinate ξ. To complete the numerical mapping to the NLS regime requires the use of Ansatz (7.7) along with considerations of the natural scales present in Equation (7.20).

Consider the four-parameter family of possible soliton intitial conditons

$$\psi(\xi, 0) = 2\lambda \operatorname{sech}(2\lambda(\xi - \xi_0))e^{i(c\xi+\theta)}e^{\frac{i\pi}{4}}, \tag{7.23}$$

for the homogeneous NLSE (6.3). In order to relate this soliton to the NLSE (7.20), we rescale the envelope $A \to \sqrt[3]{\Gamma}\psi$, the characteristic coordinate $\xi \to \Gamma^{2/3}\beta^{-1/2}\xi$, and the evolution variable $\zeta \to \sqrt[3]{\Gamma}\zeta$. We then have a total of five fitting parameters to work with: the wavenumber Q, the time parameter in the phase Φ of the leading order solution (7.6), and the three NLS parameters λ, c, and θ. We show the result

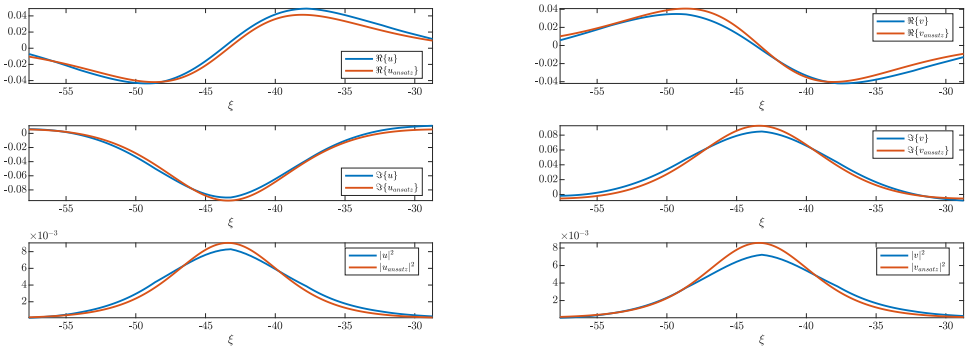

(a) (b)

Figure 7.2 Fitting the ansatz (7.6) with the NLS soliton (7.23) to the simulated data interpolated onto the characteristic coordinates in Figure 7.2.2. The fitting parameters found were roughly $\lambda = 18,\ p = 30,\ \theta = 1.8,\ \xi_0 = -43,\ Q = 0.03,$ and time shift $T = -11000$.

of a fitting performed at the point where the line $\varepsilon^{-2}\zeta = 2\text{cm}$ intersects the characteristic coordinate ξ.

We use the fitted NLS soliton, shown in Figure (7.2), as an initial conditon for the NLSE (7.20). In solving the NLSE, we see that the inhomogeniety is in the coefficient of the dispersive term $\partial_x^2 A$. Critically, this variable coefficient is a function of the evolution parameter ζ, and not the coordinate ξ. This means we can still use efficient spectral methods in order to solve, what will become, the constraining dynamics of an optimal control problem. The numerical method used to solve the NLSE (7.20) is an appropriately slight modification of the method discussed in Appendix A.1.

We show, in Figure 7.3, a sample simulation of Equation (7.20) for the Rosenthal and Horowitz grating structure (5.11) without chirp. We see the generic difficulty in using an apodized grating with increasing Bragg grating strength in the NLS regime: the soliton experiences compression at the cost of losing coherence by generating radiation.

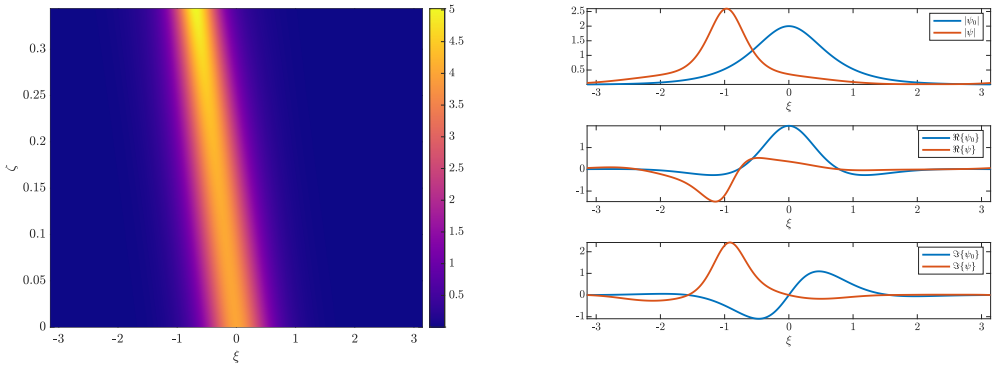

(a) (b)

Figure 7.3 Numerical solution of the NLSE (7.20) with the Rosenthal and Horowitz apodization (5.11). The parameters used for the initial soliton condition (7.23) are $\lambda = 1$, $\xi_0 = 0$, $p = 2$, $\theta = 0$, and wavenumber $Q = .03$ required by the coefficients (7.21) and (7.22).

7.3 Optimal Control Framework and the Trace Formula

In this section, we consider an optimal control strategy which makes use of the soliton-specific optimal control framework detailed in Section 6.3. Our main objective here is to refine grating structures shown in Section 5.4. As we did in Chapter 6, we use nonlinear filtering via the trace formula, but for the appropriately scaled NLSE (7.20).

Recall, the inverse scattering formalism, see Appendix C, associates a linear eigenvalue problem, called the Zakharov-Shabat system, with a potential given by an integrable nonlinear wave equation. For the homogeneous NLSE (6.3), the Zakharov-Shabat eigenvalue problem is given by

$$\partial_\xi \varphi = -i\lambda\varphi + \psi(\xi,\zeta)\phi, \tag{7.24}$$

$$\partial_\xi \phi = i\lambda\phi - \psi^\dagger(\xi,\zeta)\varphi, \tag{7.25}$$

where λ is the eigenvalue and ψ solves the NLSE (7.20) with $\beta = \Gamma = 1$.

In work due to Moore, et al. [50], it is shown the trace formula corresponding to the discrete spectrum of the operator

$$\mathcal{A} = i \begin{pmatrix} \partial_\xi & -\psi \\ -\psi^\dagger & -\partial_\xi \end{pmatrix} \tag{7.26}$$

can be used to nearly reconstruct the "soliton-like" portion of the wavefunction ψ in a computationally viable way. The formula is

$$\psi = -\sum_{k=1}^{N} \left(\frac{\varphi_k^2}{\int_{\mathbb{R}} \phi_k \varphi_k} + \frac{\phi_k^{\dagger 2}}{\int_{\mathbb{R}} \phi_k^\dagger \varphi_k^\dagger} \right) \tag{7.27}$$

where N is the cardinality of the point spectrum of ψ and each eigenfunction φ_k and ϕ_k correspond to the eigenvalue λ_k.

In order to compute the reconstruction through formula 7.27, we use a spectral collocation method due to Yang [80], which we briefly outline here. First, we truncate the spatial domain to the finite, symmetric one $\xi \in [-L/2, L/2]$. Note that this is sufficient, instead of pursuing the rescaling approach using in Subsection 4.2 since we assume reconstructed wavefunctions will have a high degree of regularity. Second, we assume the following expansions of the eigenfunctions φ and ϕ, and the potential ψ :

$$\varphi(\xi) = \sum_{n=-N}^{n=N} a_n e^{ik_n \xi}, \tag{7.28}$$

$$\phi(\xi) = \sum_{n=-N}^{n=N} b_n e^{ik_n \xi}, \tag{7.29}$$

$$\psi(\xi, \cdot) = \sum_{n=-N}^{n=N} c_n e^{ik_n \xi}, \tag{7.30}$$

where $k_n = nk_0 = \frac{2n\pi}{L}$. Substitute expansions (7.28)–(7.30) into Equations (7.24) and (7.25). The resulting eigenvalue problem is

$$i \begin{pmatrix} \mathcal{K} & \mathcal{B} \\ \mathcal{B}^\dagger & -\mathcal{K} \end{pmatrix} \begin{pmatrix} \mathbf{a} \\ \mathbf{b} \end{pmatrix} = \lambda \begin{pmatrix} \mathbf{a} \\ \mathbf{b} \end{pmatrix}, \tag{7.31}$$

where $\mathcal{B}$ is a Toeplitz matrix of size $(2N+1)\times(2N+1)$ with its first column given by $(c_0,\ c_1,\ \ldots\ c_N,\ \mathbf{0}_{1\times N})^{\mathsf{T}}$ and its first row by $(c_0,\ c_{-1},\ \ldots,\ c_{-N},\ \mathbf{0}_{1\times N})$, the operator ∂_ξ has been diagonalized into

$$\mathcal{K}_{\mathrm{ij}} = \begin{cases} -N-1+\mathrm{i}, & \mathrm{i}=\mathrm{j}, \\ 0, & \mathrm{i}\neq\mathrm{j}, \end{cases} \qquad \mathrm{i}=1,\ldots,2N+1, \tag{7.32}$$

$\mathbf{a} = (a_{-N},\ \ldots,\ a_N)^{\mathsf{T}}$, and $\mathbf{b} = (b_{-N},\ \ldots,\ b_N)^{\mathsf{T}}$. We solve the eigenvalue problem (7.31) using MATLAB's built-in function `eig`.

We test this reconstruction method and numerical procedure on the so-called Satsuma Yajima potential

$$\psi_{\mathrm{YS}}(\xi) = \alpha\,\mathrm{sech}(\xi), \tag{7.33}$$

with an amplitude of $\alpha = 1.8$, and a spatial domain of $\xi\in[-2\pi,2\pi]$ with $N = 2^{10}$ discretization points. Note that the Satsuma–Yajima potential (7.33) is not exactly an NLS soliton of the form (7.23). Despite this, we see, in Figure 7.4, that the reconstruction formula (7.27) faithfully reconstructs the bulk of the potential.

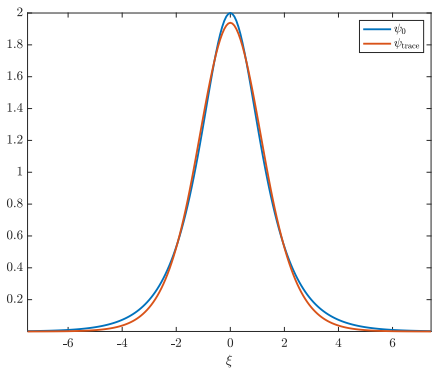

Figure 7.4 A reconstruction, via a numerical solution of the eigenvalue problem (7.31), of the nearly soliton-like portion of the Satsuma-Yajima potential (7.33).

Now equipped with a way to accurately filter radiation components from data numerically simulated by Equation (7.20), we can investigate the following optimal control problem. Let the first contribution to the discrete trace formula (7.27) be

denoted by

$$\Lambda = -\frac{\varphi_1^2}{\int_{\mathbb{R}} \phi_1 \varphi_1} - \frac{\phi_1^{\dagger 2}}{\int_{\mathbb{R}} \phi_1^\dagger \varphi_1^\dagger} \tag{7.34}$$

The optimal control problem, analogous to that of Section 6.3, we pose is

$$\min_{(\kappa,\eta)\in\mathcal{C}'} \mathcal{J} = \min_{(\kappa,\eta)\in\mathcal{C}'} \left\{ \int_{\mathbb{R}} d\xi \left(|\psi|^2 - |\Lambda|^2 \right) \Big|_{\zeta=\zeta_1} + \frac{\gamma}{2} \int_{\zeta_0}^{\zeta_1} \left(\partial_\zeta \kappa^2 + \partial_\zeta \eta^2 \right) d\zeta \right\}, \tag{7.35}$$

where $\mathcal{C}'$ is an admissible class of grating functions given by

$$\mathcal{C}' = \left\{ \kappa, \eta \in H^1\left([\zeta_0, \zeta_T]\right) : \kappa(\zeta_0) = \kappa_0,\ \kappa(\zeta_T) = \kappa_T,\ \eta(\zeta_0) = \eta_0,\ \eta(\zeta_T) = \eta_T \right\}, \tag{7.36}$$

s and where ζ_0 and ζ_1 correspond to the shallow apodization region we are interested in optimizing over. Note that the prescribed boundary conditions in the definition of the class C' are such that the grating structure across both apodization regions is continuous. Deriving the optimality conditions for optimal control problem is similar to procedure outlined in Appendix B.3. In addition, since numerically approximating the gradient of the functional $\mathcal{J}$ is somewhat difficult to implement, we choose to rely solely on the CRAB method in the numerical optimization.

7.4 Numerical Results

We present here the result of using the optimal control problem on refining the Rosenthal and Horowitz apodization function (5.11), and leave future computational investigations with other grating structures and apodization domains as the subject of future work. In Figure 7.5, we show the numerical solution of Equation (7.20) from the Rosenthal and Horowitz apodization function (5.11) and a grating function resulting from an optimization over the CRAB

$$\kappa_r(\zeta) = (\kappa_T - \kappa_0) \sum_{j=1}^{10} \frac{r_\kappa}{j^2} \sin\left(j\pi \frac{\zeta - \zeta_0}{\zeta_T - \zeta_0} \right) + (\kappa_T - \kappa_0) \frac{\zeta - \zeta_0}{\zeta_T - \zeta_0} + \kappa_0, \tag{7.37}$$

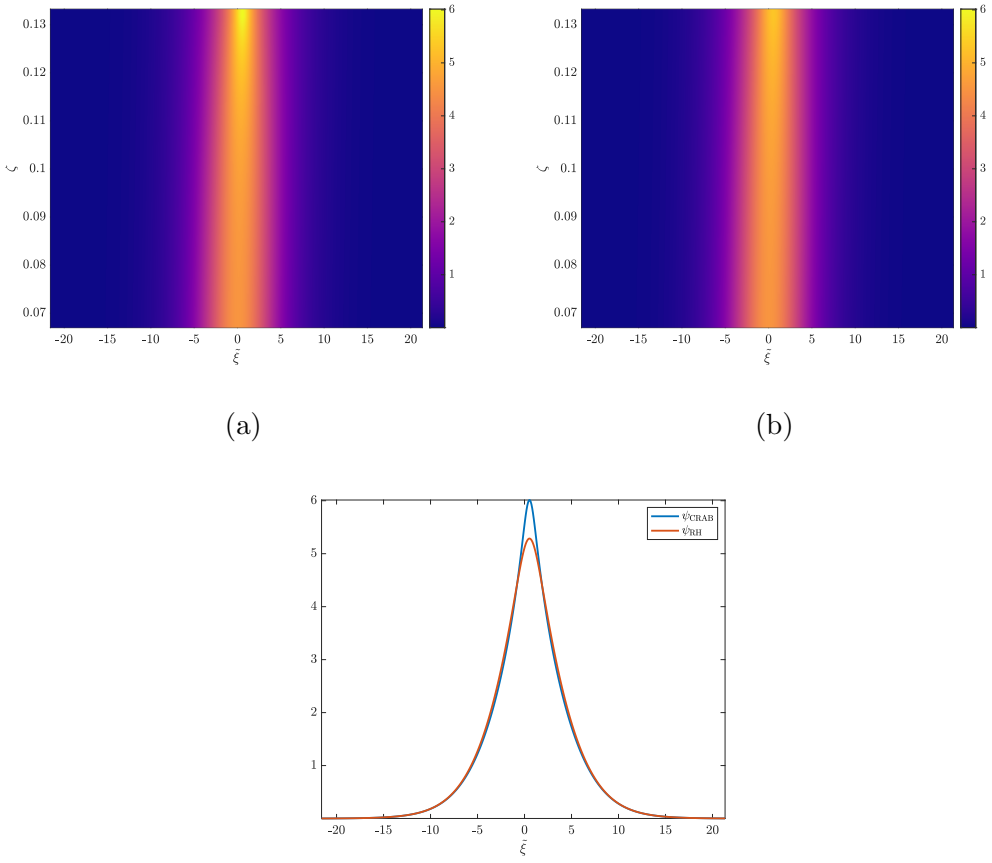

Figure 7.5 The result of using the CRAB method, with ansatz (7.37), in order to solve the optimal control problem (7.3). Panel (a) shows the solution of Equation (7.20) with the a more optimal grating function than the Rosenthal Horowitz grating (5.11) used to generate Panel (b). Panel (c) shows the corresponding final computed solutions at $\zeta = \zeta_T$. The coordinate $\tilde{\xi}$ is the shifted coordinate $\xi - \xi_0$ where ξ_0 is defined through Equation (7.23).

The DE parameters used are the same as those in Subsection 6.4. We see that more compression has been achieved without the excitation of more radiation.

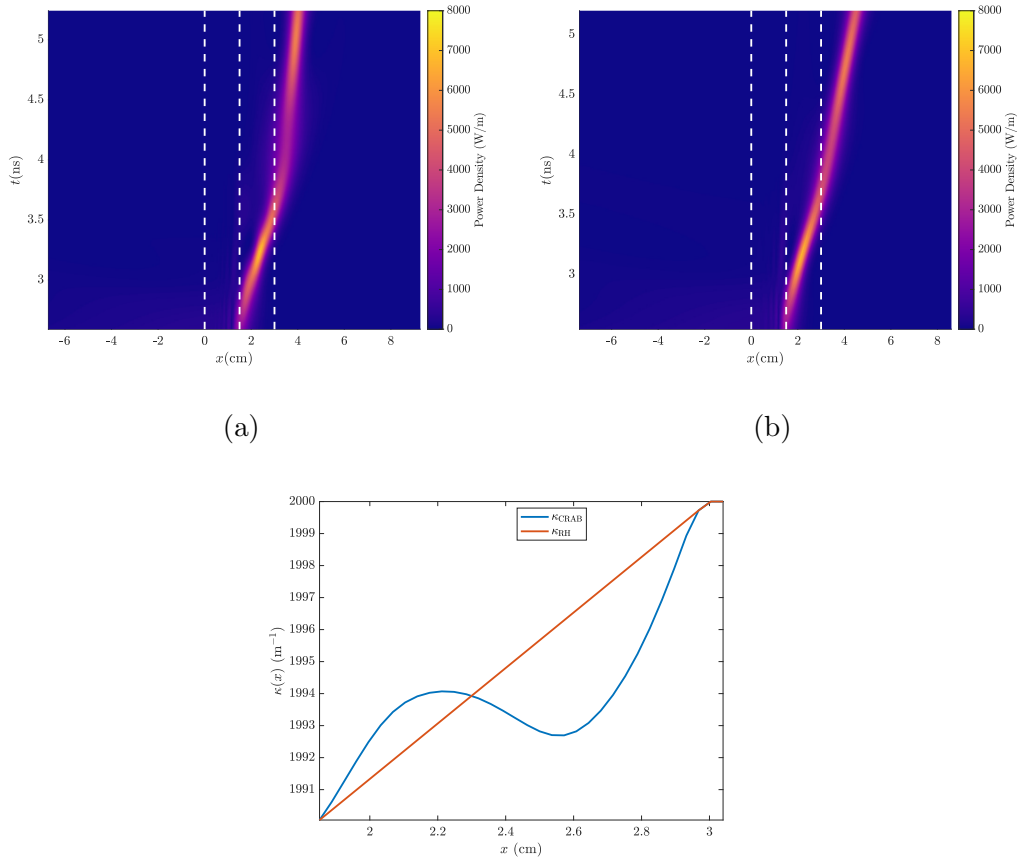

Figure 7.6 The result of using the optimal grating structure, shown in Panel (c), to solve the NLCME (5.4). More energy is coupled into the constant grating in Panel (a) than is done by the resulting Rosenthal and Horowitz power density shown in Panel (b).

In Figure 7.6, we show the optimal grating function used to generate Figure 7.5 in the NLCME regime, while also showing the resulting solution of Equations (5.4). We see that more energy is coupled into the constant grating than before. The total energy coupled into the grating is about 74%, yet, we see that there is still a significant excitation of radiation in Figure 7.7, where the energy of the Bragg soliton is only about 70%.

We learn that although in the NLS regime less radiation is excited and the resulting Bragg soliton has a stronger power density, the control objective (7.3)

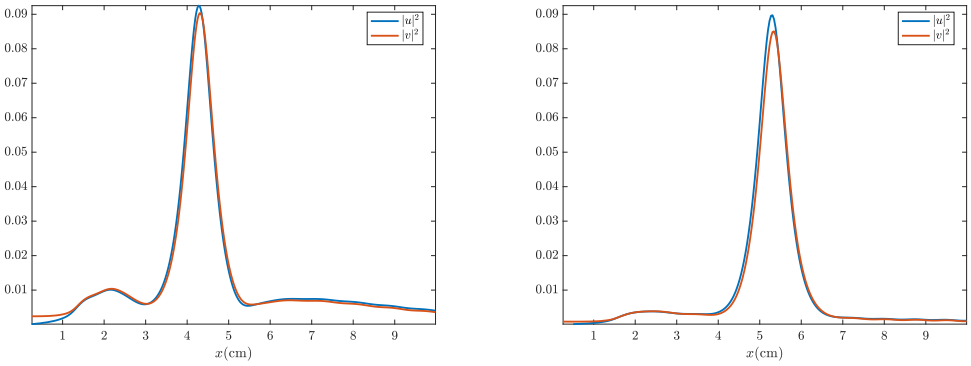

(a) (b)

Figure 7.7 Panel (a) shows the coupled-modes, in absolute value squared, resulting from the solution of the soliton control problem (7.3) at $t = 6$ns, while Panel (b) shows the resulting coupled-modes from the Rosenthal and Horowitz apodization (5.11).

fails to suppress further excitation of the radiation once radiation has already been coupled into the constant grating. For this reason, careful investigations of how to more effectively apply the soliton-specific control developed here will be carried out in future work.

APPENDIX A

NUMERICAL METHODS FOR DIFFERENTIAL EQUATIONS

A.1 Numerical Method for Solving Schrödinger-Type Equations

It is necessary to solve the GPE (3.1) in order to validate the dimensionality reductions used throughout Chapter 3. Additionally, we must solve Equations (4.10), (4.11), and (6.3), which all have a similar structure to equation (3.1), several times in order to solve optimal control problems. Therefore, in this section, we discuss an efficient numerical method for solving the generalized GPE

$$i\partial_t\psi = -\frac{1}{2}\partial_x^2\psi + V(x,t)\psi + s|\psi|^{2s}\psi, \tag{A.1}$$

where $s \geq 0$, so that the required adjustments for solving Equations (3.1), (4.10), (4.11), and (6.3) are clear. The boundary conditions are assumed to be periodic so that the use of spectral methods is straightforward.

We use an operator splitting method, and, to this end, rewrite Equation (A.1) in the form

$$i\partial_t\psi = \mathcal{L}\psi + \mathcal{N}(\psi), \tag{A.2}$$

where the linear operator is given by $\mathcal{L} = -\frac{1}{2}\partial_x^2$ and the nonlinear and inhomogeneous operator $\mathcal{N}(\psi)$ incorporates the remaining terms. The idea of operator splitting is to "split" the operators on the right-hand side of Equation (A.2). Then, one solves the resulting equations in an alternate and successive manner. More explicitly, we choose to use a second order in time operator splitting, often referred to as Strang splitting [28], to approximate the resulting matrix exponential by

$$e^{(\mathcal{L}+\mathcal{N})Mh} = e^{\mathcal{L}h/2}e^{\mathcal{N}h}e^{\mathcal{L}h}\dots e^{\mathcal{L}h}e^{\mathcal{N}h}e^{\mathcal{L}h/2} + \mathcal{O}\left(h^2\right), \tag{A.3}$$

where $h = T/M$ is the time discretization for a given number of time steps M.

The solution of the linear equation resulting from the matrix exponential $e^{\mathcal{L}h}$ is facilitated by the Fourier transform and is given by

$$\psi_{n+1} = \mathcal{F}^{-1}\left\{\mathcal{F}\{\psi_n\}e^{-\frac{ihk^2}{2}}\right\}, \tag{A.4}$$

where $\mathcal{F}$ and $\mathcal{F}^{-1}$ denote the Fourier and inverse Fourier transformation, respectively. Fourier and inverse Fourier transforms are computed via the fast Fourier transform functions in MATLAB, `fftw` and `ifftw`, with discretized wavenumbers $k \in \left[\frac{-N/2+1}{2\pi l}, \frac{N/2-1}{2\pi l}\right]$, where $2l$ units of length are assumed in the truncated spatial domain and N is the number of spatial discretization points.

The nonlinear equation resulting from the matrix exponential $e^{\mathcal{N}h}$ is quite simple. Since the nonlinearity does not involve spatial derivatives, we are simply tasked with solving ODEs. Using polar coordinates, i.e., letting

$$\psi = \rho(x,t)e^{i\theta(x,t)}, \tag{A.5}$$

results in the ODE

$$\begin{aligned} \partial_t \rho(x,t) &= 0, \\ \partial_t \theta(x,t) &= -s\rho^{2s} - V(x,t). \end{aligned} \tag{A.6}$$

The first of these equations is a statement about conservation of the mass $||\psi_0||_{L^2(\mathbb{R})}$. The second equation, governing the phase θ, can be solved via any number of standard numerical ODE techniques; we simply use the second-order accurate midpoint method. The update for the phase θ, in this case, is

$$\theta(x,t_{n+1}) = \theta(x,t_n) - hs\rho(x,t_n)^{2s} - hV\left(x, t_n + \frac{h}{2}\right) \tag{A.7}$$

The power of operator splitting is evident: the implementation of the method is incredibly straightforward since it is explicit, yet the update

$$\psi_{n+1} = e^{\mathcal{L}h/2}e^{\mathcal{N}h}e^{\mathcal{L}h/2}\psi_n \tag{A.8}$$

only requires the computation of two fast Fourier transforms, two fast inverse Fourier transforms, and a pointwise evaluation of the potential V. In fact,

the Strang splitting formula (A.3) cuts the required number of Fourier and inverse Fourier transforms approximately in half. Moreover, since the operators are split into a stiff linear operator and a non-stiff nonlinear operator, issues of numerical stability are less relevant. For the Schrödinger-type equations considered throughout this dissertation, we can always find a suitable and computationally reasonable enough time discretization h which yields a stable computation for a given spatial discretization $\frac{2l}{N}$.

A.2 Numerical Methods for Solving Coupled-Mode Equations

The coupled-mode equations

$$\begin{aligned} i\partial_t u + i\partial_x u + \kappa(x)v + \eta(x)u + \left(|u|^2 + 2\,|v|^2\right) u = 0, \\ i\partial_t v - i\partial_x v + \kappa(x)u + \eta(x)v + \left(2\,|u|^2 + |v|^2\right) v = 0, \end{aligned} \tag{A.9}$$

are somewhat more difficult to solve than the GPE (A.1). The experience gained from the previous section strongly encourages us to continue using operator splitting methods whenever they are available. For this reason, we follow a known operator splitting method, first developed by Rosenthal and Horowitz [56], for solving Equation (A.9). They use a method which is first-order in time, and we improve this to a second-order in time method by using a symmetric Strang-MacNamara splitting [28].

This improvement is critical in an optimization since it cuts the number of necessary spatial discretization points in half, which also effectively cuts the computation time of evaluating the functional (5.17) in half; searches for optimal grating functions is on the order of hours. Note that the splitting methods of this section fundamentally assume the solutions of Equations (A.9) are analytic. Although this is a strong assumption to make given that the grating functions are only assumed to be absolutely continuous, we believe the resulting numerical simulations justify this assumption a posteriori.

Most operator splitting methods split the linear and nonlinear operators into two separate operators, as was done in the previous section. However,

since the numerical simulations require signalling data without a backpropagating component $v(x,t)$, this means solving the state equations (5.4) using a method which splits the linear and nonlinear operators is not available; v is excited by the coupling through the linear *and* nonlinear terms.

Instead, the method of Rosenthal and Horowitz splits Equation (5.4) into

$$\partial_t \begin{pmatrix} u \\ v \end{pmatrix} = (A+B) \begin{pmatrix} u \\ v \end{pmatrix}, \tag{A.10}$$

where the matrix operator A is defined as

$$A = i \begin{pmatrix} -\partial_x \bullet + (|\bullet|^2 + 2|v|^2)\bullet & 0 \\ 0 & \partial_x \bullet + (2|u|^2 + |\bullet|^2)\bullet \end{pmatrix}, \tag{A.11}$$

using $\bullet$ to help express how the operator A functions, and where the matrix B is

$$B = i \begin{pmatrix} \eta & \kappa \\ \kappa & \eta \end{pmatrix}. \tag{A.12}$$

Computations involving the matrix exponential of B are simple. Using the Taylor series definition of the matrix exponential and diagonalizing the operator B into canonical form, we have

$$\begin{aligned} e^{B\Delta t} = \sum_{n=0}^{\infty} \frac{(B\Delta t)^j}{j!} &= P \sum_{n=0}^{\infty} \frac{(\Delta t \Lambda)^n}{n!} P^{-1} = P e^{i\Delta t \Lambda} P^{-1} \\ &= e^{i\Delta t \eta} \begin{pmatrix} \cos(\kappa \Delta t) & i\sin(\kappa \Delta t) \\ i\sin(\kappa \Delta t) & \cos(\kappa \Delta t) \end{pmatrix}, \end{aligned} \tag{A.13}$$

where the matrix Λ is the 2×2 diagonal eigenvalue matrix of B, and P is a 2×2 matrix whose columns are eigenvectors of B.

The computation of $e^{A\Delta t}$ is more subtle and explicitly assumes analyticity of the coupled modes u and v. Observe the effect of the following operator on monomials:

$$e^{a\partial_x} x^m = \sum_{k=0}^{\infty} \frac{(a\partial_x)^k}{k!} x^m = \sum_{k=0}^{m} \begin{pmatrix} m \\ k \end{pmatrix} a^k x^{m-k} = (x+a)^m. \tag{A.14}$$

Remarkably, the effect of this operator is simply a spatial translation of a units. Therefore, it is easy to show the effect of this operator on a function $f(x)$, analytic in a neighborhood about $x = 0$, is

$$e^{a\partial_x} f(x) = f(x + a). \tag{A.15}$$

This implies directly that

$$e^{A\Delta t} \begin{pmatrix} u(x,t) \\ v(x,t) \end{pmatrix} = \begin{pmatrix} e^{i\Delta\left(|u(x-\Delta t,t)|^2+2|v(x,t)|^2\right)} u(x - \Delta t, t) \\ e^{i\Delta\left(2|u(x,t)|^2+|v(x+\Delta t,t)|^2\right)} v(x + \Delta t, t) \end{pmatrix}, \tag{A.16}$$

is simply an appropriately coupled, advective update.

Clearly, this method also couples the spatial and temporal discretizations, and for this reason, we follow Rosenthal and Horowitz in choosing $\Delta t = \Delta x := \Delta$. The first-order composition of propagators, after M time steps, is straightforward:

$$e^{(A+B)M\Delta} = e^{B\Delta} e^{A\Delta} \dots e^{B\Delta} e^{A\Delta} + \mathcal{O}(\Delta). \tag{A.17}$$

The improvement we make on this method is facilitated by using the symmetric average suggested by MacNamara and Strang [28]:

$$e^{(A+B)M\Delta} = \frac{1}{2^M} \left(e^{A\Delta} e^{B\Delta} + e^{B\Delta} e^{A\Delta}\right) \dots \left(e^{A\Delta} e^{B\Delta} + e^{B\Delta} e^{A\Delta}\right) + \mathcal{O}\left(\Delta^2\right), \tag{A.18}$$

where the matrix exponential $e^{A\Delta} e^{B\Delta}$ is computed by similar means of computing $e^{B\Delta} e^{A\Delta}$. Note that the previously used splitting formula (A.3) is not easily available because of the coupling of discretizations Δ.

As required by the gradient descent algorithm (3), we must also solve the costate, or coupled-mode adjoint, equations

$$i\partial_t \lambda + i\partial_x \lambda + \left(\eta + 2\mathcal{E} + u^{\dagger 2}\right) \lambda + \left(\kappa + 4v^\dagger \Re\{u\}\right) \mu = 0, \tag{A.19}$$

$$i\partial_t \mu - i\partial_x \mu + \left(\eta + 2\mathcal{E} + v^{\dagger 2}\right) \mu + \left(\kappa + 4u^\dagger \Re\{v\}\right) \lambda = 0, \tag{A.20}$$

$$\lambda(x,T) = 2iH(x-a)\Re\{u(x,T)\}, \tag{A.21}$$

$$\mu(x,T) = 2iH(x-a)\Re\{v(x,T)\}, \tag{A.22}$$

derived in Section B.2. To this end, we use the splitting

$$\partial_t \begin{pmatrix} \lambda \\ \mu \end{pmatrix} = (C + D) \begin{pmatrix} \lambda \\ \mu \end{pmatrix}, \tag{A.23}$$

where the matrix operator C is defined as

$$C = \begin{pmatrix} -\partial_x & 0 \\ 0 & \partial_x \end{pmatrix}, \tag{A.24}$$

and the matrix D is given by

$$D = i \begin{pmatrix} f_1 & f_2 \\ f_3 & f_4, \end{pmatrix} \tag{A.25}$$

where

$$f_1(x,t) = \eta + 2\left(|u|^2 + |v|^2\right) + u^{\dagger 2}, \tag{A.26}$$

$$f_2(x,t) = \kappa + 4v^\dagger \Re\{u\}, \tag{A.27}$$

$$f_3(x,t) = \kappa + 4u^\dagger \Re\{v\}, \tag{A.28}$$

$$f_4(x,t) = \eta + 2\left(|u|^2 + |v|^2\right) + v^{\dagger 2}. \tag{A.29}$$

In order to evolve the costates, we must do so backwards in time, since the terminal conditions (A.21)–(A.22) are specified at the final time of simulation. The first-order backward composition of operators

$$e^{-(C+D)M\Delta} = e^{-D\Delta}e^{-C\Delta}\ldots e^{-D\Delta}e^{-C\Delta} + \mathcal{O}\left(\Delta\right), \tag{A.30}$$

is straightforward to form through computations of

$$e^{-C\Delta}\begin{pmatrix} \lambda(x,t) \\ \mu(x,t) \end{pmatrix} = \begin{pmatrix} \lambda(x+\Delta,t) \\ \mu(x-\Delta,t) \end{pmatrix} \tag{A.31}$$

and

$$e^{-D\Delta} = e^{-\frac{i\Delta}{2}(f_1+f_4)}\begin{pmatrix} \cos\left(\frac{\varphi\Delta}{2}\right) - \frac{i\phi}{\varphi}\sin\left(\frac{\varphi\Delta}{2}\right) & -\frac{2if_2}{\varphi}\sin\left(\frac{\varphi\Delta}{2}\right) \\ -\frac{2if_3}{\varphi}\sin\left(\frac{\varphi\Delta}{2}\right) & \cos\left(\frac{\varphi\Delta}{2}\right) + \frac{i\phi}{\varphi}\sin\left(\frac{\varphi\Delta}{2}\right) \end{pmatrix}, \tag{A.32}$$

where

$$\phi = f_1 - f_4, \tag{A.33a}$$

$$\varphi = \sqrt{\phi^2 + 4f_2 f_3}. \tag{A.33b}$$

Using the symmetric average (A.18) as before, and computing $e^{-D\Delta}e^{-C\Delta}$ via similar means, yields a second-order in time method for the adjoint coupled-mode equations (A.19)–(A.22).

A.3 Numerical Method for the Perturbed Korteweg-deVries Equation

We use the Strang splitting method (A.3) in order to solve the KdV-type Equation (6.1). To this end, the KdV-type equation is written in the form

$$\partial_t q = \mathcal{L}q + \mathcal{N} \tag{A.34}$$

where the linear operator is given by $\mathcal{L} = -\partial_x^3$, and the operator $\mathcal{N}$ incorporates all other terms. The update for the linear operator is given simply by

$$q_{n+1} = \mathcal{F}^{-1}\left\{\mathcal{F}\{q_n\}e^{ihk^3}\right\}. \tag{A.35}$$

Computing the update for $\mathcal{N}$ is slightly more challenging than that of Equation (A.1). In the case of Equation (6.1), we are tasked with solving

$$\partial_t q + 3\partial_x q^2 + \Gamma(t)q = 0. \tag{A.36}$$

We use an integrating factor and the Fourier transform to rewrite this as

$$\partial_t\left(e^{-\int^t \Gamma(s)ds}\hat{q}\right) = -3ik\widehat{q^2}, \tag{A.37}$$

where, by the explicit form of Γ, the integrating factor can be computed in closed form as $e^{-\frac{9}{4}\int^t \partial_s \log D(s)ds} = D^{-\frac{9}{4}}(t)$. Now, using the change of variables $w = D^{-\frac{9}{4}}\hat{q}$, we have

$$\partial_t w = -3ikD^{\frac{9}{2}}\mathcal{F}\left\{\mathcal{F}^{-1}\{w\}^2\right\}, \tag{A.38}$$

which is an ODE which can easily be solved by the midpoint rule as was done in Section A.1.

APPENDIX B

OPTIMALITY CONDITIONS FOR CONTROL PROBLEMS

B.1 Optimality Conditions for Control of Stationary States

Recall the optimal control problem of Chapter 4:

$$\min_{u\in\mathcal{U}} \mathcal{J} = \min_{u\in\mathcal{U}} \left\{ \frac{1}{2}\left(||\varphi_d||^4_{L^2(\mathbb{R}^n)} - |\langle \varphi_d, \varphi_T\rangle|^2_{L^2(\mathbb{R}^n)} \right) + \frac{\gamma}{2}\int_0^l |\partial_z u|^2 \, dz \right\}, \tag{B.1}$$

subject to

$$i\partial_z \psi + P(x,u,D)\psi = 0, \tag{B.2a}$$

$$\psi(x,0) = \varphi_0(x), \tag{B.2b}$$

where the wave function $\psi(x,t) \in L^2\left([0,T]; H^{|\alpha|-1}(\mathbb{R})\right)$, and all other conventions are consistent with the problem description in Section 4.2.

We use the strategy outlined in Subsection 2.4.4, and reflected by Equation (2.36), in order to compute Gateaux derivatives of the objective $\mathcal{J}$. That is, we use the method of Lagrange multipliers, and the fundamental theorem of calculus to convert the Bolza control problem (B.1) into the Lagrange form (2.35). The infidelity, in this case, can be rewritten as

$$\mathcal{J}_{\text{infidelity}} = -\int_0^l \Re\left\{ \langle \varphi_d, \psi\rangle \langle \partial_z \psi, \varphi_d\rangle \right\} dz. \tag{B.3}$$

By using the Lagrange multiplier $p \in L^2\left([0,T]; H^{|\alpha|-1}(\mathbb{R})\right)$, the Lagrange density is given by

$$\begin{aligned} \mathcal{L} &= \Re\left\{ \langle p, i\partial_z\psi + P\psi\rangle - \langle \varphi_d, \psi\rangle \langle \partial_z\psi, \varphi_d\rangle \right\} + \frac{\gamma}{2}|\partial_z u|^2, \\ &= \int_{\mathbb{R}^\kappa} \Re\left\{ \mathcal{S}\left(\psi, \psi^\dagger, p^\dagger, \partial_z\psi, P\psi, u\right)\right\} dx + \frac{\gamma}{2}|\partial_z u|^2 \end{aligned} \tag{B.4}$$

where † denotes hermitian conjugation.

The unconstrained optimization problem now takes the Lagrange form

$$\min_{u\in\mathcal{U}} \int_0^l \mathcal{L}(\psi, \partial_z\psi, P\psi, \psi^\dagger, p^\dagger, u, \partial_z u) dz. \tag{B.5}$$

We now show how to use Lagrange's method of variations to formally compute the necessary optimality conditions of problem (B.5). Start by writing a formal Taylor series about each of its optimal functional variables

$$\psi = \sum_{n=0}^{\infty} \varepsilon^n \psi_n, \quad p = \sum_{n=0}^{\infty} \varepsilon^n p_n, \quad u = \sum_{n=0}^{\infty} \varepsilon^n u_n, \tag{B.6}$$

where the first term in each expansion is a functional variable in the set of local minimizers of $\mathcal{J}$ and each function thereafter in the respective expansion is in an appropriate function space, i.e., they are infinitely differentiable in all of its variables and, $\forall n \in \mathbb{N}$, satisfy the adjoint boundary conditions

$$\begin{aligned} \psi_n(x,0) &= 0, & p_n(x,0) &= 0 \\ u_n(0) &= 0, & u_n(l) &= 0 \\ \lim_{x\to\pm\infty} \psi_n &= 0, & \lim_{x\to\pm\infty} p_n &= 0. \end{aligned} \tag{B.7}$$

The n^{th} functional derivative of the objective is then defined as

$$\delta^n J := \frac{1}{n!} \frac{d^n J}{d\varepsilon^n}\bigg|_{\varepsilon=0}. \tag{B.8}$$

Using the formal series (B.6), we can, in principle, compute as many functional derivatives as desired. For the purposes of Chapter 4, we are only interested in the first functional derivative δJ. By making use of the Lebesgue Dominated Convergence Theorem, Leibniz's rule, the chain rule, integration by parts, and boundary conditions (B.7), we compute the first functional derivative δJ as follows:

$$
\begin{aligned}
&d_\varepsilon \mathcal{J}\big|_{\varepsilon=0} = \lim_{\varepsilon\to 0} d_\varepsilon \int_0^l \mathcal{L}(\psi, \partial_z\psi, P\psi, \psi^\dagger p^\dagger, u, \partial_z u)dz, \\
&= \int_0^l \lim_{\varepsilon\to 0} \partial_\varepsilon \mathcal{L}(\psi, \partial_z\psi, P\psi, \psi^\dagger, p^\dagger, u, \partial_z u)dz, \\
&= \int_0^l \left(\langle \partial_\psi \mathcal{S}, \partial_\varepsilon \psi\rangle + \langle \partial_{\partial_z\psi}\mathcal{S}, \partial_\varepsilon\partial_z\psi\rangle + \langle \partial_{P\psi}\mathcal{S}, \partial_\varepsilon P\psi\rangle + \left\langle \partial_{\psi^\dagger}\mathcal{S}, \partial_\varepsilon\psi^\dagger\right\rangle\right)\big|_{\varepsilon=0} dz \\
&+ \int_0^l \left(\left\langle \partial_{p^\dagger}\mathcal{S}, \partial_\varepsilon p^\dagger\right\rangle + \partial_u\mathcal{L}\partial_\varepsilon u + \partial_{\partial_z u}\mathcal{L}\partial_\varepsilon\partial_z u\right)\big|_{\varepsilon=0} dz, \\
&= \int_0^l \left\langle \psi_1, \partial_\psi\mathcal{S} - \partial_z\partial_{\partial_z\psi}\mathcal{S} + P^\dagger\partial_{P\psi}\mathcal{S} + \partial_{\psi^\dagger}\mathcal{S}\right\rangle dz \\
&+ \int_0^l \left(\left\langle p_1, \partial_{p^\dagger}\mathcal{S}\right\rangle + {u_1}^\dagger\left(\partial_u\mathcal{L} - \partial_z\partial_{\partial_z u}\mathcal{L}\right)\right)dz + \left\langle {\psi_1}^\dagger, \partial_{\partial_z\psi}\mathcal{L}\right\rangle\big|_{z=l}, \\
&:= \left\langle \psi_1, \partial_{\partial_z\psi}\mathcal{L}\big|_{z=l}\right\rangle_{\mathbb{R}^n} + \left\langle \psi_1, \delta_\psi\mathcal{J} + \delta_{\psi^\dagger}\mathcal{J}\right\rangle_{L^2([0,l])} \\
&+ \left\langle p_1, \delta_{p^\dagger}\mathcal{J}\right\rangle_{L^2([0,l])} + \left\langle u_1, \delta_u\mathcal{J}\right\rangle_{L^2([0,l])}.
\end{aligned}
\tag{B.9}
$$

Since the functional perturbations $\psi_1,\ p_1$, and u_1 are arbitrary in their respective function spaces, we can conclude by the Fundamental Lemma of the Calculus of Variations [27], δJ vanishes if and only if the Euler-Lagrange equations

$$
\delta_\psi\mathcal{J} + \delta_{\psi^\dagger}\mathcal{J} = \partial_\psi\mathcal{S} - \partial_z\partial_{\partial_z\psi}\mathcal{S} + P^\dagger\partial_{P\psi}\mathcal{S} + \partial_{\psi^\dagger}\mathcal{S} = 0, \quad \partial_{\partial_z\psi}\mathcal{L}\big|_{z=l} = 0, \tag{B.10a}
$$

$$
\delta_{p^\dagger}\mathcal{J} = \partial_{p^\dagger}\mathcal{S} = 0, \qquad \psi(x,0) = \varphi_0(x), \tag{B.10b}
$$

$$
\delta_u\mathcal{J} = \partial_u\mathcal{L} - \partial_z\partial_{\partial_z u}\mathcal{L} = 0, \qquad u \in \mathcal{U} \tag{B.10c}
$$

are satisfied. The corresponding equations reduce to

$$
i\partial_z p = P^\dagger p, \qquad ip(x,l) = \langle \varphi_d, \psi(x,l)\rangle_{L^2(\mathbb{R}^n)}\,\varphi_d, \tag{B.11a}
$$

$$
i\partial_z\psi = P\psi, \qquad \psi(x,0) = \varphi_0(x), \tag{B.11b}
$$

$$
\gamma\partial_z^2 u = -\Re\left\langle p, \partial_u P\psi\right\rangle_{L^2(\mathbb{R}^n)}, \qquad u(0) = u_0,\ u(l) = u_l. \tag{B.11c}
$$

A revealing way to view the system of optimality conditions (B.11) is through the Hamiltonian

$$
\mathcal{H} = \Re\left\{\langle p, P\psi\rangle - \langle \varphi_d, \psi\rangle\langle \partial_z\psi, \varphi_d\rangle\right\} + \frac{\gamma}{2}|\partial_z u|^2. \tag{B.12}
$$

From this, we see that the state ψ and adjoint state $p^\dagger$ form the following Hamiltonian system

$$i\partial_z \psi = +\nabla_{p^\dagger} \mathcal{H}, \tag{B.13}$$

$$i\partial_z p^\dagger = -\nabla_{\psi} \mathcal{H}, \tag{B.14}$$

where the gradient operator ∇ is understood in the sense of $L^2([0,l])$, i.e., if we let

$$\mathcal{J} = \int_0^l \mathcal{H} dz, \tag{B.15}$$

then

$$\nabla_{p^\dagger} \mathcal{H} = \delta_{p^\dagger} \mathcal{J}, \tag{B.16}$$

$$\nabla_{\psi} \mathcal{H} = \delta_{\psi} \mathcal{J}. \tag{B.17}$$

This result provides part of the appropriate generalization of the Pontryagin principle (2.3.1) to the optimal control problem (4.1) constrained by class of linear dispersive wave equations (4.2a).

B.2 Optimality Conditions for Coupling Light into Bragg Gratings

We now derive the optimality conditions for the optimal control problem of Chapter 4, written here

$$\min_{(\kappa,\eta)\in\mathcal{C}} J = \min_{(\kappa,\eta)\in\mathcal{C}} \left\{ -\int_0^T \mathcal{F}_{\mathcal{E}}(u,v;a)dt + \frac{\gamma}{2}\int_0^a \left(\partial_x^2\kappa^2 + \partial_x^2\eta\right) dx \right\}, \tag{B.18}$$

subject to

$$\begin{aligned} &i\partial_t u + i\partial_x u + \kappa(x)v + \eta(x)u + \left(|u|^2 + 2|v|^2\right)u = 0, \\ &i\partial_t v - i\partial_x v + \kappa(x)u + \eta(x)v + \left(2|u|^2 + |v|^2\right)v = 0, \end{aligned} \tag{B.19}$$

where the admissible class $\mathcal{C}$ of grating structures is given by the space of absolutely continuous functions on $\mathbb{R}$ such that

$$\kappa(x) = \begin{cases} 0 & x \leq 0, \\ \kappa_0 & a \leq x, \end{cases} \quad \text{and} \quad \eta(x) = \begin{cases} 0 & x \leq 0, \\ 0 & a \leq x. \end{cases} \tag{B.20}$$

To this end, let $H(x-a)$ denote Heaviside's function. We rewrite the energy flux term in objective (B.18), assuming the flux vanishes at infinity, as

$$\begin{aligned} -\partial_t \mathcal{F}_{\mathcal{E}}\big|_{x=a} &= \int_{-\infty}^{\infty} H(x-a) \int_0^T \partial_t \mathcal{E} dt dx \\ &= \int_{-\infty}^{\infty} H(x-a) \int_0^T \left(u^\dagger \partial_t u + u \partial_t u^\dagger + v^\dagger \partial_t v + v \partial_t v^\dagger \right) dt dx, \end{aligned} \tag{B.21}$$

by using the fundamental theorem of calculus and the conservation laws (5.9), (5.15).

Using the method of Lagrange multipliers, we define the Lagrangian

$$\begin{aligned} \mathcal{L} =& \Re \left\langle \lambda, i\partial_t u + i\partial_x u + \kappa(x) v + \eta(x) u + \left(|u|^2 + 2|v|^2 \right) u \right\rangle_{L^2([0,T])} \\ &+ \Re \left\langle \mu, i\partial_t v - i\partial_x v + \kappa(x) u + \eta(x) v + \left(2|u|^2 + |v|^2 \right) v \right\rangle_{L^2([0,T])} \\ &+ H(x-a) \int_0^T \left(u^\dagger \partial_t u + u \partial_t u^\dagger + v^\dagger \partial_t v + v \partial_t v^\dagger \right) dt, \end{aligned} \tag{B.22}$$

so that the objective in optimal control problem (B.18) in Lagrange form is

$$\mathcal{J} = \int_{\mathbb{R}} \Re \left\{ \mathcal{L} \left(u, v, \partial_t u, \partial_t u^\dagger \partial_t v, \partial_t v^\dagger, \partial_x u, \partial_x v, \kappa, \eta, \lambda^\dagger, \mu^\dagger \right) \right\} dx \tag{B.23}$$

Using the typical arguments from the classical calculus of variations [27] and used in the previous section, we find the desired optimality conditions by taking the appropriate functional derivatives. Setting functional derivatives with respect to the state variables to zero gives

$$\frac{\delta \mathcal{J}}{\delta u} + \frac{\delta \mathcal{J}}{\delta u^\dagger} = 0, \tag{B.24a}$$

$$\rightarrow i\partial_t \lambda + i\partial_x \lambda + \left(\eta + 2\mathcal{E} + u^{\dagger 2} \right) \lambda + \left(\kappa + 4v^\dagger \Re\{u\} \right) \mu = 0, \tag{B.24b}$$

$$\frac{\delta \mathcal{J}}{\delta v} + \frac{\delta \mathcal{J}}{\delta v^\dagger} = 0, \tag{B.24c}$$

$$\rightarrow i\partial_t \mu - i\partial_x \mu + \left(\eta + 2\mathcal{E} + v^{\dagger 2} \right) \mu + \left(\kappa + 4u^\dagger \Re\{v\} \right) \lambda = 0, \tag{B.24d}$$

where $\rightarrow$ means the equation that is implied by the vanishing functional derivative. An integration by parts yields boundary terms (B.25) which must also be set to zero:

$$(\partial_{\partial_t u}\mathcal{L} + \partial_{\partial_t u^\dagger}\mathcal{L})\Big|_{t=T} = 0 \rightarrow \lambda(x,T) = 2iH(x-a)\Re\left\{u(x,T)\right\}, \tag{B.25a}$$

$$(\partial_{\partial_t v}\mathcal{L} + \partial_{\partial_t v^\dagger}\mathcal{L})\Big|_{t=T} = 0 \rightarrow \mu(x,T) = 2iH(x-a)\Re\left\{v(x,T)\right\}. \tag{B.25b}$$

Since variations of the states u and v need not vanish at $t = T$, equations (B.25) must be satisfied. Indeed, these conditions determine, what is in essence, an initial condition for the equations (B.24) which can then be solved backwards in time.

Next, setting functional derivatives with respect to the control variables to zero gives

$$\delta_\kappa \mathcal{J} = \int_0^T \Re\left\{\lambda^\dagger v + \mu^\dagger u\right\} dt - \gamma\partial_x^2\kappa = 0, \tag{B.26a}$$

$$\delta_\eta \mathcal{J} = \int_0^T \Re\left\{\lambda^\dagger u + \mu^\dagger v\right\} dt - \gamma\partial_x^2\eta = 0. \tag{B.26b}$$

Equations (B.26), together with the boundary conditions implied by the admissible class $\mathcal{C}$, gives two-point boundary value problems over the domain $[0, a]$. Lastly, vanishing functional derivatives with respect to the costate variables $\lambda^\dagger$ and $\mu^\dagger$ gives back the state equations (B.19), i.e., the NLCME.

B.3 Optimality Conditions for Korteweg-deVries Contol

Recall the optimal control problem of Chapter 6:

$$\inf_{D\in\mathcal{D}} \mathcal{J} = \frac{1}{2}\inf_{D\in\mathcal{D}} \int_0^T \left(\Lambda_{\mathcal{J}}^2 + \gamma\partial_t D^2\right) dt \tag{B.27}$$

subject to

$$\begin{aligned} \partial_t q + 6q\partial_x q + \partial_x^3 q + \Gamma(t)q = 0, \\ q(x,0) = \alpha^2 \operatorname{sech}^2 \frac{\alpha x}{2}, \end{aligned} \tag{B.28}$$

where $\Gamma = \frac{9}{4}\partial_t \log D,\ \alpha > 0,\ \gamma > 0$, the admissible class of topographies $D(t)$ is

$$\mathcal{D} = \left\{ D \in H^1([0,T]) : D(0) = D_0,\ D(T) = D_T,\ D_T > D_0 \right\}, \tag{B.29}$$

and the first term in the running cost is given by

$$\Lambda_{\mathcal{J}} = \int_{\mathbb{R}} q dx - 4\eta_1(t), \tag{B.30}$$

where η_1 is the smallest singular value, in absolute value, of the eigenvalue problem

$$\partial_x^2 \psi + \left(q - \eta^2\right)\psi = 0. \tag{B.31}$$

Our strategy for formally deriving the necessary optimality conditions here mimics those of the previous sections of this appendix. We being by converting Λ_J to a functional which more explicitly involves the ground state eigenfunction ψ_1. This is easily done by using the Rayleigh quotient

$$\eta_1^2 = \int_{\mathbb{R}} \left(q\psi_1^2 - \left(\partial_x \psi_1\right)^2\right) dx. \tag{B.32}$$

The Lagrangian for our problem is thus given by

$$\begin{aligned}
\mathcal{L} &= \left\langle p, \partial_t q + 6q\partial_x q + \partial_x^3 q + \Gamma(t) q \right\rangle_{L^2(\mathbb{R})} + \left\langle \varphi, \partial_x^2 \psi + (q - \xi)\psi \right\rangle_{L^2(\mathbb{R})} \\
&\quad + \frac{1}{2}\left(\left(\beta D^{-\frac{9}{4}} - 4\xi^{1/2}\right)^2 + \gamma \left(\partial_t D\right)^2 \right), \\
&= \int_{\mathbb{R}} \mathcal{S}\left(q, \partial_t q, \partial_x q, \partial_x^3 q, p, \psi, \partial_x \psi, \partial_x^2 \psi, \xi, \varphi, D\right) dx + \mathcal{F}\left(\xi, D, \partial_t D\right),
\end{aligned} \tag{B.33}$$

where we use Lagrange multipliers p and φ, made explicit use of the Rayleigh quotient (B.32) and the mass law (6.6), and, for sake of clarity in using the chain rule, we use the notation

$$\mathcal{F}\left(\xi, D, \partial_t D\right) = \beta^2 D^{-\frac{9}{2}} - 8\beta D^{-\frac{9}{4}} \xi^{\frac{1}{2}} + \frac{\gamma}{2} \partial_t D^2, \tag{B.34}$$

$$\xi = \int_{\mathbb{R}} \mathcal{G}(q, \psi, \partial_x \psi) dx, \tag{B.35}$$

$$\mathcal{G}(q, \psi, \partial_x \psi) = q\psi^2 - \left(\partial_x \psi\right)^2, \tag{B.36}$$

with the subscript on the ground state ψ_1 dropped. Taking the appropriate functional derivatives and setting them equal to 0 gives

$$\delta_q \mathcal{J} = \partial_q \mathcal{S} - \partial_x \partial_{\partial_x q} \mathcal{S} - \partial_x^3 \partial_{\partial_x^3 q} \mathcal{S} - \partial_t \partial_{\partial_t q} \mathcal{S} + \partial_\xi \mathcal{F} \partial_q \mathcal{G} = 0, \quad \text{(B.37)}$$

$$\delta_\psi \mathcal{J} = \partial_\psi \mathcal{S} - \partial_x \partial_{\partial_x \psi} \mathcal{S} + \partial_x^2 \partial_{\partial_x^2 \psi} \mathcal{S} + (\partial_\xi \mathcal{S} + \partial_\xi \mathcal{F}) (\partial_\psi \mathcal{G} - \partial_x \partial_{\partial_x \psi} \mathcal{G}) = 0, \quad \text{(B.38)}$$

$$\delta_D \mathcal{J} = \partial_D \mathcal{S} - \partial_t \partial_{\partial_t D} \mathcal{S} + \partial_D \mathcal{F} - \partial_t \partial_{\partial_t D} \mathcal{F} = 0, \quad \text{(B.39)}$$

$$\partial_{\partial_t q} \mathcal{S}\big|_{t=T} = 0, \quad \text{(B.40)}$$

while setting functional derivatives with respect to the Lagrange multipliers p and φ yields Equations (B.28) and (B.31), respectively. For the explicit forms of $\mathcal{F}, \mathcal{S}$, and $\mathcal{G}$, the corresponding Euler-Lagrange equations (B.37)–(B.39) read

$$\partial_t p + 6q\partial_x p + \partial_x^3 p - \Gamma(t) p - \varphi\psi - \frac{1}{2}\xi^{\frac{1}{2}}\psi^2 = 0, \quad \text{(B.41)}$$

$$\partial_x^2 \varphi + (q - \xi)\varphi - 2\partial_x^2 \psi - 2\left(\psi\varphi + 4\beta D^{-\frac{9}{4}} \xi^{-\frac{1}{2}}\right)\left(\partial_x^2 \psi + (q - \xi)\psi\right) = 0, \quad \text{(B.42)}$$

$$\gamma \partial_t^2 D - \frac{9}{4}\partial_t \frac{pq}{D} + \frac{9}{4} D^{-2} \partial_t D + \frac{9}{4}\beta^2 D^{-\frac{11}{2}} - 9\xi^{\frac{1}{2}}\beta D^{-\frac{13}{4}} = 0, \quad \text{(B.43)}$$

$$p(x, T) = 0. \quad \text{(B.44)}$$

APPENDIX C

THE KORTEWEG-DEVRIES TRACE FORMULAE

We outline a method for constructing the trace formulae; representations of conserved quantites of integrable systems in terms of the spectrum of the associated Zakharov-Shabat (ZS) operator. This method is presented for the Korteweg-deVries (KdV) equation in full detail in the book [52]. We present the basics of the inverse scattering transform as an aid for understanding the trace formula (6.5). Unfortunately, we skip over much of the beautiful machinery of the inverse scattering transform so that our goal can be met in a somewhat concise fashion.

We start by observing that the following change of variables, first suggested by Miura and Gardner [26]. Let $q(x,t)$ satisfy the Korteweg-deVries equation

$$\partial_t q + 6q\partial_x q + \partial_x^3 q = 0. \tag{C.1}$$

Then, by substituting

$$q = w + \frac{i}{2\zeta}\partial_x w + \frac{1}{4\zeta^2}w^2, \tag{C.2}$$

into Equation (C.1), and substituting

$$w = 2i\zeta\partial_x \log\psi - 2\zeta^2, \tag{C.3}$$

into the resulting equation, we arrive at

$$\partial_x^2\psi + \left(\zeta^2 + q(x,t)\right)\psi = 0. \tag{C.4}$$

The inverse scattering formalism seeks to understand the behavior of an integrable system, in this case the KdV equation, through the scattering properties of the potential energy $q(x,t)$ as it appears in Equation (C.4). It is also helpful to know Schrödinger's equation can be rewritten as a system of first order equations,

referred to as the (Zakharov-Shabat) form,

$$\begin{pmatrix} \partial_x - i\zeta & 1 \\ -u & \partial_x + i\zeta \end{pmatrix} \begin{pmatrix} \psi \\ \varphi \end{pmatrix} = \begin{pmatrix} 0 \\ 0 \end{pmatrix}, \tag{C.5}$$

by letting $\partial_x \psi = i\zeta\psi - \varphi$. The associated eigenvalue problem (C.4) written in the form of (C.5) is canonical.

When using singular perturbative techniques in quantum mechanics, it is common to rewrite the Schrödinger equation in terms of a Ricatti equation by letting [7]

$$\psi = e^{i\zeta x + \Phi}, \tag{C.6}$$

so that

$$-2i\zeta\partial_x\Phi = q + \partial_x^2\Phi + \partial_x\Phi^2. \tag{C.7}$$

We can iteratively solve for $\partial_x\Phi$, by setting

$$\partial_x\Phi = \sum_{n=1}^{\infty} (2i\zeta)^{-n} R_n. \tag{C.8}$$

It's easy to see that the functions $R_n(x)$ are such that

$$\begin{aligned} R_1 &= -q, \\ R_{n+1} &= -\partial_x R_n - \sum_{k=1}^{n-1} R_k R_{n-k}, \quad n \geq 1, \end{aligned} \tag{C.9}$$

Up to a sign difference, equations (C.9) are the conserved densities of the KdV equation. Historically speaking, Miura knew how to calculate the first 10 conserved quantities by shear brute force. Gardner more systematically expanded equations (C.2)–(C.4) in powers of ζ^{-1} and integrated. We can view the usage of the Liouville-Green method as another systematic means of calculating an arbitrary number of conservation laws, or better yet, the most straightforward way of finding conserved quantities of more complicated, yet still integrable PDE. Moreover, using equations (C.5) and (C.9), we can establish the following

asymptotic result

$$\left(\psi - \frac{1}{2i\zeta}\varphi\right) e^{-i\zeta x} \sim \exp\left(-\sum_{n=1}^{\infty}(2i\zeta)^{-n}\int_{-\infty}^{\infty} R_n dx\right), \quad \text{as } x \to -\infty. \tag{C.10}$$

Result (C.10) will be relevant again shortly.

Once we've established properties of the associated ZS eigenvalue problem, the basic idea of inverse scattering on the infinite real line proceeds as follows. Imagine there is a wave traveling inward from $+\infty$ and incident on some potential. We expect the following Fresnel equations

$$\begin{aligned} \Psi &\sim e^{-i\zeta x} + R(\zeta)e^{i\zeta x}, \quad \text{as } x \to +\infty, \\ \Psi &\sim T(\zeta)e^{-i\zeta x}, \qquad\quad \text{as } x \to -\infty, \end{aligned} \tag{C.11}$$

where Ψ is any evanescent solution to the Schrödinger equation, to hold in the appropriate limits. The following Volterra integral equations

$$\varphi(\zeta, x) = e^{-i\zeta x} - \zeta^{-1}\int_x^{\infty} d\xi \sin(\zeta(x-\xi))q(\xi,t)\varphi(\zeta,\xi), \tag{C.12}$$

$$\psi(\zeta, x) = e^{i\zeta x} - \zeta^{-1}\int_x^{\infty} d\xi \sin(\zeta(x-\xi))q(\xi,t)\psi(\zeta,\xi) \tag{C.13}$$

are the irregular solutions of equation (C.4). These equations make sense whenever $q(x,t)$ has the right polynomial decay in space, i.e. $\int_{\mathbb{R}} x|q(x,t)|dx < \infty$ [79]. This will always be the case for problems we are computationally interested in solving. However, for purposes of justifying what follows, Deift and Trubowitz [20] established the correct class of potentials to study are those potentials that satisfy

$$\int_{\mathbb{R}} (1+x^2)|q(x,t)|dx < \infty. \tag{C.14}$$

In essence, this condition requires that q be in $L^1(\mathbb{R}) \cap H_0^1(\mathbb{R})$, by Plancherel's theorem [39]. Therefore, by the Riemann-Lebesgue Lemma, we see the following limits of Equations (C.12) and (C.13)

$$\begin{aligned} \varphi(x,\zeta) &\sim e^{-i\zeta x}, \quad \text{as } x \to -\infty, \\ \psi(x,\zeta) &\sim e^{i\zeta x}, \quad\ \text{as } x \to +\infty, \end{aligned} \tag{C.15}$$

hold. Additionally, if q and ζ are real, then we have

$$\bar{\varphi}(x,\zeta) = \varphi(x,-\zeta) = \varphi^*(x,\zeta) \tag{C.16}$$

$$\bar{\psi}(x,\zeta) = \psi(x,-\zeta) = \psi^*(x,\zeta), \tag{C.17}$$

with * denoting complex conjugation. By the linear independence of the irregular solutions (C.12), we can express any solution to the Schrödinger equation as a linear combination of a conjugate pair of just one irregular solution. For this reason, one has the freedom to express the particular solution

$$\varphi(x,\zeta) = a(\zeta)\bar{\psi} + b(\zeta)\psi. \tag{C.18}$$

Moreover, and to serve as further justification of expressing the fundamental solution (C.18), the Wronskian

$$W\left(\bar{\varphi},\varphi\right) = W\left(\bar{\psi},\psi\right) = 2i\zeta, \tag{C.19}$$

implies

$$|a|^2 - |b|^2 = 1, \tag{C.20}$$

by manipulating (C.18) while taking derivatives and conjugates of the definitions when appropriate. For reasons that will become obvious, divide through by $a(\zeta)$. By requiring that our solution satisfy the Fresnel equations (C.11) in the appropriate limit, the left hand side tells us

$$\lim_{x\to-\infty} \frac{\varphi(x,\zeta)}{a(\zeta)} = \frac{1}{a(\zeta)} e^{-i\zeta x} = T(\zeta)e^{-i\zeta x}, \tag{C.21}$$

while the right hand side informs us of how

$$\lim_{x\to\infty} \bar{\psi} + \frac{b(\zeta)}{a(\zeta)}\psi = e^{-i\zeta x} + \frac{b(\zeta)}{a(\zeta)} e^{i\zeta x} = e^{-i\zeta x} + R(\zeta)e^{i\zeta x}. \tag{C.22}$$

By inverting the relation (C.18) we have

$$\psi(x,\zeta) = a(\zeta)\bar{\varphi} - \bar{b}\varphi(x,\zeta). \tag{C.23}$$

We can now connect the conserved quantities, calculated through the Liouville-Green method, to the scattering coefficient $a(\zeta)$ by observing that

$$\left(\psi - \frac{1}{2i\zeta}\varphi\right) e^{-i\zeta x} \sim a(\zeta), \quad \text{as } x \to -\infty, \tag{C.24}$$

implies, remarkably,

$$\ln a(\zeta) \sim -\sum_{n=1}^{\infty} (2i\zeta)^{-n} \int_{-\infty}^{\infty} R_n dx, \quad \text{as } x \to -\infty. \tag{C.25}$$

A key thing to note here is that this expression informs us directly of how

$$\lim_{\zeta \to \infty} a(\zeta) = 1. \tag{C.26}$$

Now, let $\zeta_k = i\eta_k$ denote the k^{th} eigenvalue corresponding to the discrete spectrum of the Schrödinger eigenvalue problem, and, for the moment, assume the function

$$f(\zeta) = \prod_{k=1}^{\infty} \frac{\zeta + i\eta_k}{\zeta - i\eta_k} a(\zeta). \tag{C.27}$$

$f(\zeta)$ is analytic whenever $\Im\{\zeta\} > 0$, and tends to ∞ as $\zeta \to \infty, \Im\{\zeta\} \geq 0$. Therefore, by Cauchy's integral formula

$$\ln f(\zeta) = \frac{1}{2\pi i} \int_{-\infty}^{\infty} \frac{\ln f(\xi)}{\xi - \zeta} d\xi, \tag{C.28}$$

and using the Cauchy-Goursat theorem we have

$$\frac{1}{2\pi i} \int_{-\infty}^{\infty} \frac{\ln f(\xi)}{\xi + \zeta} d\xi = 0, \tag{C.29}$$

by closing the contour in the upper half-plane and using the bound (C.26) on $a(\zeta)$ as $\zeta \to \infty$. Taking $\xi \to -\xi$ in the second equation and subtracting the two, using the relations between a, b, and R, and some algebraic manipulation along with another application of Cauchy-Goursat, we have

$$\begin{aligned} \ln a(\zeta) &= \sum_{k=1}^{\infty} \ln \frac{\zeta - i\eta_k}{\zeta + i\eta_k} + \frac{1}{2\pi i} \int_{-\infty}^{\infty} \frac{\ln |a|^{-2}}{\xi - \zeta} d\xi, \\ &= \sum_{k=1}^{\infty} \ln \frac{\zeta - i\eta_k}{\zeta + i\eta_k} - \frac{\zeta}{\pi i} \int_{0}^{\infty} \frac{\ln\left(1 - |R|^2\right)}{\xi^2 - \zeta^2} d\xi. \end{aligned} \tag{C.30}$$

The trace formulae are found by expanding the left and right hand sides in inverse powers of ζ. For the optimal control strategy of Chapter 6, we only need the first which is

$$\int_{-\infty}^{\infty} q dx = 4 \sum_{k=1}^{N} \eta_k + \frac{2}{\pi} \int_0^{\infty} \ln\left(1 - |R|^2\right) d\xi. \tag{C.31}$$

This formula tells us exactly how the mass of any solution to the KdV equation decomposes into the spectral contributions of the bound and radiative states of the associated ZS eigenvalue problem (C.5).

REFERENCES

[1] The British Museum. Collection database. *The Nimrud Lens/the Layard Lens*. `https://www.britishmuseum.org/collection/object/W_-90959`, Oct 21 2019.

[2] Thorlabs Inc. `https://www.thorlabs.com`, Oct 21 2019.

[3] A. B. Aceves and S. Wabnitz, *Self-induced transparency solitons in nonlinear refractive periodic media*, Physics Letters A, 141 (1989), pp. 37–42.

[4] G. P. Agrawal and S. Radic, *Phase-shifted fiber Bragg gratings and their application for wavelength demultiplexing*, IEEE Photonics Technology Letters, 6 (1994), pp. 995–997.

[5] M. Bardi, M. G. Crandall, L. C. Evans, H. M. Soner, and P. E. Souganidis, *Viscosity Solutions and Applications: Lectures Given at the 2nd Session of the Centro Internazionale Matematico Estivo (CIME) Held in Montecatini Terme, Italy, June, 12-20, 1995*, Springer-Verlag Berlin and Heidelberg GmbH & Co. KG, Berlin, 2006.

[6] R. Bellman, *The theory of dynamic programming*, Bulletin of the American Mathematical Society, 60 (1954), pp. 503–515.

[7] C. S. Bender and S. Orszag, *Advanced mathematical methods for scientists and engineers I: Asymptotic methods and perturbation theory*, Springer-Verlag New York Inc., New York, NY, 2010.

[8] J. Bernoulli, *Problema novum ad cujus solutionem mathematici invitantur*, Acta Eruditorum, (1696), pp. 264–269.

[9] A. Borzì, G. Ciaramella, and M. Sprengel, *Formulation and numerical solution of quantum control problems*, Society for Industrial and Applied Mathematics (SIAM), New York, NY, 2017.

[10] W. Boyce and S. DiPrima, *Elementary Differential Equations*, vol. 10, John Wiley & Sons, Danvers, MA, 2015.

[11] J. P. Boyd, *Chebyshev and Fourier spectral methods*, Dover Publications Inc., New York, NY, 2001.

[12] S. Boyd and L. Vandenberghe, *Convex optimization*, vol. 1, Cambridge University Press, Cambridge, 2004.

[13] A. E. Bryson and Y.-C. Ho, *Applied optimal control: optimization, estimation, and control*, Hemisphere Publishing Corporation, (1975).

[14] T. Caneva, T. Calarco, and S. Montangero, *Chopped random-basis quantum optimization*, Phys. Rev. A, 84 (2011), p. 022326.

[15] W. Choi, *On the fission of algebraic solitons*, Proceedings: Mathematical, Physical and Engineering Sciences, 453 (1997), pp. 1753–1762.

[16] F. H. Clarke, *Method of Dynamic and Nonsmooth Optimization*, Society for Industrial and Applied Mathematics (SIAM), New York, NY, 1989.

[17] M. G. Crandall and P.-L. Lions, *Viscosity solutions of Hamilton-Jacobi equations*, Transactions of the American mathematical society, 277 (1983), pp. 1–42.

[18] E. de Giorgi, *Sulla differenziabilità e l'analiticità delle estremali degli integrali multipli regolari*, Memorie della Accademia delle Scienze di Torino. Classe di Scienze Fisiche, Matematiche e Naturali, 3 (1957), pp. 25–43.

[19] C. M. De Sterke and J. E. Sipe, *Gap solitons*, Progress in Optics, 33 (1994), pp. 203–260.

[20] P. Deift and E. Trubowitz, *Inverse scattering on the line*, Communications on Pure and Applied Mathematics, 32 (1979), pp. 121–251.

[21] M. DeSterke, *Propagation through apodized gratings*, Optics Express, 3 (1998), pp. 405–410.

[22] F. M. Dickey, L. S. Weichman, and R. N. Shagam, *Laser beam shaping techniques*, tech. rep., Sandia National Labs., Albuquerque, NM (US), 2000.

[23] P. Doria, T. Calarco, and S. Montangero, *Optimal control technique for many-body quantum dynamics*, Phys. Rev. Lett., 106 (2011), p. 190501.

[24] Z. Feng, B. D. Froese, R. Liang, D. Cheng, and Y. Wang, *Simplified freeform optics design for complicated laser beam shaping*, Applied Optics, 56 (2017), pp. 9308–9314.

[25] A. T. Fuller, *Bibliography of Pontryagin's maximum principle*, International Journal of Electronics, 15 (1963), pp. 513–517.

[26] C. S. Gardner, J. M. Greene, M. D. Kruskal, and R. M. Miura, *Method for solving the Korteweg-deVries equation*, Physical Review Letters, 19 (1967), p. 1095.

[27] I. Gelfand and S. Fomin, *Calculus of Variations*, Prentice-Hall, Englewood Cliffs, New Jersey, 1963.

[28] R. Glowinski, S. J. Osher, and W. Yin, *Splitting Methods in Communication, Imaging, Science, and Engineering*, Springer International Publishing AG, Cham, 2017.

[29] H. Goldstine, *A History of the Calculus of Variations from the* 17^{th} *through the* 19^{th} *Century*, Springer-Verlag New York Inc., New York, NY, 2012.

[30] J. W. Goodman, *Introduction to Fourier Optics, 4th ed*, W.H. Freeman & Co, Macmillan Learning, New York, NY, 2017.

[31] R. H. Goodman, R. E. Slusher, and M. I. Weinstein, *Stopping light on a defect*, Journal of the Optical Society of America B, 19 (2002), pp. 1635–1652.

[32] D. Hilbert, *Mathematical problems*, Bulletin of the American Mathematical Society, 8 (1902), pp. 437–479.

[33] M. Hintermuller, D. Marahrens, P. A. Markowich, and C. Sparber, *Optimal bilinear control of Gross-Pitaevskii equations*, SIAM (Society for Industrial and Applied Mathematics) Journal on Control and Optimization, 51 (2013), pp. 2509–2543.

[34] U. Hohenester, P. K. Rekdal, A. Borzi, and J. Schmiedmayer, *Optimal quantum control of Bose-Einstein condensates in magnetic microtraps*, Physical Review A, 75 (2007), p. 023602.

[35] S. G. Johnson, *Notes on adjoint methods for 18.335*, Introduction to Numerical Methods, (2012).

[36] W. M. Kunkel and J. R. Leger, *Gradient-index design for mode conversion of diffracting beams*, Optics Express, 24 (2016), pp. 13480–13488.

[37] A. Kurzhanskii, *Pontryagin maximum principle*, Encylcopedia of Mathematics, 2011.

[38] M. Levi, *Classical mechanics with calculus of variations and optimal control: an intuitive introduction*, vol. 69, American Mathematical Society (AMS), Providence, 2014.

[39] E. Lieb and M. Loss, *Analysis*, American Mathematical Society (AMS), Philadelphia, PA, second ed., 2010.

[40] J. Loheac and E. Zuazua, *Maximum principle and bang-bang property of time optimal controls for schr odinger-type systems*, SIAM (Society for Industrial and Applied Mathematics) Journal of Optimal Control, 51 (2013), pp. 4016–4038.

[41] J. Loheac and E. Zuazua, *Norm saturating property of time optimal controls for wave-type equations*, IFAC-PapersOnLine, 49 (2016), pp. 37–42.

[42] O. Madsen and C. Mei, *Dispersive long waves of finite amplitude over an uneven bottom*, in Defense Technical Information Center, 1969.

[43] W. C. K. Mak, B. A. Malomed, and P. L. Chu, *Slowdown and splitting of gap solitons in apodized Bragg gratings*, Journal of Modern Optics, 51 (2004), pp. 2141–2158.

[44] A. Maspero and D. Robert, *On time dependent schrödinger equations: Global well-posedness and growth of sobolev norms*, Journal of Functional Analysis, 273 (2017), pp. 721–781.

[45] E. J. McShane, *The calculus of variations from the beginning through optimal control theory*, SIAM (Society for Industrial and Applied Mathematics) Journal on Control and Optimization, 27 (1989), pp. 916–939.

[46] J. Mennemann, D. Matthes, R. Weishaupl, and T. Langen, *Optimal control of Bose-Einstein condensates in three dimensions*, New Journal of Physics, 17 (2015), p. 113027.

[47] P. D. Miller, *Applied asymptotic analysis*, American Mathematical Society (AMS), Providence, 2006.

[48] J. Mok, C. M. De Sterke, I. Littler, and B. Eggleton, *Dispersionless slow light using gap solitons*, Nature Physics, (2006).

[49] J. V. Moloney and A. Newell, *Nonlinear Optics*, Taylor & Francis Ltd, London, 2018.

[50] R. Moore, W. Kath, and B. G., *Computing statistics of large soliton perturbations*, SIAM (Society for Industrial and Applied Mathematics) Journal of Applied Mathematics, 67 (2007), pp. 1418–1439.

[51] J. Nash, *Continuity of solutions of elliptic and parabolic equations*, American Journal of Mathematics, 80 (1958), pp. 931–954.

[52] A. C. Newell, *Solitons in mathematics and physics*, Society for Industrial and Applied Mathematics (SIAM), New York, NY, 1985.

[53] L. P. Pitaevskii and S. Stringari, *Bose-Einstein Condensation*, Clarendon Press, Oxford, 2003.

[54] G. Pöschl and E. Teller, *Bemerkungen zur quantenmechanik des anharmonischen oszillators*, Zeitschrift für Physik, 83 (1933), pp. 143–151.

[55] K. Price, R. Storn, and J. Lampinen, *Differential Evolution: A practical approach to global optimization*, Springer-Verlag Berlin and Heidelberg GmbH & Co. KG, Berlin, 2018.

[56] A. Rosenthal and M. Horowitz, *Analysis and design of nonlinear fiber Bragg gratings and their application for optical compression of reflected pulses*, Optics Letters, 31 (2006), pp. 1334–1336.

[57] A. Rosenthal and M. Horowtiz, *Efficient method for launching in-gap solitons in fiber Bragg gratings using a two-segment apodization profile*, Optics Letters, 33 (2008), pp. 678–680.

[58] I. M. Ross, *A historical introduction to the convector mapping principle*, in Proceedings of Astrodynamics Specialists Conference, 2005.

[59] I. M. Ross and F. Fahroo, *Legendre pseudospectral approximations of optimal control problems*, in New trends in nonlinear dynamics and control and their applications, Springer, 2003, pp. 327–342.

[60] L. Ruthotto, S. J. Osher, W. Li, L. Nurbekyan, and S. W. Fung, *A machine learning framework for solving high-dimensional mean field game and mean field control problems*, Proceedings of the National Academy of Sciences, 117 (2020), pp. 9183–9193.

[61] J. Serrin, *The solvability of boundary value problems, mathematical developments arising from Hilbert problems*, Proceedings of Symposia in Pure Mathematics, 28 (1983), p. 507–524.

[62] G. Smith, *Newton's Philosophiae Naturalis Principia Mathematica*, in The Stanford Encyclopedia of Philosophy, E. N. Zalta, ed., Metaphysics Research Lab, Stanford University, Winter 2008 ed., 2008.

[63] J. J. Sørensen, M. Aranburu, T. Heinzel, and J. Sherson, *Approaching the quantum speed limit with global-local optimization*, arXiv preprint arXiv:1802.07521, (2018).

[64] R. Storn and K. Price, *Differential evolution–a simple and efficient heuristic for global optimization over continuous spaces*, Journal of Global Optimization, 11 (1997), pp. 341–359.

[65] G. Strang, *Introduction to linear algebra*, vol. 3, Wellesley-Cambridge Press, Wellesley, MA, 1993.

[66] S. H. Strogatz, *Nonlinear dynamics and chaos with student solutions manual: With applications to physics, biology, chemistry, and engineering*, Taylor & Francis Ltd, London, 2018.

[67] F. D. Tappert and N. J. Zabusky, *Gradient-induced fission of solitons*, Physical Review Letters, 27 (1971), p. 1774.

[68] V. Tikhomirov, *Weierstrass conditions (for a variational extremum)*, Encyclopedia of Mathematics (EoM), 2011.

[69] A. N. Tikhonov, A. V. Goncharsky, V. V. Stepanov, and A. G. Yagola, *Numerical Methods for the Solution of Ill-Posed Problems*, Springer, Dordrecht, 1995.

[70] L. N. Trefethen, *Spectral methods in MATLAB*, Society for Industrial and Applied Mathematics (SIAM), New York, NY, 2000.

[71] B. van Brunt, *The Calculus of Variations*, Springer-Verlag New York Inc., New York, NY, 2004.

[72] S. van Frank, M. Bonneau, J. Schmeidmayer, S. Hild, C. Gross, M. Cheneau, I. Bloch, T. Pichler, A. Negretti, T. Calarco, and S. Montangero, *Optimal control of complex atomic quantum systems*, Scientific reports, 6 (2016), pp. 1–12.

[73] J. Viana-Gomes and N. M. R. Peres, *Solution of the quantum harmonic oscillator plus a delta-function potential at the origin: the oddness of its even-parity solutions*, European Journal of Physics, 32 (2011), p. 1377.

[74] Virgil, *The Aenid*, Vintage Books, New York, NY, 1983.

[75] G. von Winckel and A. Borzi, *Computational techniques for a quantum control problem with H1-cost*, Inverse Problems, (2008).

[76] D. G. Wells, *The Penguin dictionary of curious and interesting geometry*, Penguin Books Ltd, London, 1991.

[77] G. B. Whitham, *Linear and Non-linear Waves*, John Wiley & Sons Inc, New York, NY, 1974.

[78] T. Witelski and M. Bowen, *Methods of Mathematical Modeling*, Spring Undergraduate Mathematics Series, Cham, 2016.

[79] D. R. Yafaev, *Mathematical scattering theory: general theory*, American Mathematical Society (AMS), Providence, RI, 1992.

[80] J. Yang, *Nonlinear Waves in Integrable and Nonintegrable Systems*, Society for Industrial and Applied Mathematics (SIAM), New York, NY, 2010.